QUANTITATIVE MAPPING IN MAGNETIC RESONANCE IMAGING

by
Guan Wang

A dissertation submitted to Johns Hopkins University in conformity with the requirements for the degree of Doctor of Philosophy

Baltimore, Maryland

December, 2015

Abstract

Magnetic Resonance Imaging (MRI) produces superior soft tissue contrast that is mostly determined by the tissue relaxation times (T_1 and T_2) and spin density (PD). This dissertation introduces novel methods to quantify T_1, T_2 and PD, and explored their value for disease classification, and tracking delivery of cell therapies.

First, a novel T_2 measurement (Dual-τ) method that employs adiabatic pulses is proposed, that exploits the property that the spins undergo T_2 decay during excitation by long adiabatic pulses. The new method is relatively immune to MR static and excitation field inhomogeneity, and has a higher efficiency than the conventional methods. The adiabatic excitation pulse can also serve as a preparation pulse that introduces T_2 contrast into the MRI, and can be combined with T_1 quantification methods to produce T_1 and T_2 simultaneously. The method is shown to be most accurate at short T_2s. The T_2 measurements were validated in phantoms and *in vivo* in human studies.

Second, three methods of mapping T_1, T_2, and PD simultaneously with the least possible number of acquisitions are presented, also utilizing adiabatic pulses. The first, Dual-τ-Dual-FA method, encodes T_1 by varying excitation flip-angle (FA). The second, Dual-τ-Dual-TR method, encodes T_1 using the variations in the sequence repetition time (TR). The third method incorporates the FA self-correction to eliminate T_1 errors caused by field inhomogeneities, and is called the Four-FA method. All three methods were validated in phantom studies, and the Dual-τ-Dual-FA and Four-FA methods were validated in human brain studies as well. The Four-FA method is demonstrated to have the best overall accuracy compared to the existing methods, such as DESPOT1/2, IR TrueFISP, etc.

Combining the multi-parametric mapping methods with intravascular (IV) MRI potentially offers a means of reducing the scan time and increasing the local SNR. For the first time, multi-parametric high-resolution (<200μm) T_1, T_2, PD and fat images of human vessels are obtained. These maps were used to train a machine-learning based classifier to automatically distinguish early- and advanced-stage vessel disease from healthy and smooth muscle. This application enables differentiation of vessel wall disease types with high sensitivity and specificity compared with histology as the standard.

The contrast of cells delivered as therapeutic agents in MRI can be enhanced using capsules impregnated with MRI-sensitive contrast agents. At the end of the dissertation, we explore quantitative cell tracking using ^{19}F-labeled capsules that provide dual modality contrast for both computed tomography (CT) and MRI. The method was validated in rabbit diseased models using clinical imaging systems. Compared with CT, ^{19}F MRI was able to accurately track cells non-invasively *in vivo,* without the use of ionizing radiation. Two weeks after the cell administration, no significant changes in the volume or concentration of the capsules were observed, and the cells preserved high viability according to histology.

Advisor and first reader: Paul A. Bottomley

Russell H. Morgan Professor, Department of Radiology and Radiological Science,

School of Medicine, Johns Hopkins University

Second reader: Alexander Kaplan

Professor of Electrical and Computer Engineering,

Whiting School of Engineering, Johns Hopkins University

Acknowledgement

First of all, my most sincere thanks go to my advisor, Dr. Paul A. Bottomley. He has been extremely patient with me, and carefully guided me into the field of research science step-by-step, like a father. His intelligence, diligence, acuity, 40 years' constant passion for medical imaging, and tremendous knowledge about MRI always motivate me and made me very proud to be his student, over the past six years and, into the future.

Then, my thanks go to Dr. William A. Edelstein, who co-advised me during the second and the third year of my PhD. He was a kind, wise man, who had extensive knowledge and opinions on varied topics. He always eased my tension with his jokes. I will always remember that he worked until his last day in the world.

I would like to thank Dr. Dara L. Kraitchman, who also co-advised me. She is the most hands-on advisor that I know. She provided me with the opportunity to work with animals and with multiple imaging modalities. I would also express my appreciation to Dr. Shashank S. Hegde, who has been a great companion for me. During the two years of his postdoc at Hopkins, he helped me with every intravascular imaging experiment. He is still open to my questions, even though he now works for a company in India. I want to thank Dr. Abdel-Monem M. El-Sharkawy. He was the first person who taught me about how to work in a lab. I learned a lot from his strict and professional attitude toward research.

I am thankful to the following colleagues who offered their enormous and prompt help during our collaboration: Dr. Yingli Fu, for her thoughtful advice and careful plan for my stem cell project; Dr. Michael Schär, who is always ready to solve any problems I have on MR sequences; Parag Karmarkar, for all his work on the interventional coil for

me; Dr. Ye Qiao, for introducing me to clinical studies and offering advice about career plans. I thank Dr. Jinyuan Zhou, Dr. Alexander Kaplan, Dr. Jin U. Kang, Dr. Trac D. Tran and Dr. Daniel Herzka for being the committee members of my oral exam, proposal and defense. I thank all my co-authors, without whom I would not have been able to produce the work I did: Dr. Steven Shea and Dr. Li Pan from Siemens; Judy Cook who skillfully performed all the animal surgeries for me; and Dr. Laura Rose from the Cell Engineering lab.

I feel grateful to have had the opportunity to work with my lab-mates: Dr. Yi Zhang for his insightful discussions as we learned about MRI together, and for his friendship; and Dr. M. Arcan Erturk, Xiaoyang Liu, Dr. Refaat Gabr for their generous assistance during my PhD. I also want to thank some special people in the MR division: Dr. Robert Weiss for his kind support; Dr. Sahar Soleimanifard for serving as a role model; Dr. Ying Cheng for her sweet friendship; and Ms. Peggy Herman for her administrative help. I thank all the enlightened faculties and motivated students in this division for all the inspiring time we have shared.

My life at Hopkins would not be so memorable if I hadn’t met my friends. You are brothers and sisters to me, especially Yixin Gao, whom I literally call sister. I feel privileged to know so many smart minds and brave souls. A significant part of my knowledge and courage comes from listening to your stories.

Last but not least. I want to express my deepest gratitude to my family: my parents, Dr. Huiran Wang and Ruifang Ma, who have been very open-minded and supportive of my study for 28 years; and, to Detian Deng, for his vision, knowledge, constant support and care, all of which lets me know that marrying him is the best decision of my life.

Guan Wang

Baltimore, MD

Nov 2015

Table of Contents

Chapter 3. Minimum Acquisition Methods for Simultaneously Imaging T_1, T_2, and Proton Density with B_1 Correction and No Spin-echoes 44

List of Figures

List of Table

Abbreviation

2D: two dimensions
3D: three dimensions
AFI: actual flip angle imaging
AHA: American Heart Association
Allo: allogeneic
ANOVA: two-way analysis of variance
BB: black blood
BIR-4: B_1-insensitive rotation pulses
BPP: Bloembergen-Purcell-Pound
BW: bandwidth
CA: contrast agent
CNR: contrast-to-noise ratio
CPMG: Carr-Purcell-Meiboom-Gill
CSF: cerebral spinal fluid
CT: X-ray computed tomography
DSA: dynamic subtraction angiogram
^{19}F: fluorine
f_{max}: maximum frequency sweep
FA: flip angle
FETS: fast exchange two-state model
FT: Fourier transform
FID: free induction decay
FOV: field-of-view
GM: gray matter
GRE: gradient echo
^{1}H: proton
H&E: hematoxylin and eosin
HU: Hounsfield units
HuNa: anti-human nuclear antigen
IR: inversion-recovery
IRB: Institutional Review Board
IV: intravascular
M: magnetization moment
M_0: equilibrium magnetization
M_z: longitudinal component of magnetization
M_{xy}: transverse component of magnetization
MIP: maximum intensity projection
MR: magnetic resonance
MRF: MR fingerprinting

MRI: magnetic resonance imaging
MSC: mesenchymal stem cell
MT: magnetization transfer
NMR: nuclear magnetic resonance
OCT: optical coherence tomography
PAD: peripheral artery disease
PD: nuclear spin density
PFOB: perfluoro-octyl-bromide
PS: partial saturation
Pu: percent units
PVE: partial volume effect
RF: radio frequency
ROC: Receiver Operating Characteristic
ROI: region of interest
SC: stem cell
SD: standard deviation
SE: Spin-echo
SFA: superficial femoral artery
SNR: signal-to-noise ratio
SPIO: superparamagnetic iron oxide
SSFP: steady-state free-precession
τ: pulse length
T: Tesla
T_1: spin-lattice relaxation time
T_2: spin-spin relaxation time
T_2-prep: T_2-preparation
TE: echo time
TR: repetition time
TrueFISP: true fast imaging with steady state precession
TSE: turbo spin echo
US: ultrasound
vs.: versus
VVG: Verhoeff-Van Gieson
WM: white matter
Xeno: xenogeneic
XMRCap: perfluorooctylbromide-containing microcapsule

Chapter 1. Introduction

1.1 Overview of the thesis

Magnetic Resonance Imaging (MRI) is a technique that was developed in the 1970s[1], and has been widely applied in medical diagnosis and treatment since its first clinical use in the 1980s. It was first referred to as Zeugmatography, then "nuclear" magnetic resonance (NMR) imaging, even though there is no ionizing radiation involved. During an MRI scan, a body in the strong magnetic field is excited by radio frequency (RF) waves, assembled into RF pulse sequences, and then, as the nuclear magnetization gradually recovers to equilibrium, the body re-emits signal. MRI has no known health risks, although the magnets can attract ferromagnetic projectiles. The RF wave from an MR scanner is in the electromagnetic spectrum, as are the RF waves emitted from our cell phones, radios, TVs, and microwave ovens, which operate at different frequencies. To overcome physicians' fear associated with the word "nuclear," NMR was renamed MRI. In fact, my co-advisor William A. Edelstein and advisor Paul A. Bottomley wrote a letter to the editor of Radiology in 1984 to explain that there was no reason to fear, because all matter is made of nuclei, "which are not about to explode"[2]. The editor agreed with them, but responded that "the educational effort" was unlikely to be successful in the near-term.

In addition to its safety, another great advantage of MRI is its versatility. This resulted in extensive research that has fostered many innovations over the years. Here, "versatility" has two interpretations. In a narrow sense, it means that MRI can be performed in any arbitrary plane in either two dimensions (2D) or three dimensions (3D).

In a broader sense, MRI is flexible in terms of image contrast. Because the signal source lies in the body, the signal is largely dependent on many local tissue characteristics: the nuclear density; the motion of the nuclear signal sources; temperature; the chemical environment of the nuclei; tissue heterogeneity; etc. Indeed, MRI produces soft tissue contrast superior to that of any other imaging modalities. Among all these characteristics, the three tissue parameters: the nuclear spin density (PD), the spin-lattice relaxation time (T_1), and the spin-spin relaxation time (T_2) of the water protons (^1H), are essential for controlling the contrast in routine MRI. How to produce these three parameters and generate contrast-optimized magnetic resonance (MR) images for tissue differentiation and disease diagnosis is a stimulating topic in MRI research, and forms the basis for this thesis.

However, although MRI is versatile and safe, it cannot always replace other imaging modalities, even for soft tissue imaging. As well as the bulk size, high maintenance cost, and noisy acquisitions of MR scanners, a major drawback is the relatively slow speed. The signal-to-noise ratio (SNR) is proportional to the square root of the acquisition time, and thus, reducing the scan time causes a loss of signal, and may render images more susceptible to artifacts as well. One effective metric by which to evaluate MRI sequences is efficiency-per-unit-accuracy of the signal or parameter being imaged. The sequence with the highest efficiency-per-unit-accuracy requires the shortest acquisition time to reach the same signal precision and accuracy. For the new MRI sequences presented in this thesis, the efficiency-per-unit-accuracy has been compared with existing sequences and the results are reported.

After the three main parameters are produced by high-efficiency-per-unit-accuracy sequences, the question becomes: “What combination of the three parameters will yield an image whose contrast can best help diagnosing a given medical condition?” In other words, how can we best increase the contrast between pathological and healthy tissue using the information from the three parameters? This is an optimization problem that is similar to finding the global minimum solution in a 3D (or higher) space. Obviously, the optimum solution varies for different types of disease, thus the weights for combining the three parameters would also change. Radiologists choose to perform T_1-weighted, T_2-weighted, or PD-weighted sequences for disease diagnoses based on empirical experience, but there is no quantitative guideline for producing optimized contrast images.

When cells are to be imaged, the contrast enhancement based on the three main MRI parameters and the spatial resolution are usually not sufficient to distinguish individual cells. In this case, a cell-labeling technique was invented to further increase the contrast with special reporter probes that allow the cells to be visualized [3]. The cell labeling probe can be negative, such as with iron oxide-based contrast agents that induce dark susceptibility artifacts at the cell’s location[4]. However, the dark signal from the cells may be offset because the surrounding tissue ^{1}H signal confounding its differentiation. Labeling the cells with an NMR nucleus that does not normally exist in the tissue can provide strong signal hot spots if MRI is performed of the new nucleus, without proton signal contamination from tissue. Due to the near-absence of fluorine (^{19}F) in nearly all mammalian tissues, ^{19}F MRI could advantageously generate positive signals with NMR sensitivity comparable to that of ^{1}H MRI [5, 6]. MRI-based cell-tracking is a rapidly developing field, and there is hope that it will not only allow localized detection, but also enable quantification of the cell count *in vivo*.

Thus, this thesis explores MRI contrast in many aspects, from its fundamental mechanisms, the development of MRI methods to quantify T_1, T_2 and PD, to its applications in automatic disease classification, and quantitative cell-tracking employing ^{19}F MRI.

The remainder of this chapter will describe the fundamental concepts of NMR and MRI contrast. The basis of T_1 and T_2 and the conventional methods of measuring them are introduced. In addition, methods to improve contrast, including contrast agents are explored.

In Chapter 2, the development of a new T_2 measurement and imaging sequence that employs long adiabatic excitation pulses without the conventional spin echoes is reported. The new method has the advantages of immunity to static and excitation field inhomogeneity, and efficiency. The adiabatic excitation pulse can also serve as a preparation pulse that introduces T_2 contrast into the images, which can then be combined with T_1 quantification methods to produce simultaneously T_1 and T_2.

Chapter 3 builds on this work to develop several methods of mapping T_1, T_2, and PD with a minimum number of acquisitions. Based on the T_2 provided by the adiabatic pulses, the T_1 contrast is introduced using either variations in flip-angle (FA) or the sequence repetition time (TR), in the new Dual-τ Dual-FA method and Dual-τ Dual-TR methods. However, T_1 measurements are very sensitive to inhomogeneity in the excitation field (B_1). Thus, we incorporated one more acquisition to create a set of 4 acquisitions to provide T_1, T_2, and PD maps that incorporate a B_1-field inhomogeneity self-correction. This set of acquisitions is called the 'Four-FA' sequence.

In Chapter 4 we use the measured parameters to distinguish vessel wall disease. Autopsied vessel specimens were imaged with interventional MRI coils using T_1, T_2, and PD quantification sequences. A 3D space is constructed in which each axis corresponds to one of these parameters. A machine-learning algorithm was trained to partition the space into sub-spaces, compromised different stages of disease. This application enabled differentiation of tissue types for disease classification with high sensitivity and specificity.

Finally, in Chapter 5, we explore quantitative cell tracking using ^{19}F-labeling. The ^{19}F labeling is introduced by impregnating the cell capsules with perfluoro-octyl-bromide (PFOB). Compared with X-ray computed tomography (CT), MRI was able to accurately track cells non-invasively *in vivo,* without the use of ionizing radiation.

1.2 MR Basics

1.2.1 History of MR

In 1937, Isidor Isaac Rabi, an American physicist from Columbia University, recognized that the atomic nuclei absorb or emit radio waves when exposed to a magnetic field, and was first to use the magnetic resonance method to observe atomic spectra[7, 8]. He was awarded the Nobel Prize for Physics in 1944 for this work[9]. In 1946, Felix Bloch and Edward Mills Purcell independently, but contemporaneously, demonstrated the "nuclear magnetic resonance" phenomenon. They developed similar methods to measure the magnetic moments of nuclei, and shared the Nobel Prize in 1952 [10, 11]. Later, Purcell, along with Nicolaas Bloembergen and Robert Pound published a comprehensive theory of nuclear magnetic relaxation[12]. The landmark article is known as the "BPP" paper, and is one of the foundations in NMR physics. In 1950, Erwin Hahn introduced the pulse NMR experiment and discovered the "spin-echo" phenomenon which he used to measure NMR T_2 values[13]. In the 1960s, Richard R. Ernst and Weston A. Anderson showed that Fourier transforming (FT) the time-domain NMR signal from the pulsed NMR experiment greatly improved the SNR of the NMR spectrum for chemical analysis, allowing high-resolution analysis of many more types of nuclei. Ernst won the Nobel Prize in Chemistry in 1991 for this contribution[14]. Allan M. Cormack and Godfrey N. Hounsfield developed the CT scanner in 1970s, with the reconstruction-from-projection technique. This inspired Paul C. Lauterbur to reconstruct the first MR image by coupling the CT projection reconstruction and the gradient concept to generate angular projections through a sample[1]. Sir Peter Mansfield pushed the transition from NMR to MRI forward with the development of echo-planar imaging, which allowed the creation of a 2D MRI within one excitation[15]. Lauterbur and Mansfield were both awarded the Nobel Prize in Physiology or Medicine in 2003 for their work in MRI. In 1986, Kurt Wuthrich developed the NMR spectroscopy method to determine the 3D structure of biological macromolecules in solution[16], for which he shared the 1999 Nobel Prize in Chemistry[17].

During the 1970s, John Mallard's team built the first full-body MRI scanner at the University of Aberdeen. My former co-advisor William Edelstein was part of this group which performed the first clinical study on a patient in August, 1980[18]. Dr. Edelstein was also the primary inventor of "spin-warp," the 2D FT-based technique that has dominated the spatial encoding since then[19]. In 1980, my advisor, Paul Bottomley, and his team ordered the highest field magnet available at that time—a1.5 Tesla (T)—and built the first high-field whole-body MRI/MRS scanner, increasing the field strength almost four times from 0.4 T. According to the market report of 2013[20], 1.5T MRI scanners still represent more than 60% market share. Recently, higher-field-strength (3T-7T) scanners have gained a foothold in an increasing number of institutions, and human MRI studies have now been performed at fields of 9.4T[21], while animal MRI studies have been performed at 21.1T[22].

1.2.2 MR Physics

The NMR phenomenon occurs in atoms with an odd number of protons or neutrons, such as ^{1}H, ^{31}P, ^{23}Na, ^{19}F, etc. These atoms possess spin angular momentum, and are called "spins." The spins in the magnetic field produce an effective "magnetic dipole moment." The average magnetic dipole moment density per volume is called the nuclear magnetization, M. Unless stated otherwise, the ^{1}H nucleus is the subject of the rest of the thesis.

In the quantum mechanical view, in the presence of a static magnetic field B_0 directed, by convention, along the z-axis of a Cartesian coordinate frame, the number of nuclei that are parallel to the field exceeds those that are anti-parallel (Fig 1.1a). We assume that the ratio between the two populations of nuclei follows the Boltzmann distribution, $\frac{n_-}{n_+} = e^{\frac{-\Delta E}{kT}}$. This produces an equilibrium nuclear magnetization, $M_0 = \gamma\hbar / 2(n_+ - n_-)$. Here $n_- + n_+ = \rho_0$, where ρ_0 is the total number of spins per unit volume. $\Delta E = -h\gamma B_0 / 2\pi$ is the energy difference between the two states. $\hbar = h/2\pi$ is

Planck's constant, T is absolute temperature, k is the Boltzmann's constant, and γ is a constant named the gyromagnetic ratio. For ^{1}H, $\gamma/2\pi = 42.58$ MHz/T.

In all the applications and temperatures considered here, we have $\Delta E \ll kT$, [typically, $\Delta E/kT = O(10^{-5})$], so that $n_- \square n_+ \square \rho_0/2$, $n_- - n_+ \square \ \rho_0/2$. M_0 is then found as

$$M_0 = \frac{\rho_0 \gamma^2 \hbar^2}{4kT} B_0 \qquad [1.1]$$

At a human body temperature of 37 ºC, the excess is about 5 out of every 10^6 spins at 1.5T. [23]

If M does not align with the field, it will precess about the field at the "Larmor frequency", given by

$$\begin{aligned} \omega &= \gamma B \quad \text{rad/s} \\ f &= \frac{\gamma}{2\pi} B \quad \text{Hz} \end{aligned} \qquad [1.2]$$

Clearly, the Larmor frequency depends linearly on the field strength.

When a RF magnetic field B_1 rotating at the Larmor frequency ω is applied in the transverse direction (x-y plane), M will be rotated away from the longitudinal direction (z-axis) by a flip angle (FA, Fig1.1b). This process is called an excitation. Following the excitation, M will continue to precess about the z-axis, and the component in the x-y plane, M_{xy} will produce a RF signal, often called a free induction decay (FID), which can be detected via Faraday's law of induction. The devices used to transmit B_1 or receive FID are called RF coils. At the same time, the longitudinal component of M (M_z) will regrow while M_{xy} will decay, until M returns to the equilibrium state. Relaxation time constants T_1 and T_2 measure the return of M_z and M_{xy} to the equilibrium, respectively (Fig 1.1c-d). The mechanisms of T_1 and T_2 are elaborated in Section 1.3. For convenience, a frame of reference x'-y' rotating about z at ω is conventionally introduced to simplify the motion of M (Fig 1.1e).

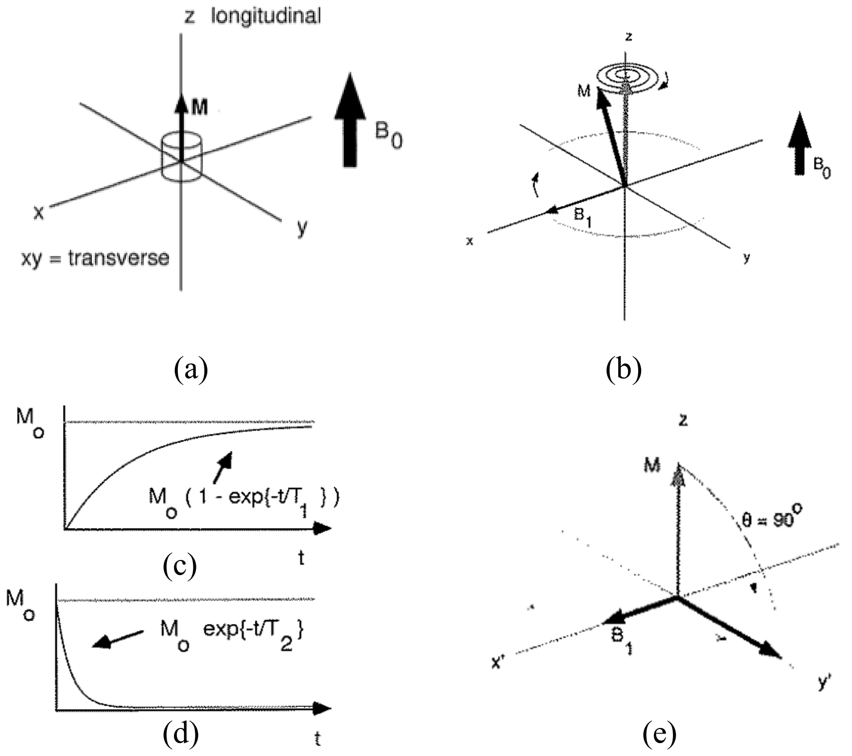

(a) (b)

(c) (d) (e)

Fig 1.1 (a) Applied B_0 field and magnetization M. The B_0 direction is defined as the z-axis, and the perpendicular plane is called the transverse (or x-y) plane. (b) RF B_1 excitation at the Larmor frequency. M is tipped away from z while precessing about z at the same frequency. (c) M_z and (d) M_{xy} during relaxation back to equilibrium. (e) The rotation frame-of-view following a 90° excitation, with the x-y plane rotating at the Larmor frequency. The rotation frame is denoted x'-y'. Fig1.1 is from Nishimura [24].

The behavior of **M** is governed by the Bloch equation,

$$\frac{d\mathbf{M}}{dt} = \mathbf{M} \square \gamma \mathbf{B} - \frac{M_x i + M_y j}{T_2} - \frac{(M_z - M_0)k}{T_1} \qquad [1.3]$$

with i, j, k the unit vectors in x, y, z directions. The cross product on the right describes what happens during the B_1 pulse, the 2nd and the 3rd term describes the behavior between pulses.

To localize the signal source, a magnetic gradient field pointing in the z direction is added to the B_0. The added field strength can be varied linearly in any of the x, y, z directions, with the gradients denoted G_x, G_y, G_z corresponding to $\partial B_0/\partial x$, $\partial B_0/\partial y$, $\partial B_0/\partial z$ respectively. After the application of the gradient field, or “gradients” for short, the Larmor frequency of the spin at (x, y, z) becomes $\omega=\gamma(B_0+G_x x+G_y y+G_z z)=\gamma(B_0+\mathrm{G}\cdot\mathrm{r})$. For simplicity, from hereafter in this section, we will ignore the T_2 decay and assume the signals are from the transverse 2D plane at z=0. Then, based on the Bloch equation, with a time varying gradient G(t), the received signal for the transverse plane is

$$s(t)=\int_x\int_y m(x,y)e^{-i2\pi[k_x(t)x+k_y(t)y]}\,dx\,dy \tag{1.4}$$

where $k_x(t)=\frac{\gamma}{2\pi}\int_0^t G_x(\tau)d\tau$, $k_y(t)=\frac{\gamma}{2\pi}\int_0^t G_y(\tau)d\tau$, m(x,y) is the integral of M(x,y,z) over z. We immediately associate the signal equation with a FT. Indeed, the signal equation can be alternatively written as the FT of m(x,y),

$$s(t)=\mathcal{M}(k_x(t),k_y(t))=\mathcal{M}(\frac{\gamma}{2\pi}\int_0^t G_x(\tau)d\tau,\frac{\gamma}{2\pi}\int_0^t G_y(\tau)d\tau) \tag{1.5}$$

When the gradient is on ($G_x\neq0$ or $G_y\neq0$), the signal received at the time t equals the 2D FT of m(x,y) at the spatial frequency ($k_x(t)$, $k_y(t)$). The Fourier space is called k-space in MRI in analogy to X-ray crystallography. By controlling G_x and G_y in [1.5], the signal can be acquired at different k-space positions. Therefore the gradients determine the k-space trajectory. Spatially encoding the spins in the x direction using G_x is called frequency encoding, while encoding in the y direction using G_y is called phase encoding.

To excite only a plane in the object instead of the whole object, a slice selection gradient G_z is added. This will result in the excitation of only the spins on resonance at

$G_z=0$, which is defined by the user. A phase shift caused by G_z during the application of the RF pulse can be removed by reversing the G_z for half of the pulse duration after the pulse. A pulse sequence timing diagram describes the timing of applying a RF excitation pulse and the gradients (Fig 1.2a-b).

To reconstruct the image m(x,y), we need a sufficient poriton of k-space to be covered. Assuming signals are acquired by sampling with the periods Δk_x, Δk_y, and the highest sampled spatial frequencies are $k_{x\max}$, $k_{y\max}$ (Fig 1.2 c), we are able to generate an image with a field-of-view (FOV) and a special resolution δ as follows,

$$FOV_x = \frac{1}{\Delta k_x}, FOV_y = \frac{1}{\Delta k_y} \qquad [1.6]$$

$$\delta_x \square \frac{1}{2k_{x\max}}, \delta_y \square \frac{1}{2k_{y\max}} \qquad [1.7]$$

as in Fig 1.2 (d).

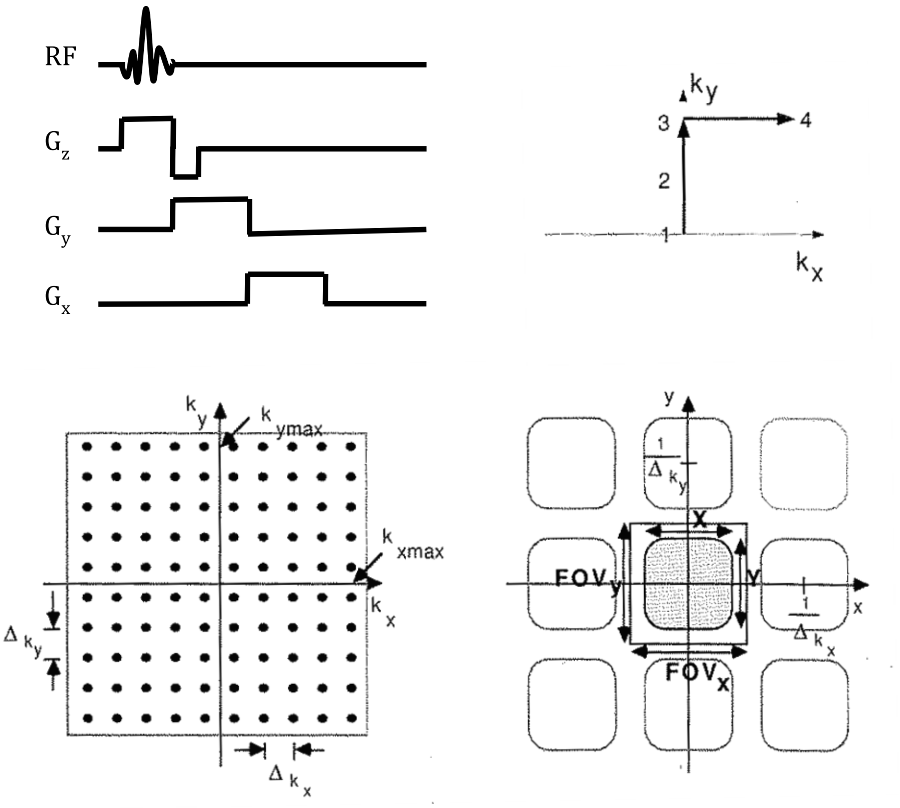

Fig 1.2(a) A pulse sequence timing diagram showing the application of a RF pulse and the G_x, G_y gradients. (b) The corresponding k-space trajectory. After RF excitation, G_y is turned on first. K_y is the time integral of G_y, thus $k_y(t)$ increases until G_y turns back to zero when it stops increasing. Similarly, when G_x is turned on, the sampled signal corresponds to a horizontal line in k-space. (c) Sampling in k-space. (d) Corresponding spatial domain. The sampling period controls the FOV, while the highest sampled frequency determines the image resolution. Fig1.2 is from Nishimura [24].

An MR image is generated by Fourier transforming the sampled k-space data into the spatial domain. These are the basic imaging principles of MRI.

1.3 Relaxation times

Here, the T_1 and T_2 relaxation times are discussed in detail. Their mechanisms, dependence on environmental factors and tissue characteristics, value in the disease diagnosis, as well as the conventional methods of measuring them, are explained.

1.3.1 Defining relaxation

T_1 characterizes the relaxation of excited spins to the equilibrium state in the longitudinal direction. The relaxation involves energy-state transitions. From the quantum mechanics view, for a spin-1/2 NMR nucleus, the spins and the lattice are in either of the two states: the high-energy state m=-1/2 (i.e., anti-parallel to B_0) or the low-energy state m=+1/2(i.e., parallel to B_0). The energy transition between the spins and the lattice can be described as

$$\frac{d(\Delta N)}{dt} = \frac{(\Delta N)_0 - \Delta N}{T_1} \qquad [1.8]$$

Where $\Delta N \equiv N_+ - N_-$ is the spin excess pointing in the +z direction, with N_+ and N_- referring to the number of spins in the lower and higher energy states respectively. $(\Delta N)_0$ is ΔN at equilibrium. The energy exchange rate between the spins and the lattice defines T_1, spin-lattice relaxation constant. Integrating Eq [1.8] over a volume actually yields the longitudinal part of the Bloch equation [1.3].

At equilibrium, by definition, there is an equal probability for the energy jump upward and downward, the number of spins in each state is dynamically balanced with a slight excess in the low energy state, as given by the Boltzman distribution. The RF pulses transmit energy to the system, resulting in more anti-parallel spins corresponding to the high-energy state. To return to equilibrium requires spin transition from m=-1/2 to m=+1/2 at the decay rate, T_1, such that $\Delta N \to (\Delta N)_0$. Eventually, at equilibrium, resulting in $\frac{d(\Delta N)}{dt} = 0$ [23]. The general solution to the differential equation [1.8] of longitudinal magnetization at time t in the absence (or between) B_1 excitation pulses is:

$$M_z(t) = M_0 + (M_z(0) - M_0)e^{-t/T_1} \qquad [1.9]$$

T_2 is the time constant that describes the decay of M_{xy} due to the phase incoherence in the transverse plane, in addition to T_1 relaxation. The interactions between the spins result in a local field disturbance ΔB(t), causing the dephasing of the spins and a reduced MR signal from a volume. The general solution to the transverse part of the Bloch equation at time t (between excitation pulses) is:

$$M_{xy}(t) = M_{xy}(0)e^{-t/T_2} \tag{1.10}$$

1.3.2 What decides T_1 and T_2?

Many models have been developed to explore factors that affect relaxation. Presented here are the dominant BPP theory [12], and the fast exchange two-state (FETS) model describing its application to tissue[25].

The energy state transitions of the spins are always stimulated by the surrounding magnetic field perturbation resulted from molecular tumbling motion in which the spins behave as magnetic dipoles. The energy exchange is thermal. The probability of transition is related to the amount of perturbations at the resonance frequency. The average time duration of a spin interacting with the magnetic perturbations is called the correlation time (τ_c). In the BPP theory of dipole relaxation, T_1 and T_2 are decided by τ_c (Fig 1.3a):

$$\frac{1}{T_1} = K[\frac{\tau_c}{1+\omega_0^2\tau_c^2} + \frac{4\tau_c}{1+4\omega_0^2\tau_c^2}] \tag{1.11}$$

$$\frac{1}{T_2} = \frac{K}{2}[3\tau_c + \frac{5\tau_c}{1+\omega_0^2\tau_c^2} + \frac{2\tau_c}{1+4\omega_0^2\tau_c^2}] \tag{1.12}$$

Where ω_0 is the Larmor frequency and K is a constant ($\sim 10^{10}s^{-2}$). For bulk water, molecules move very fast; thus, τ_c is very short ($\sim 10^{-12}$s), $\omega_0\tau_c \ll 1$, and $T_1 \approx T_2$. For solid, molecules are tightly bounded and τ_c becomes very long ($\sim 10^{-5}$s), thus $\omega_0\tau_c \gg 1$.

Consequently solids tend to have very long T_1s and ultra short T_2s. For viscous liquid, τ_c is about 10^{-9}s, which is near the minimum of the T_1 curve in Fig 1.3a. T_1 and T_2 values of the viscous liquids are typically closer to each other than those of solids, but further apart than those of low-viscousity liquids. The T_1 of viscous liquid is clearly frequency dependent in this case (Fig 1.3b).

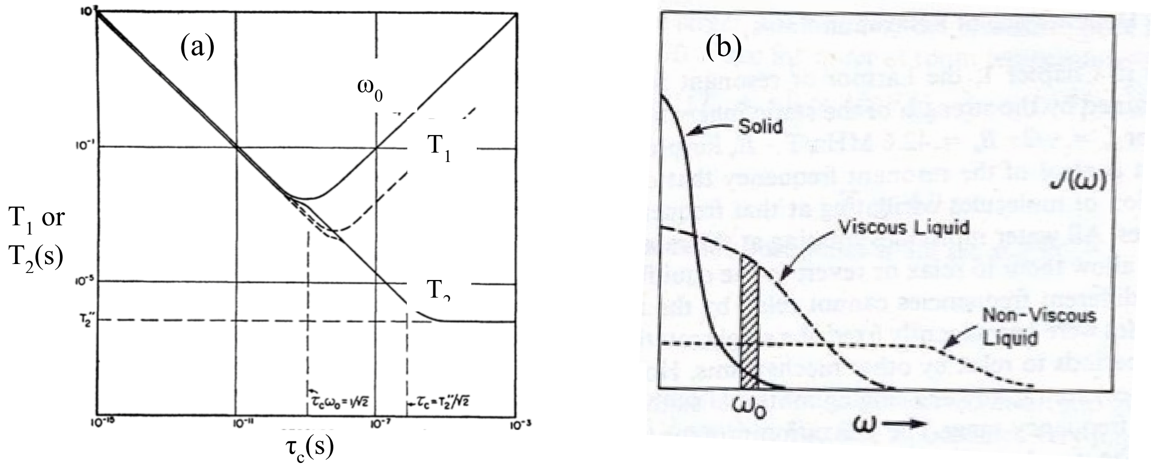

Fig 1.3. (a) T_1 and T_2 relaxation times as a function of correlation time τ_c. Viscous liquid has the lowest T_1. (b) Substance spectrum distribution vesus (vs.) frequency ω for solid, liquid and viscous liquid. T_1 is shortened when the shaded area is increased by imaging at lower ω_0. Fig 1.3(a) is from [12] and Fig 1.3(b) is from [26].

BPP theory is fairly successful in explaining the relaxation of small or simple molecules; however, it is insufficient for complicated multi-component structures, such as biological tissues.

The FETS model suggests that tissues consist of two states of water: a large free water compartment, and a bound water compartment comprised of water molecules attached to the surface of the macromolecule. These two compartments undergo rapid exchange. The observed tissue T_1 is then a weighted average of free and bound water[27],

$$\frac{1}{T_1} \approx \frac{0.05}{T_{1b}} + \frac{0.95}{T_{1f}} \sim \frac{1}{0.5s} \qquad [1.13]$$

The published relaxation data are consistent with the tissue T_1 being determined primarily by the exchange between macromolecules and the bound hydration layer, while T_2 is determined by the exchange diffusion between the bound water and the free water[27, 28].

1.3.2 Relaxation in tissue

Relaxation is dependent on tissue type, species, frequency, temperature, as well as pathology[28] [29]. Table 1 is a summary of T_1 and T_2 relaxation times in human tissues measured *in vivo* at 37°C and 3T.

Table 1.1. In vivo human tissue relaxation times from healthy volunteers at 3T

Tissue	T_1(ms)	T_2(ms)	Reference
White matter	1084±45	69±3	[29]
Gray matter	1820±114	99±7	[29]
Liver	812±64	42±3	[29]
Heart	1471±31	47±11	[29]
Kidney	1194±27	56±4	[29]
Muscle	1420±38.1	31.7±1.9	[30]
Cartilage	1240±107	36.9±3.81	[30]
Synovial fluid	3620±320	767±48.8	[30]
Marrow fat	365±9.0	133±6.14	[30]

Both T_1 and T_2 vary extensively in different body tissues. Muscle and other organs have long T_1s and short T_2s, fat has a short T_1 and a long T_2, and fluid has a slow relaxation in both T_1 and T_2. The empirical fitting generates T_1 frequency dependence as

$T_1 = A\omega_0^B$, where A and B are tissue-dependent constants. T_2 appears essentially independent of frequency in the MRI frequency range 1-100 Hz [28].

Relaxation changes in pathological tissues primarily due to the changes in tissue components, including alterations in the proportions of the components, changes in structural and its constituents. For instance, with edema, white matter T_2 may be elongated because of the formation of intramyelin vacuole[31]; peripheral nerve system (PNS) disease causes demyelination, reducing the short T_2 component and consequently the overall T_2 may increase[32]. Malignant tumors result in "less ordered" (i.e., higher motion frequency) tissue water, and thus, a longer T_1 [33]. Atherosclerosis deposits lipid (low relaxation times), fibrosis, and calcium (dephasing local water molecule faster), and may therefore yield a lower T_1, T_2, and PD[34].

1.3.3 Conventional methods of measuring the relaxation times

In this section, two conventional methods of measuring T_1 and T_2 are introduced. They always serve as gold standard T_1 and T_2 mapping methods, although many more efficient novel techniques have been developed.

1.3.3.1 Spin-echo T_2 measurement

The spins produce a FID signal after an excitation that tips them into the transverse plane. FID decays with a decay constant called T_2*, which is much shorter than T_2. The T_2* dephasing is caused by the external B_0 field inhomogeneity, in additional to the dipole-dipole interaction. To measure the intrinsic T_2, the "spin echo" (SE) sequence was invented[13] to reverse the dephasing caused by the B_0 inhomogeneity (Fig 1.4).

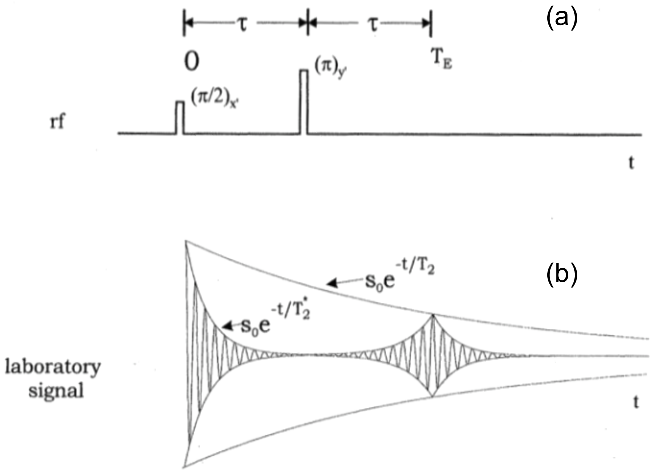

Fig 1. 4 (a) The spin echo pulse sequence diagram. First, a 90° excitation pulse is applied along the x' axis. After a certain time period τ, a 180° "refocusing" pulse, is applied along the y' axis. This refocusing pulse will invert the accumulated phase to the opposite direction in the x'-y' plane. Thus, at time 2τ, the spins will "rephase" and create an "echo" signal. The echo time is called "TE." The corresponding signal is plotted in (b). The FID follows T_2* decay, but the spin echo amplitude is determined by T_2. Fig 1.4 is from [23].

To improve the accuracy and efficiency of the T_2 mapping, some variations of spin echo sequences have been developed. One well-known sequence is called the Carr-Purcell-Meiboom-Gill (CPMG) [35]. This sequence adds a train of equally spaced refocusing pulses after excitation. It is considered to be the most accurate T_2 measurement and is used as the gold standard method for measuring T_2 in this thesis.

1.3.3.2 Partial saturation T_1 measurement

To acquire data for the full image k-space, a pulse sequence is repeated with a repetition time (TR). If TR is comparable to or shorter than T_1, the excited spins will not reach their equilibrium before the next excitation. If TR>>T_2, there will be no transverse signal left at the end of each TR. If M^- is the M_z just prior to the excitation, and M^+ is the M_z after excitation, then, $M^+ = M^- \cos\theta$. After many TRs, the system will reach a steady state, with constant M^- and M^+. At the steady state, substituting time t = TR in [1.9], with $M_z(TR) = M^-$ and $M_z(0) = M^+ = M^-\cos\theta$, M^- can be solved as

$$M^- = \frac{M_0(1-E_1)}{1-E_1\cos\theta} \quad [1.14]$$

where $E_1=\exp(-TR/T_1)$.

Suppose the system is in the steady state, and the signal readout occurs shortly after excitation such that, there is negligible signal decay in the transverse plane. Then the signal amplitude is $M^-\sin\theta$, which may be acquired as a function of T_1. By acquiring images with variable TRs, T_1 and M_0 are thus solvable with the known FA. When FA $\theta=90°$, this T_1 measuring method is called “Partial Saturation (PS)”, and is used as a gold standard in this thesis.

Many other fast and efficient methods of measuring T_1 and T_2 have been published recently. Those methods will be discussed and compared in the following chapters as well.

1.4 Contrast Maximization in MRI

In this section, the contrast mechanism in MR images is introduced. The effect of T_1, T_2 and PD on image contrast and the relationship between contrast-to-noise ratio (CNR) and visibility are discussed. The concept of contrast agents is also briefly described.

1.3.1 MRI contrast

SNR and CNR are two important metrics with which to evaluate the quality of medical images. SNR measures the signal relative to the noise generated by random voltage fluctuation from the hardware and from the sample. CNR measures how much the signal from diseased tissue differs from that of normal tissue also relative to the noise. The CNR between two tissues A and B is defined as $CNR_{AB} = \frac{S_A - S_B}{\sigma_0} = SNR_A - SNR_B$, where S_A and S_B are the voxel signal amplitudes from the two tissues, σ_0 refers to the standard deviation (SD) of noise.

How much CNR is needed for disease detection? According to the Rose Criterion, based on empirical exams, observers are able to detect objects in the image with an SNR threshold of 3-5 [36]. We can apply similar criteria to the CNR. Suppose S_A and S_B follow Gaussian distributions with the same SD and CNR=4, it can be shown that the probability of the observer to make an error in tissue detection is less than 2.5%[23].

As we know, the contrast of almost all MR images is governed by T_1, T_2, and PD. Signals acquired using different sequences follow different formulas containing the three parameters in accordance with the solution of the Bloch equation [1.3]. Here, we focus on a wildly used sequence called the gradient echo (GRE) as an example for understanding the contrast expression. The GRE sequence refocuses the dephased spins by applying a reverse gradient to form an echo. The GRE signal decay follows T_2*. Assuming $TR \gg T_2^*$, the contrast C_{AB} between S_A and S_B in a GRE image thus becomes

$$C_{AB} = S_A(TE) - S_B(TE) = M_{0A}(1 - e^{-TR/T_{1A}})e^{-TE/T_{2A}^*} - M_{0B}(1 - e^{-TR/T_{1B}})e^{-TE/T_{2B}^*} \quad [1.15]$$

Thus, C_{AB} can be optimized by suitable choice of TR or TE or both.

1.3.2 Contrast maximization

Tissue contrast in MRI can result from the differences in some or all of T_1, T_2, and PD. Here, three basic forms of MRI contrast are introduced: T_1-weighted; T_2 (or T_2*)-weighted; and PD-weighted contrast. PD measures the proton density, T_1 is powerful in showing soft tissue anatomy, and T_2 is often a good indicator of fluid and disease[37-39].

To create a PD-weighted image, it is necessary to minimize the signal dependence on T_1 and T_2. Intuitively, spins should reach their equilibrium at the end of each TR cycle, which would eliminate the T_1-weighting. In addition, the signal should be acquired shortly after excitation to eliminate T_2 decay, i.e., TR>>T_1 and TE<<T_2*. In this case, [1.15] becomes $C_{AB} \square M_{0A} - M_{0B}$.

Similarly, to yield a T_1-weighted image, the T_2 weighting should be minimized by reducing TE to <<T_2. A short TR that is comparable to T_1, can be used to enhance T_1 contrast. To acquire T_2- or T_2*-weighted images, TR is generally set to >>T_1, and TE kept comparable to T_2. However, in T_{1-} and T_2-weighted images, the PD dependence generally cannot be eliminated.

In pure T_1- (or T_2-) weighted images, to optimize the contrast between two specific tissues, TR (or TE) should be calculated carefully by substituting the T_1 (or T_2) values and PD values into Eq. [1.15] and finding the maxima. In a more general case, the optimum contrast is achieved in an image that optimizes all three weightings of T_1, T_2, PD, with both TR and TE being solved simultaneously. In other words, if there is a 3D coordinate system with each axis corresponds to one of these parameters, we want to find a hyper plane in the space to separate two (or more) different tissues. The normal direction of that plane indicates the combination of the three contrasts (T_1, T_2, PD) with which the two (or more) tissues can be most clearly separated, to achieve maximum contrast.

1.3.3 Contrast enhancement with a contrast agent

For a tissue of interest that has T_1, T_2 and PD very close to those of the surrounding tissue, or that is too small to identify due to the MRI spatial resolution, a contrast agent (CA) is often introduced to improve visibility. A CA can be directly injected into the body intravascularly or interstitially, or used as a label that binds to a target molecules' surface[40].

Based on the magnetic properties and image effects, CAs can be classified into several major classes: paramagnetic CAs, superparamagnetic CAs, "heteronuclear" CAs, etc. Paramagnetic CAs, such as gadolinium (Gd^{3+}) and manganese (Mn^{2+}), possess one or more unpaired electrons, resulting in a strong magnetic moment, thousands of times larger than that of water molecule protons. The magnetic dipole interaction between the CAs and surrounding protons will expedite relaxation, and thus, reduce the T_1 of the water protons, causing a signal increase in the T_1-weighted image.

Superparamagnetic CAs are often referred to as small superparamagnetic iron oxide (SPIO). They consist of very small magnetic crystallites. These crystallites have much larger magnetic moments than paramagnetic CAs. They produce a highly-localized magnetic field gradients, which cause a rapid T_2 decay. Hence, SPIOs result in dark areas at target sites in T_2-weighted MRI. In cell-tracking, SPIO particles have been most widely used. However, the reduced signal can always be confused with other attenuation effects, such as the iron in blood or blood clots[41]. It also induces strong field distortion to the underlying MR anatomy. Moreover, CAs that generate positive signals are preferable for cell visibility.

Recently, ^{19}F-based labeling probes have been developed as heteronuclear CAs. Due to the near non-existence of naturally abundant ^{19}F in native mammalian bodies, cells labeled as ^{19}F nuclei will be visible in ^{19}F MRI with no background signal from the tissue. The ^{19}F signal strength is directly proportional to the number of ^{19}F nuclei present in the label, which also enables cell number quantification[3].

Chapter 2. Measuring and Imaging T_2 using Dual-τ Method with No Spin-echoes, and preliminary results with Dual-τ-dual-FA Method

2.1 Introduction

The transverse component of the nuclear magnetization can undergo T_2 decay even during excitation. The T_2 decay depends on the pulse length τ. Here, this property is exploited in a new, "Dual-τ" method of measuring T_2 using the ratio of NMR signals acquired with short and long-duration excitations, using self-refocusing adiabatic pulses. This method uses no SEs. The Dual-τ method is implemented with B_1-insensitive rotation (BIR-4) pulses, and validated theoretically with Bloch Equation simulations independent of FA, and experimentally in phantoms. Dual-τ T_2 measurements are most accurate at short T_2 where results agree with standard spin-echo measures to within 10% for $T_2 \leq 100$ms. Dual-τ MRI performed with a long 0° BIR-4 pre-pulse provides quantitative T_2 imaging of phantoms and humans while preserving desirable contrast and functional properties of the rest of the MRI sequence. A single 0° BIR-4 pre-pulse can provide T_2 contrast-weighted MRI and serve as a "T_2-prep" sequence with a lower B_1 requirement than prior approaches. Finally, a Dual-τ-dual-FA experiment is introduced in which both τ and flip-angle are varied, enabling measurement of T_2, T_1 and signal intensity in just three acquisitions if flip-angles are well-characterized. These new methods can potentially save time and simplify relaxation measurements and/or contrast-weighted NMR and MRI.

2.1.1 Adiabatic pulse

The term *adiabatic* as applied to NMR excitation pulses refers to frequency and/or amplitude modulated pulses whose effective B_1-field in the frame-of-reference rotating at the Larmor frequency change sufficiently slowly such that the nuclear magnetization M is able to follow it without inducing transitions[42, 43]. Adiabatic pulses are highly-valued for their insensitivity to RF and B_0 inhomogeneity over ranges determined by the pulse duration τ, flip-angle θ, and B_1 amplitude and frequency sweep (with maximum frequency, f_{max}) [44]. The duration of the pulses is supposed to be shorter than any relaxation processes–whence the term, *fast passage*.

In the classic experiment, the frequency was swept linearly through resonance [42, 43]. Nowadays, adiabatic full-passage (AFP; $\theta = 180°$) and half passage (AHP; $\theta = 90°$) pulses with $B_1(t)$ amplitude/frequency-sweeps that vary as *sin*/*cos*, *tan/tanh* and *sech/tanh*, offer far superior B_1-performance [43-46]. The B_1-insensive rotation (BIR-4) pulse, which combines four AHP segments, has further extended adiabaticity to flip-angles that can be arbitrarily pre-set anywhere in the range $|\theta| \leq 180°$ [47]. The BIR-4 flip-angle is set by means of two phase-jumps between the segments, which can be phase-cycled to improve accuracy [48].

All of these pulses, and especially the BIR-4 pulses, are intrinsically longer than conventional hard pulses. To the extent that the magnetization M evolves in the transverse plane during the pulse, it is subject to transverse T_2 decay, even when the pulses are self-refocusing [44, 49, 50]. This dependence is potentially exploitable for measuring T_2, or for enhancing T_2 contrast. To date, except for the use of spectral linewidths, T_2 has been measured with NMR SEs. The most accurate T_2 measurements are derived from the CPMG technique [35]. SEs are routinely used to provide critically important T_2-dependent contrast and T_2 measurements in clinical diagnostic magnetic resonance imaging (MRI)[51].

Here we present a new approach for measuring T_2 in NMR and MRI, and for providing T_2 contrast in MRI, that does not use SEs. Instead, the T_2 dependence of adiabatic pulses is harnessed to measure T_2 by repeating the NMR or MRI acquisition sequence using one or more different adiabatic pulse lengths τ. We introduce the Dual-τ method, which provides a T_2 measurement from the ratio of NMR signals acquired with short- and long-duration adiabatic pulses. This is analogous to the *dual-angle* method for measuring the T_1 relaxation time from the ratio of signals acquired with two BIR-4 pulse flip-angles. Indeed, addition of a third acquisition permits the measurement of *both* T_2 and T_1 using a combination of different pulse lengths and flip-angles in the Dual-τ-dual-FA method, also introduced herein. Both the Dual-τ and the Dual-τ-dual-FA methods are implemented with self-refocusing BIR-4 pulses and validated by Bloch equation simulations, and by experimental studies of phantoms whose T_2s and T_1s are measured by standard CPMG SE and PS methods. The simulations provide a look-up table or curve which is used to convert measured signal ratios into T_2 values. T_1 is determined from a formula analogous to that used for the *dual-angle* method [52].

2.1.2 “T_2 prep”

Because adiabatic pulses are generally unsuitable for spatially-selective excitation in MRI, implementation of the Dual-τ method in imaging is most easily accomplished by addition of a 0° BIR-4 pre-pulse to the conventional MRI sequence. Since a 0° pulse does not otherwise affect the nuclear spin dynamics, other desirable MRI contrast and functional properties built into the sequence that follows the pre-pulse can be preserved. A single 0° BIR-4 pre-pulse of length τ can provide T_2-contrast or T_2-weighted MRI, as well as "T2-prep" (T2-preparation) MRI with a lower B1 threshold than T2-prep sequences employing AHP and AFP pulses[53]. Quantitative Dual-τ T2 imaging can be performed by applying MRI sequences with and without the 0° *τ* pre-pulse. The Dual-τ T2 MRI method is validated with studies of phantoms and the human foot by comparison with standard CPMG methods.

2.2 Theory

2.2.1 Dual-τ Method

The M_z and M_{xy} are affected by both T1 and T2 relaxation following a long adiabatic pulse [50]. At the end of an adiabatic pulse with FA=θ (time 0^+), $M_z(0^+) = \cos\theta M_z(0^-)E_p^z$ and $M_{xy}(0^+) = \sin\theta M_{xy}(0^-)E_p^{xy}$, as compared to the start of the pulse (time 0^-). Here E_p^z and E_p^{xy} are longitudinal and transverse attenuation factors, which are functions of *τ*, T2, B1 and the maximum frequency sweep, f_{max}, of the pulse, but not T1 as long as τ<<T1. After self-refocusing at the end of the adiabatic pulse, the T2 decay can be written as $E_n^{xy} = e^{-g.\tau/T}$, where *g* is a parameter reflecting the fraction of time spent by the magnetization in the transverse plane during the pulse. Numerical analysis of the Bloch equations for T2 ≤ 200ms with BIR-4 pulses of duration τ <40ms (see methods, below) shows that $E_p^z = E_p^{xy}$. We thus denote $E_n = E_n^z = E_r^x$.

If the residual transverse magnetization prior to time 0^- is crushed [54], the steady-state magnetization after a sequence of adiabatic pulses applied at a TR comparable to T1 is [50]:

$$M_z^{\infty}(0^+) = M_0 \frac{(1-E_1).\cos\theta.E_p}{1-\cos\theta.E_p.E_1}\,;\; M_{xy}^{\infty}(0^+) = M_0 \frac{(1-E_1).\sin\theta.}{1-\cos\theta.E_p.} \qquad [2.1]$$

where $E_1 = e^{-TR/T}$ and M_0 is the equilibrium nuclear magnetization. If θ =90°, the application of two such sequences with the same TR but two different pulse durations τ_1 and τ_2, will produce steady-state signals

$$M_{xy}(\tau = \tau_1) = M_0(1 - E_1)E_{p1}^{xy} \text{ and } M_{xy}(\tau = \tau_2) = M_0(1 - E_1)E_{p2}^{xy} \ .$$

The ratio of these signals is:

$$R = \frac{M_{xy}(\tau=\tau_1)}{M\ (\tau=\tau\ )} = \frac{M_0(1-E_1)E_{p1}}{M(1-E)E} = \frac{E}{E} \qquad [2.2]$$

where E_{p1} and E_{p2} are the attenuation factors for the two pulses. Thus, R is just a function of T_2 which can be derived numerically from the known B_1 and f_{max}.

2.2.2 Dual-τ-dual-FA T_2 and T_1 measurements

The Dual-τ method is limited by the choice of θ =90° required to cancel the coefficient of E_p in the denominator of Eq. [2.1] for short TR. Incomplete cancellation can occur due to pulse imperfections, incomplete dephasing of residual transverse magnetization, and/or deviations in E_p as TR approaches T_2. Achieving perfect 90° pulses is often problematic for *in vivo* applications such as MRI where the pulses are slice-selective and the RF fields are seldom uniform across the slice. While increasing TR can alleviate this problem, long TRs generally reduce the SNR ratio per unit time and increase the scan time. We have overcome these limitations by adding a third acquisition to accommodate both θ<90° pulses and short TRs. Importantly, the additional acquisition can permit a simultaneous determination of T_1 and T_2.

We call this the Dual-τ-dual-FA method, in which: 1) a first signal S_1 is acquired with a conventional short α RF excitation pulse without adiabatic excitation; 2) a second signal S2 is excited by a β° adiabatic pulse of duration τ_2; and 3) a third signal S3 is excited by a β˚ adiabatic pulse of length $\tau_3=2\tau_2$. The three steady-state signals are:

$$S_1=\frac{(1-E_1)\sin\alpha}{(1-E_1.\cos\alpha)}M,\quad S_2=\frac{(1-E_1)E_{p2}\sin\beta}{(1-E_1E_{p2}\cos\beta)}M_0 \text{ and } S_3=\frac{(1-E_1)E_{p3}\sin\beta}{(1-E_1E_{p3}\cos\beta)}M_0 \quad [2.3]$$

Using the same B1 and f_{max} for both adiabatic pulses yields $E_p=e^{-g\cdot\tau/T_2}$, $E_{p3}=E_{p2}^2$, and the equation set simplifies to a quadratic:

$$aE_{p2}^{2}+bE_{p2}+c=, \qquad [2.4]$$

where $a=S_1\sin\beta\cos\beta\sin\alpha(S_3-S_2)$, $b=S_1S_2\sin\alpha\cos\alpha\sin\beta-S_2S_3\sin^2\alpha\cos\beta$, and $c=S_2S_3\sin^2\alpha\cos\beta-S_1S_3\sin\alpha\cos\alpha\sin\beta$.

Choosing the root of Eq. [2.4] that falls in the interval (0, 1) yields the T2 attenuation factor

$$E_{p2}=\frac{-b\pm\sqrt{b^2-4a}}{2a}. \qquad [2.5]$$

Substitution of Eq. [2.5] into Eq. [2.3] yields the T1 attenuation factor

$$E_1=\frac{S_2\sin\alpha-S_1\sin\beta E_{p2}}{(S_2\sin\alpha\cos\beta-S_1\cos\alpha\sin\beta)E_{p2}} \text{ or } E_1=\frac{S_3\sin\alpha-S_1\sin\beta E_{p3}}{(S_3\sin\alpha\cos\beta-S_1\cos\alpha\sin\beta)E_{p3}} \qquad [2.6]$$

This is basically the *dual-angle* equation [52] with an E_{p2}-attenuation correction. Thus, from E_{p2} and E_1,

$$T_2=-\frac{g.\tau_2}{\ln(E_{p2})} \quad \text{and} \quad T_1=-\frac{TR}{\ln(E_1)}. \qquad [2.7]$$

2.3 Methods

2.3.1 Numeric simulations

Simulations of the Bloch equations were performed using Matlab (Mathworks, Natick, MA)[55]. The evolution of magnetization was simulated for proton (^1H) relaxation at 3T over the range $20 \leq T_2 \leq 200$ms and $0.1s \leq T_1 \leq 1s$ for BIR-4 pulses with B_1=20μT and f_{max}=15kHz, as used in experiments. Pulses were defined at 5μs intervals with lengths varying from $1 \leq \tau \leq 40$ms, a practical range given limitations in RF pulse power and power deposition. Adiabatic pulse flip-angles were varied from $0 \leq \theta \leq 90°$. The simulations were used to derive the attenuation factors, E_p^z and E_p^{xy} after long BIR-4 pulses, decay parameter g, and the corresponding signal ratio R, as a function of T_2, T_1, τ, and θ in the Dual-τ experiment.

Monte Carlo simulations were performed to evaluate the sensitivity of Dual-τ and Dual-τ-dual-FA measurements, to noise. The SD of the noise was set at 2% of the signal strength (SNR=50) elicited by each pulse. The signals, their ratio R for the Dual-τ T_2 experiment, and the solutions to Eq. [2.7] for the Dual-τ-dual-FA experiment, were determined for 1000 simulations as a function of T_2 up to 80ms in the Dual-τ and Dual-τ-dual-FA experiments, and $0.1s \leq T_1 \leq 1s$ for the Dual-τ-dual-FA experiment. Note that T_2 measured by the Dual-τ experiment is unaffected by TR for perfect $\theta = 90°$ pulses.

2.3.2 Phantom construction

Twelve phantoms with tissue-comparable relaxation times were prepared with agarose (Type 1-A CAS 9012-36-3: Sigma Chemical, St. Louis, MO, USA) and $CuSO_4$ (CAS 7758-99-8: Acros organics, Geel, Belgium) in de-ionized distilled water. Both agarose and $CuSO_4$ shorten the T_1 and T_2 of pure water. However, agarose decreases T_2 more effectively than $CuSO_4$, which more strongly affects T_1. The concentrations of

$CuSO_4$ and agarose were adjusted from 0.2 to 1.6g/l and 10 to 110 g/l respectively, to provide phantoms with $10ms<T_2<130ms$, and $0.15s<T_1<1.0s$ [56]. The ingredients were mixed in a beaker and heated in a microwave oven to dissolve the agarose without introducing too many bubbles. The hot solutions were then sealed to occupy 9cm of 12cm- long, 25mm inner diameter (ID) plastic tubes and allowed to cool and gel.

2.3.3 NMR measurements

All NMR and MRI measurements were done on a 3T Achieva MRI scanner (Philips Healthcare, Best, The Netherlands) using the standard transmit/receive birdcage head coil (maximum B_1=20μT). The gel phantoms were set in a plastic foam panel in the center of the coil with long axes parallel to the z-axis. To facilitate T_1 and T_2 measurements, NMR data were acquired with one-dimensional chemical shift imaging (1D CSI, 5mm resolution; acquisitions per frame, NEX=1) from five aligned phantoms at a time. In all measurements involving BIR-4 pulses, the flip angles were calibrated at the pulse lengths being tested. Dual-τ T_2 was measured with two 90° BIR-4 pulses of lengths τ_1=5ms (f_{max} =12kHz) and τ_2=35ms (f_{max} =15kHz), the shortest TE (1.8ms) and TR=4s.

Reference T_2 and T_1 relaxation times were measured at 3T using standard SE and PS NMR methods, respectively. Individual SE data was obtained using 1D CSI with 8 different echo times (TE=14, 30, 50, 75, 100, 150, 200, 300ms), and TR set to 4.0s to allow for complete signal recovery. T_1 was measured using PS sequences with TR =0.25, 0.5, 1, and 3s. Because relaxation times can change slowly over time, these measurements were repeated whenever a dual- or Dual-τ-dual-FA study was done.

CSI yielded approximately 5 slices in the CSI direction from each phantom. The FID signals acquired from the three middle slices in each phantom were fitted using jMRUI software (available from www.mrui.uab.es)[57] to determine the peak areas.

These values were used to determine the signal ratio at the two τ values. Dual-τ T_2 was then determined from a look-up curve generated by the numerical analysis (see Results mean±SD). Reference T_1 and T_2 measurements obtained by conventional SE and PS methods were determined from the same three slices by fitting the data sets to $\{w \cdot \exp(-TE/T_2)\}$ and $\{u - v \cdot \exp(-TR/T_1)\}$ with *u, v* and *w* constants. Mean reference relaxation times from the phantoms used in the Dual-τ studies are listed in Table 2.1.

Table 2.1 Numbered phantoms with their relaxation times for the Dual-τ T_2 NMR and MRI studies

Phantom No.	1	2	3	4	5	6	7	8	9	10	11	12
T_2(ms)	110	97	65	65	52	44	35	28	18	13	106	67
T_1(ms)	818	837	770	740	691	702	665	635	567	582	825	-

T_2 was measured by a 32-points SE NMR method (TE stepped by 7.21ms). T_1 was measured by PS NMR (0.1s≤TR≤1.5s). The signal within each phantom was first averaged then fit to an exponential relaxation curve.

The Dual-τ-dual-FA method was also validated in 1DCSI studies of 12x1.3cm ID and 4x2.5cm ID phantoms with $169 \leq T_1 \leq 890$ms and $31 \leq T_2 \leq 129$ms. We used $\tau_3 = 2\tau_2 = 20$ms, and TR=300ms for all experiments. Shorter TRs were limited by RF power restrictions. S_1 was acquired with a (non-adiabatic) 75μs α-hard pulse nominally set to 15°. The flip-angle was 14° for the short phantoms as determined from B_1 field profiles measured separately, and 13.5° for the long phantom. The β-pulse used to acquire S_2 and S_3 was a 60° BIR-4 pulse. The choice of the nominal α =15° and β=60° pair for the Dual-τ-dual-FA experiments was based on the *dual-angle* T_1 method [52].

2.3.4 MRI measurements

The BIR-4 pulse is unsuited to spatial localization. Thus for MRI applications, either multi-dimensional phase-encoding must be used (with generally unpalatable scan times), or the BIR-4 pulse must be applied in conjunction with an additional spatial localization pulse. We adopt the latter approach by adding a 0° BIR-4 pulse before the slice-selective pulse in a standard GRE MRI pulse sequence. This is based on numerical analysis showing that the effect on E_p of the BIR-4 pulse is independent of θ (see results).

Dual-τ MRI was performed on the phantom set with a two-dimensional (2D) GRE MRI sequence and 0° BIR-4 pulses with the same τ, f_{max} and B_1 used in the NMR experiments (acquisition matrix, 152 x154; field-of-view, FOV=97x10x230 mm^3; slice thickness=10mm; TR=2s; minimum TE=2.5ms). The delay between the BIR-4 and (1ms) slice-selective pulses was 1.5ms. Because the excitation pulse and inter-pulse delay are unchanged in this Dual-τ MRI experiment, the same curve from the numerical analysis was used to obtain T_2. The sequence timing diagram is shown in Fig 2.1. Reference T_2 values from conventional MRI were obtained from the phantoms using a 3D 32-echo sequence (TE step =7.21ms, TR=461ms, 2.5ms excitation pulse 1.5ms after the BIR-4 pulse). T_2 was measured in images by determining the ratio R on a pixel-by-pixel basis for the Dual-τ method, and by fitting the SE pixels to an exponential to obtain reference T_2 images. Pixel-average T_2 values within each phantom are reported.

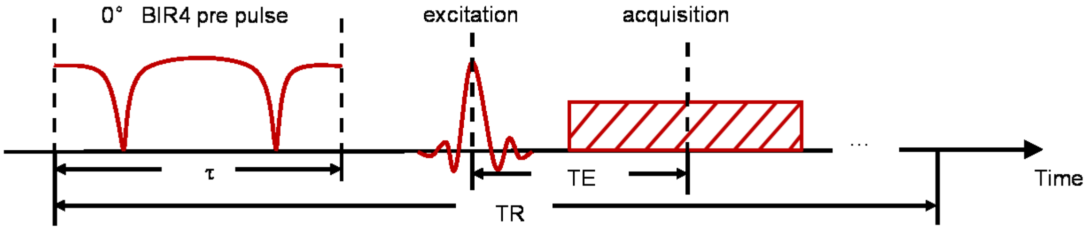

Fig 2.1 Timing diagram of a sequence employing one of 0° BIR-4 pre-pulses for the Dual-τ MRI method. In MRI experiments TE was set to a minimum (4.8ms), TR at 2s, and the gap between the pre- and excitation-pulses was ~1.5ms.

Human studies for this project were approved by the Johns Hopkins Institutional Review Board. The foot was chosen based on the expected short T_2s of muscle and cartilage [30], for which analysis showed the Dual-τ method to be well-suited. A healthy volunteer was positioned supine with the foot in the head coil, and Dual-τ T_2 MRI performed using two acquisitions of a coronal 3D GRE sequence, one employing a 0° BIR-4 pre-pulse (matrix size, 112x112; slice thickness =6mm; FOV = 42x100x100 mm^3, TR =2s, TE =4.1ms =minimum). Reference T_2 MRI of the foot was performed with the 32-echo sequence (same matrix, slice thickness and FOV as for Dual-τ GRE; TE step =5.39ms; TR=625ms). T_2 images and average T_2 values were calculated the same way as in the phantom studies.

2.4 Results

2.4.1 Numeric simulations

The attenuation factor, E_p as a function of T_2 is plotted in Fig 2.2 for four BIR-4 pulses of duration 5-35ms. The curves all fit accurately to the exponential $E_p(T_2) = \exp\left(-0.81\frac{\tau}{T_2}\right)$. In this case, g =0.81. This result is independent of flip-angle for 0°≤θ≤90° and for long TR, reflecting the fact that the BIR-4 flip-angle is set by two opposite phase-jumps of duration <<T_2 and T_1. In the adiabatic region wherein θ is independent of B_1, g is relatively insensitive to f_{max}, for example, varying by <4% for 12kHz $\leq f_{max} \leq$15kHz and B_1=20μT.

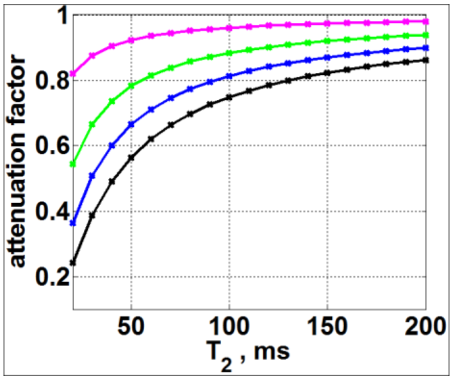

Fig 2.2 Numerical simulation of the attenuation factor E_P=|M|/M_0 after a BIR-4 pulse of duration 5ms (magenta), 15ms (green), 25ms (blue) and 35ms (black), as a function of T_2 from 20 to 200ms (T_1 =1s, TR = ∞ for complete longitudinal relaxation). The curves are exponential fits to stars are the numerically-determined points.

The sensitivity and accuracy of the Dual-τ T_2 experiment are improved by selecting BIR-4 pulses with very different pulse lengths, notwithstanding RF power constraints. Pulses shorter than 5ms have little attenuation but are limited by peak pulse power. Long pulses are limited by the RF power amplifier's ability to sustain the pulse, as well as by the spectral bandwidth of the sample. The ratio of the signals from the τ_1=5ms and τ_2=35ms pulses is plotted in Fig 2.3(a). The curve is fit by $R(T_2) = \exp(-24.3 / T_2)$ independent of θ. Sensitivity is maximum over the steepest (short-T_2) region of the curve, with the τ_1/τ_2 =5/35ms pair providing reasonable T_2 resolution up to 70 or 80ms. Thus, T_2 can be read from Fig. 2.3(a) using the measured signal ratio. The variation in T_2 determined from the ratio curve is plotted as a function of

T_1 in Fig. 2.3(b). The result varies by <1% for 0.6s $\leq T_1 \leq$1.0s, and <6% for 0.2s $\leq T_1$ $\leq$1.0s.

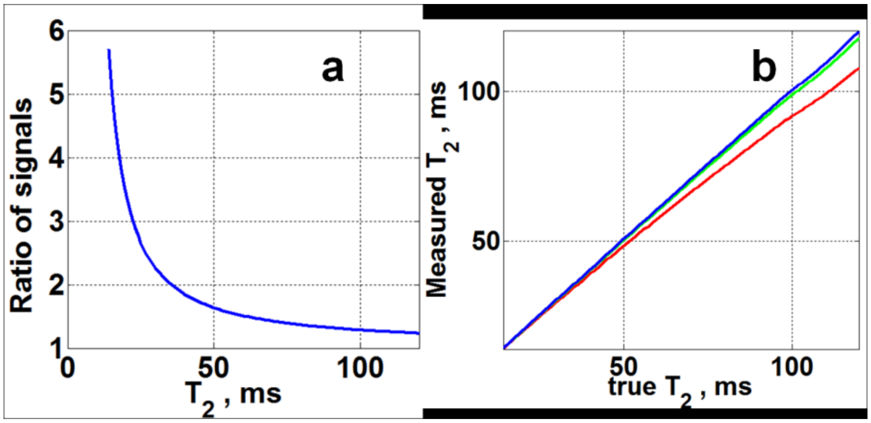

Fig 2.3(a) Computed ratio *R* of two signals acquired with adiabatic pulses of length τ=5 and 35ms as a function of T_2. The curve has the form $R(T_2)=\exp(-24.3/T_2)$. (b) Dual-τ T_2 determined from part (a) as a function of T_1 (red, T_1=0.2s; green, T_1=0.6s; blue, T_1=1.0s). The result is independent of TR.

The results of the Monte Carlo simulations are exemplified in Fig. 2.4. For the Dual-τ T_2 experiment performed with τ_1/τ_2 =5/35ms pulses and signals with 2% SD, the errors are essentially independent of TR for 0.1s $\leq$TR $\leq$1.0s. Over this range, the mean error in T_2 is less than 6% ±9%(SD) of T_2 for $T_2 \leq$80ms and 0.3s$\leq T_1 \leq$1s (Fig. 2.4a). On the other hand, the simulated Dual-τ-dual-FA experiment with $\tau_3=2\tau_2$=20ms is less accurate on average, with a mean error varying from -13% to +6% of T_2 (with up to ±30% SD scatter) for $T_2 \leq$80ms over the ranges 0.1s $\leq$TR $\leq$1.0s and 0.1$\leq T_1 \leq$1s (Fig. 2.4b). When τ_3 is set to 35ms–the same as τ_2 in the Dual-τ experiment–the mean error decreases to <13% ±17%(SD) of T_2 for the same T_1s and TRs (eg, Fig. 2.4c).

The accuracy of T_1 in the Monte Carlo simulations of the Dual-τ-dual-FA experiment is better than 1% of T_1 with a 9-15%(SD) scatter, essentially independent of pulse length for $0.3 \leq T_1 \leq 1$s and $30 \leq T_2 \leq 130$ms, as shown in Fig. 2.4(d) for TR=0.3s. At shorter T_1s (<TR), the scatter in T_1 increases as the long TR becomes sub-optimal for measuring T_1 [8]. Then, reducing TR to 0.1s, reduces the scatter back to 9-15% of T_1 for $0.1 \leq T_1 \leq 1.0$s.

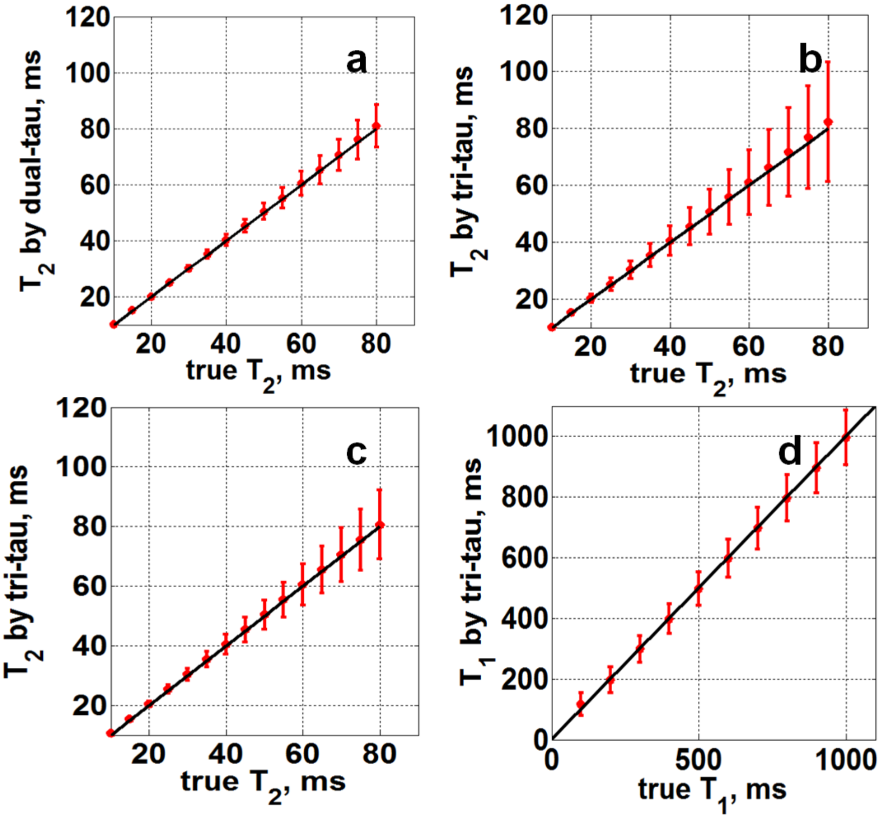

Fig 2.4 Monte Carlo simulations of the error in (a) Dual-τ T_2 with τ =5ms and τ =35ms; (b) Dual-τ-dual-FA T_2 with $\tau_3 = 2\tau_2 = 20$ms; and (c) with $\tau_3 = 2\tau_2 = 35$ms; and (d) Dual-τ-dual-FA T_1 with $\tau_3 = 2\tau_2 = 20$ms, T_2=40ms, and TR=300ms. Points are means ±SD for a 2% root-mean-square noise in each signal measurement (SNR=50) from 1000 runs with T_1=1s. The mean and SD of the T_1 measured by a Dual-τ-dual-FA experiment with $\tau_3 = 2\tau_2 = 35$ms differs from (d) by less than 1%.

2.4.2 Experiments

Results from the ^{1}H 1D CSI Dual-τ validation experiments on the 10 phantoms are plotted in Fig. 2.5. The T_1 of these phantoms was 0.6–0.8s (Table 2.1). The T_2s were determined from Fig. 2.3. Below T_2=70 ms, Dual-τ T_2 values differ from SE values by ≤3%.

Dual-τ T_2-weighted and T_2-image results from the phantoms are shown in Fig 2.6. The phantoms are labeled with the corresponding average T_2 values measured by standard 32-echo SE MRI (Fig. 2.6a), and by Dual-τ MRI (Fig. 2.6b). The T_2 values agree with the SE results within 5% up to 70ms, and 10% up to 100ms. Dual-τ and standard SE T_2 MRI of the foot are compared in Fig 2.7. Muscle T_2 values from the Dual-τ image are 29.4±1.2ms, 28.2±1.6ms, and 30.6±1.3ms; as compared to 29.8±2.8ms, 29.8±4.7ms, and 28.8±4.7ms in the same annotated volumes in the SE image. These agree with published values for muscle of 32±2ms at 3T.[30]. In marrow, SE T_2 was 106±4.3ms as compared to Dual-τ T_2 = 135±13ms in the same volume, and a published value of 133±6ms for marrow[30].

T_2 and T_1 values measured from the Dual-τ-dual-FA experiments on phantoms are compared with SE and PS T_1 and T_2 values in Fig. 2.8. The values show good agreement for all phantoms.

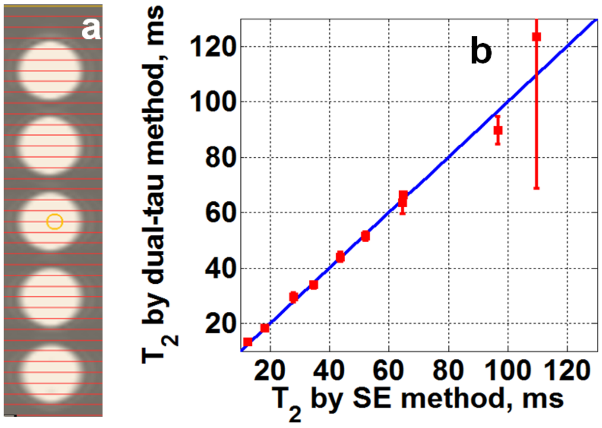

Fig 2.5(a) Transverse image of 5 of the phantoms annotated with 5mm thick 1DCSI slices (annotated in red). (b) NMR measurements of T_2 from the 10 phantoms using Dual-τ and SE methods. Filled points are the means of the middle three slices of each phantom. Error bars denote ±SD.

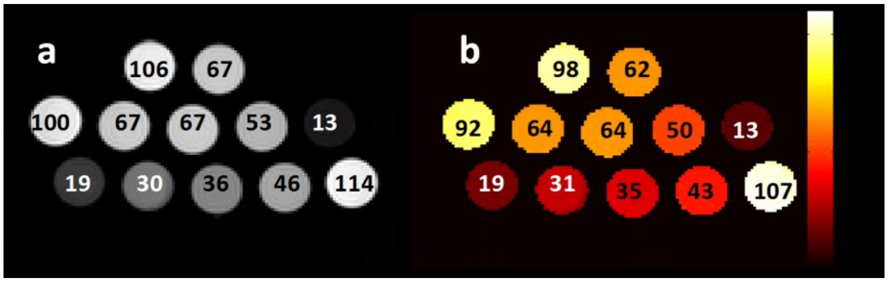

Fig 2.6(a) MRI of the phantom set, T_2-weighed by a 0° 35ms BIR-4 pre-pulse. The images are annotated with the corresponding reference SE T_2. (b) Color-coded Dual-τ T_2 image with the Dual-τ T_2 values labeled for comparison with part (a).The scale depicts T_2 in ms. The T_2 map is calculated pixel by pixel, and both images masked at the same threshold (=75% of the lowest signal in part a).

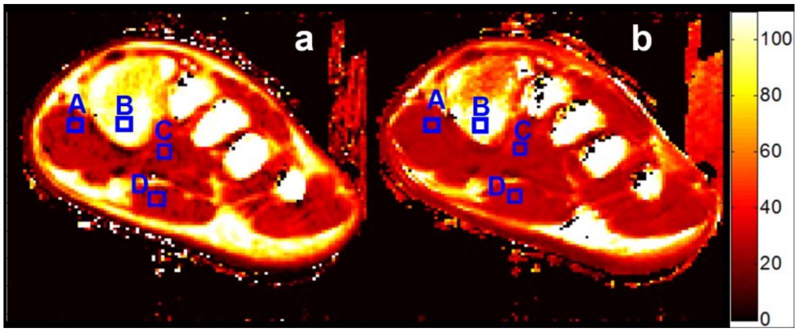

Fig 2.7 Coronal T_2 images of the human foot by the SE method (a) and the Dual-τ method (b). The scale depicts T_2 in ms. Both images are calculated pixel-by-pixel and masked by an identical threshold (SNR =4 in the raw image). Mean T_2s from the annoted squares in (a) vs (b) are: A, 29.8 ±2.8ms vs 29.4±1.2ms; B: 106 ±4.3ms vs 135 ±13ms; C: 29.8±4.7ms vs 28.2±1.6ms; D: 28.8±4.7ms vs 30.6±1.3ms.

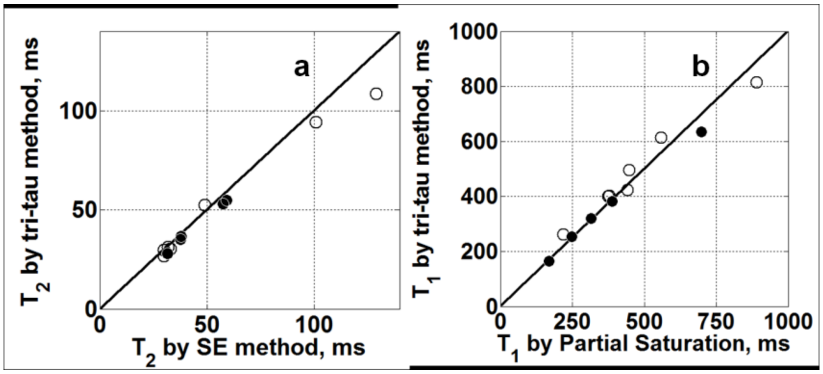

Fig 2.8 T_2 and T_1 as measured by a τ_3=2τ_2=20ms Dual-τ-dual-FA experiment from 12x1.3cm ID (empty points) and 4x2.5cm ID (filled points) phantoms, as compared with values measured using standard SE (a) and PS (b) methods (solid line =identity).

2.5 Discussion

Long adiabatic pulses such as BIR-4 are self-refocusing but are subject to T_2 decay, resulting in attenuation by the end of the pulse. We have shown for the first time that T_2 measurements and T_2 image contrast can be obtained using these adiabatic pulse properties as distinct from conventional methods that use spin-echoes or 180° refocusing pulses. In particular, we have presented new NMR and MRI pulse sequences for measuring and imaging T_2 that can be performed in just two acquisitions employing long and short duration adiabatic pulses for NMR, or a long and no adiabatic pulse for MRI. These Dual-τ methods were validated with BIR-4 pulses by numerical analysis of the Bloch Equations, and experimentally by ^{1}H NMR and MRI studies of phantoms of different T_2s and MRI of the human foot, as compared with conventional SE T_2 measurements as the reference standard (Figs. 2.4-2.6). Moreover, extension of the Dual-τ to the Dual-τ-dual-FA method resulted in a technique that not only delivered T_2 measurements but T_1 as well. The Dual-τ-dual-FA method was also validated by both simulations (Fig. 2.4) and experimental measurements on phantoms (Fig. 2.8).

As with existing techniques for measuring relaxation times, the Dual-τ and Dual-τ-dual-FA methods can be adversely affected by B_1-field nonuniformity when the adiabatic pulses are combined with conventional pulses such as those provided by MRI sequences (Fig. 2.1). The combined effect of an imperfect slice profile and B_1 inhomogeneity–to which higher-field MRI systems are intrinsically more susceptible–is significant. In order to cancel the denominator in Eq. [2.1] and obtain a ratio R from which T_2 can be determined using the Dual-τ method, we must have either θ= 90° or a long TR. Obtaining an exact θ= 90° slice-selective excitation pulse at 3T depends on the accuracy of the scanner's set-up routine. Our Dual-τ MRI studies of the foot benefited from the use of a 3D (slab-select) pulse sequence for both the Dual-τ and reference SE MRI, selection of just the middle slices, and a longer TR than we would have liked because of the uncertainty about the 90° pulse.

The delays of several milli-seconds added between the 0° BIR-4 pulse, the slice-selective pulse and the echo-times for the MRI sequences, will affect the total attenuation factor, reducing the SNR a little. This does not seem to affect T_2 in the Dual-τ MRI experiment where the delay is the same in both cases. Although the S_1 acquisition of the Dual-τ-dual-FA experiment does not have a delay while the S_2 and S_3 acquisitions do, the Dual-τ-dual-FA T_2 accuracy is also apparently unaffected.

The accuracy of T_1s measured in the Dual-τ-dual-FA NMR experiment depends critically on the accuracy of the low-angle non-adiabatic 15° NMR excitation pulses set by the scanner [52] when non-adiabatic pulses are used. If MRI is not intended, an adiabatic 15° pulse could avoid this problem provided its duration is $<<\tau_2$ to avoid a significant 3rd E_{p1} term in Eq [2.3]. Meanwhile, the accuracy of T_1 imaging using a Dual-τ-dual-FA MRI sequence wherein the 60° BIR-4 pulses are replaced by 0° BIR-4 or BIRP pulses plus nominally-60° slice-selective pulses for S_2 and S_3 with a 15° slice-selective pulse for S_1, depends on the accuracy with which B_1 and/or the flip-angles are calibrated. Nevertheless, the Dual-τ-dual-FA pulse sequence is presently *unique* in demonstrating a potential for measuring and imaging T_1, T_2 and proton density from just 3 (albeit steady-state) acquisitions–all of which are FIDs, at that.

That the decay in magnetization during the BIR-4 pulse is essentially independent of the flip-angle enables decoupling of T_2 from the flip-angle, to the point of being able to provide a T_2 attenuation effect with otherwise zero excitation. In this application, the

0° BIR-4 pulse serves as a T_2 filter, removing the short T_2 components (Fig. 2.6a), while preserving the longer ones for an FID generated by a subsequent conventional excitation. This could be useful in spectroscopy for removing unwanted short-T_2 components that generate broad baselines. Also, the use of pre-pulses to add T_2 contrast bears similarity to T_2-prep MRI sequences, especially those employing adiabatic pulses[53]. Adiabatic T_2-prep MRI uses several very short 90° AHP and 180° AFP components with gaps between them to allow T_2 relaxation[53]. By using a (i) single, (ii) long, (iii) 0° BIR-4 or BIRP pulse, (iv) with no gaps, our sequence differs from this T_2-prep sequence in four ways. Moreover, the present work extends the application from providing T_2 contrast, to providing T_2 measurements.

Conversely, the use of a single long 0° BIR-4 pulse instead of the short AHP/AFP pulses of the T_2-prep sequence[53] may offer some advantage. The single long BIR-4 (or BIRP) pulse has a much lower B_1-threshold to achieve adiabaticity than the short AHP and AFP pulses. As a consequence, it requires much lower peak power. For example, the simulations of a 45ms AHP/AFP T_2-prep sequence from Fig. 2.4a of Ref. [53]showed an adiabatic threshold requirement for B_1 of about 20μT. Performing the same simulation with the same T_1 and T_2 here, shows that use of a 45ms 0° BIR-4 pre-pulse results in a B_1 threshold that is approximately 5μT, or 1/4 that of the adiabatic T_2-prep sequence, as shown in Fig 2.9.

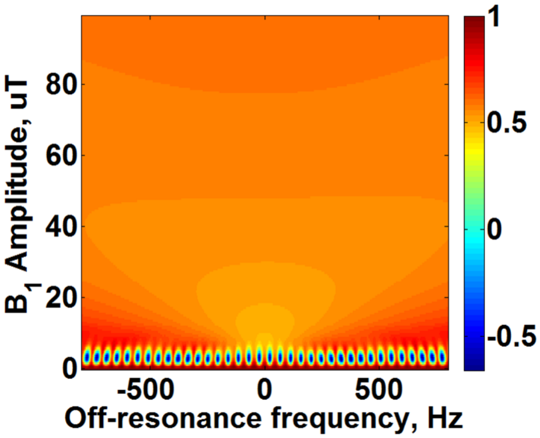

Fig 2.9 Contour plot of M_z/M_{equ} (scale at right) as a function of off-resonance frequency using a 45ms 0° BIR-4,T_1=1115ms, and T_2=55ms, for comparison with the 45ms T_2-prep sequence in Ref. [53].

Another question is whether the Dual-τ experiment with long adiabatic pulses measures either the inhomogeneously broadened T_2 (T_2*) or the T_1 in the rotating frame ($T_{1\rho}$), as distinct from a pure T_2. First, T_2* results from local B_0–field inhomogeneity or offset frequency, to which a BIR-4 pulse operating above its adiabatic threshold is insensitive over a range of several hundred Hz[52]. In the present studies, analysis shows T_2 varies by less than 6.5% for offset frequencies in the range ±300Hz, 30ms≤T_2≤130ms and TR=T_1=1s, in our commercial 3T birdcage head-coil with B_1 of 20μT. Second, $T_{1\rho}$ measures T_1 at the much lower NMR frequency corresponding to the B_1 field. Although it is not explicitly present in the Bloch Equations, $T_{1\rho}$ approaches T_2 as B_1 goes to zero, and behaves like a combination of low-frequency T_1 and T_2 [58]. As such, changes in T_1 might be expected to affect Dual-τ T_2 if it were sensitive to $T_{1\rho}$. However, analysis of the Dual-τ experiment showed variations <6% in T_2 over a 5-fold range of T_1 (Fig. 2.3b). In experiments, Dual-τ T_2 measured at a B_1 of 13.5μT (knee coil) did not differ by more than 3% from those measured with B_1 =20μT (head coil) on the same short- and long-T_2

phantoms. Thus, T_2* and $T_{1\rho}$ do not appear to be significant factors affecting Dual-τ T_2 measurements in this work.

In conclusion, the Dual-τ method provides a new option for measuring T_2 without requiring any spin echoes, at least for short T_2 tissues such as muscle, cartilage and white matter [59] where the signal ratio affords adequate T_2 resolution (Fig 2.3a). The same property delivered with an otherwise neutral 0° flip-angle self-refocusing adiabatic pulse can provide T_2-imaging, T_2-weighting, T_2-filtering (Figs. 2.6, 2.7), or T_2-prep (Fig. 2.9). At the expense of one additional acquisition, the Dual-τ-dual-FA experiment offers the potential for obtaining all of the T_2, T_1 and proton or signal density information with just three acquisitions–arguably the minimum possible–with the caveat that it requires accurate setting and knowledge of the flip-angles. These new methods can potentially save time and simplify relaxation measurements and/or contrast-weighted NMR and MRI.

Chapter 3. Minimum Acquisition Methods for Simultaneously Imaging T_1, T_2, and Proton Density with B_1 Correction and No Spin-echoes

3.1 Introduction

The ^{1}H T_2, and T_1 relaxation times of water and PD in healthy, diseased and treated biological tissue, are fundamentally responsible for image contrast and the success of MRI in medicine and biology. Nevertheless, the explicit imaging of T_1, T_2, and PD is rarely performed in clinical MRI exams, due to confounding factors affecting accuracy and to scan-time limitations. Indeed, the imaging of T_1, T_2, and PD is routinely supplanted by proxies such as T_1- and T_2-weighted image intensities. As a result, MRI scanner settings, being empirically derived, may not be optimized for contrast and detecting a particular disorder. Moreover, image intensities recorded at different MRI centers are generally not quantitatively comparable, and much potentially diagnostic T_1 and T_2 information, is simply not collected.

This is not to say that no efficient MRI relaxometry methods for jointly imaging T_1, T_2 and PD are available. Six such methods are compared in Table 3.1. Of these, those employing steady-state free-precession (SSFP) sequences (eg, “DESPOT1” and “DESPOT2”[60], “TrueFISP” T_1 and T_2[61], and “TESS”[62]) are acutely sensitive to non-uniformity in both the B_0 and the B_1. Such non-uniformities tend to increase with B_0. Although the short SSFP sequence TR saves time, the effect of B_1 errors in the excitation FA accumulates faster than in long-TR sequences, necessitating careful B_1 calibration. Short-TR SSFP is also prone to magnetization transfer (MT) errors[63]. The “FARM” method[64] (based on the “Look-locker” approach[65]), the inversion-recovery (IR) TrueFISP[61], and the IR-snapshot FLASH[66] methods sample the transient T_1 recovery curve, with acquisition strategies that can be optimized to minimize scan-time[67]. The latest "MR fingerprinting" (MRF) technique[68] also provides T_1, T_2, and PD imaging capabilities based on a look-up table of solutions to the Bloch equations obtained by numerical simulation. Accommodations in the modeling for the effects of non-uniform B_1, off-resonance, and T_2* in the absence of spin-echoes, are anticipated to be important for the accuracy of those results as well. For all approaches, the central requirements are that T_1- and T_2-dependence be imposed on the MRI signal; that this dependence be varied in repeat applications of the MRI pulse sequence; and that the resultant T_1, T_2 and/or PD-dependence can be separately deciphered from the resultant signals, thereby enabling the corresponding parametric images to be reconstructed.

Recently, we reported that self-refocusing BIR-4 adiabatic pulses[47, 49] are prone to intra-pulse T_2 decay that depends on the τ, B_1 amplitude, and f_{max} of the pulse [50]. This results from the time spent by the magnetization in the transverse plane during excitation[44]. Importantly, the T_2 decay is independent of the FA, which can be arbitrarily chosen for these pulses[47]. As a consequence, T_2-dependent attenuation of MRI signals is achievable simply by adding a long 0° BIR-4 pre-pulse to the MRI pulse sequence, leaving the sequence's other excitation properties substantially unaffected[69]. With this 'dual-τ' T_2 MRI method[69], T_2 maps were obtained without SEs, from the ratio of two steady-state signals acquired with two different pulse lengths but the same TRs. This chapter explores MRI methods that utilize this feature to image T_2, T_1, and PD in just three steady-state acquisitions, or four acquisitions if self-correction for inhomogeneity in the RF excitation field (B_1) is included. This is the minimum number of acquisitions possible.

Table 3.1 Summary of common methods for measuring T_1, T_2, and M_0. The techniques presented in this work are shaded in grey.

	Measured parameters	SteadyState (SS) or Transient	# of Acqs	TR	SSFP or SPGR	comments
DESPOT1 [60]	T_1 only	SS	2	short(6ms)	SPGR	Requires B_1 mapping.
DESPOT2 [60]	T_2 only	SS	2	short(4ms)	SSFP	Requires B_1 mapping and prior T_1 knowledge.
IR TrueFISP [61]	T_1, T_2, PD	Transient	>38	short(<6ms)	SSFP	Assumes uniform B_1, B_0.
FARM[64]	T_1 only	Transient	2	short(6ms)	SPGR	Sensitive to FA errors
TESS[62]	T_1, T_2	SS	3	21ms	SSFP	T_1 sensitive to B_1 errors
MRF[68]	T_1, T_2, M_0	Transient	1000	10-15ms	SSFP	Requires knowledge of B_1 and spiral readout.
Dual-τ Dual-FA	T_1, T_2 and PD	SS	3	609ms	SPGR	Requires B_1 mapping. Narrow T_2 range
Dual-τ Dual TR	T_1, T_2 and PD	SS	3	530/1060ms	SPGR	Requires B_1 mapping. Wider T_2 range than 'Tri-τ'.
Four FA	T_1, T_2, PD and FA	SS	4	600ms	SPGR	B_1 self-correction.

The T_1 information can be encoded into a 'dual-τ' T_2 MRI experiment by varying either the excitation FA[52, 70] or the TR [71] of the pulse sequence. This yields PD as well, but normally requires at least two more acquisitions, for a total of four. To image all three parameters–T_1, T_2, and PD–in three acquisitions, requires that both τ and either of TR or FA each be varied in at least two of the three acquisitions. Of these two options, we first evaluate the ‘Dual-τ Dual-FA’ method wherein TR is kept constant and a GRE MRI sequence is applied once with a small FA pulse, and twice more with the same large FA pulse, but preceded by either a short or a long 0° adiabatic pre-pulse. Next, the ‘Dual-τ Dual-TR’ experiment with a constant FA is evaluated. Here, a first MRI sequence is applied with a short adiabatic pre-pulse and a short TR; a second sequence is applied with a short 0° adiabatic pre-pulse and a long TR; and a third sequence uses both a long 0° adiabatic pre-pulse, and a long TR.

As with conventional methods for measuring T_1, precise knowledge of the local FA is essential for accuracy. This means that both the ‘Dual-τ Dual-FA’ and ‘Dual-τ Dual-TR’ methods would effectively require at least two additional MRI acquisitions to map B_1. While the standard B_1 mapping software on clinical scanners is well-suited to providing FA information for 3D MRI, correction for trans-slice B_1 (FA) variations in 2D MRI requires repeat acquisitions to individually calibrate each sequence when the errors are T_1-, TR-, and FA-dependent[72]. Therefore, in the final method evaluated here, the spatial FA variation is recognized as integral to a complete T_1, T_2, and PD MRI experiment. We add just one acquisition to the ‘Dual-τ Dual-FA’ method to create the ‘Four-FA’ experiment which yields T_1, T_2, PD and FA (or B_1) in just 4 acquisitions. The FA and T_1 information is extracted from GRE signals acquired with three different FAs plus a short 0° adiabatic pre-pulse, while a long 0° adiabatic pre-pulse in the fourth acquisition yields T_2. All three methods are validated *in vitro,* and the ‘Dual-τ Dual-FA’ and ‘Four-FA’ experiments are also demonstrated in human brain studies *in vivo* at 3T.

In what follows, we first describe how T_2 is encoded for all three methods using long adiabatic pulses. To avoid confusion, each method is then presented serially with its own theory, experiment, and results section. Finally, the efficiency, accuracy, and efficiency per unit accuracy are compared in Monte Carlo simulations of the 'Four-FA' method with a combined PS plus SE experiment, and with the DESPOT1/2[60], IR TrueFISP[61], and MRF methods.

3.2 Dual-τ Dual-FA Method

3.2.1 Theory

The derivation of the 'Dual-τ Dual-FA' method has been discussed in Chapter 2. It is a single steady-state acquisition is added to the dual-τ T_2 experiment to encode T_1. Here we will extend the NMR validation of this method to a full scope quantification evaluation including numerical simulations, *in vivo* and *in vitro* MRI measurements, and comparison with other quantification methods.

The three acquisitions use the same TR, but are applied with two different excitation FAs, α and β. This part of the experiment is analogous to the dual-angle T_1 method[52] where $\alpha=15^{\circ}$ and $\beta=60^{\circ}$ were found to yield both useful T_1-sensitivity and SNR.

The 'Dual-τ Dual-FA' acquisitions specifically comprise: (A1) a first signal S_1 excited by a conventional GRE MRI sequence with a short-α RF excitation pulse. In step (A2), a second signal S_2, is excited by a 0° adiabatic pulse of duration τ_2, followed by a GRE sequence with a FA of $\beta > \alpha$ excitation pulse. A third signal S_3, is excited in step (A3) by a 0° adiabatic pulse of duration $\tau_3=2\tau_2$ followed by a GRE sequence, also with FA=β. As noted above, adding a short (eg, 1ms) 0° adiabatic pre-pulse in step A1, is prudent to control for the effects of the delay between the pre-pulse and signal acquisition in steps A2 and A3.

3.2.2 Methods

3.2.2.1 Numeric simulations

Monte Carlo simulations of the nuclear magnetization were performed to determine the sensitivity of the relaxation measurements to noise. The simulations were performed by numerical analysis of the Bloch equations using Matlab software (Mathworks, Natick, MA)[55] with the SD of the noise set at 2% of the signal strength for each sequence. The mean and SD (σ_{T1}) of the solution for T_1 was determined from 100 runs for $0.3 \leq T_1 \leq 1.5$s with T_2=80ms as a function of TR, setting $\alpha=15^o$ and $\beta=60^o$ as in the dual-angle method[52]. The mean and σ_{T2} for T_2 was determined with T_1=1s for $0 \leq T_2 \leq 80$ms. The adiabatic BIR-4 pulse length was set to $\tau_3=2\tau_2$=20ms, with B_1=13.5μT, and f_{max}=5kHz (frequency sweep) to be consistent with the use of a Philips 3T MRI scanner's body coil for excitation during validation experiments.

3.2.2.2 MRI validations on phantoms and human brain

A four-compartment phantom comprised of tubes with T_1 and T_2 values spanning that of brain matter ($640 \leq T_1 \leq 1285$ms and $35 \leq T_2 \leq 191$ms) was prepared for *in vitro* validation studies, using agarose and $CuSO_4$ solutions as described in Chapter 2[56]. Their relaxation values were determined by standard PS and SE methods as detailed below. *In vivo* validation was performed in brain studies of healthy volunteers approved by the Johns Hopkins Institutional Review Board (IRB). Subjects were positioned supine and T_1 and T_2 measured by standard 3D PS and SE methods for comparison with 'Dual-τ Dual-FA' measurements.

All MRI was done on a Philips 3T Achieva MRI scanner (Philips Healthcare, Cleveland OH). The BIR-4 pulse FA was calibrated by ensuring a minimum signal at FA=0° for the pulse-lengths used[73]. The 'Dual-τ Dual-FA' method was validated using a Philips 8-channel SENSE receive-only head coil, with body coil excitation, and BIR-4 pulse parameters as simulated in Sec. 3.2. Under these conditions, the scanner's RF power constraints limited TR to ≥609ms for acquisitions employing 20ms BIR-4 pulses.

Standard 3D PS T_1 and SE T_2 values were measured in every validation experiment to avoid any confounding temporal variations in T_1 and T_2. The same MRI spatial resolution, FOV, and bandwidth (BW) were used for each T_1, T_2, PD, and B_1 mapping method being compared. The PS method employed a slab-selective 3D GRE sequence with TR=100, 300, 600, 900, 1200, 2000ms *in vitro* with FA=90°. The 3D SE method used 32 spin-echoes with TR/TE=1200/10ms. PS T_1 and SE T_2 values were calculated on a pixel-by-pixel basis using a nonlinear least-squares fit of the signal to the relaxation curves $[w.\exp(-TE/T_2)+z]$ and $[u-v.\exp(-TR/T_1)]$, respectively, with u,v,w and z as constants as in Chapter 2. The 3D B_1 distribution determined by the actual flip-angle imaging (AFI) method (TR_1/TR_2=30/130ms, FA=45°), was taken as a standard for FA corrections. Because slice-profile errors are not accounted for in 3D AFI mapping, only the middle slices of slab-selective SE and PS MRI acquisitions were used for validation studies.

Coil receiver sensitivity maps were also computed based on the signal intensities of GRE images acquired from agarose phantoms (TR/TE=2 or 3s/3ms), and corrected for FA, T_1 and T_2. These were fitted to a 2D quadratic polynomial and used to normalize the calculated PD images, for the purpose of generating PD images in percent units (*pu*) relative to water[74]. The standard PD images were corrected for the FA, T_1 and T_2 using the applicable TR/TE values, as applied to the longest TR PS sequence. The 'Dual-τ Dual-FA' PD images were corrected with the 'Dual-τ Dual-FA' FA, T_1 and T_2 values.

Phantom 'Dual-τ Dual-FA' T_1 and T_2 values were compared with PS and SE measurements as percentage differences from the standard values. The means ±SD were determined for each phantom compartment, and for brain regions-of-interest. In phantom 'Dual-τ Dual-FA' MRI experiments, S_1 was acquired with a 15° GRE selective excitation, and S_2 and S_3 were excited by 0º BIR-4 pulses followed by 60º slab-selective 3D GRE sequences, with $\tau_3=2\tau_2=20$ms (TR/TE=609/3.5ms; total scan time=10.1min; elliptical k-space sampling, PE=330 phase encodes; 80x80x14 reconstruction matrix; FOV= 70x130x130mm; BW=117kHz; resolution=5x2x2mm; the central 7th coronal slice was analyzed). The FOV and matrix parameters were modified for human studies (FOV= 200x35x200mm, BW=180kHz; elliptically sampled k-space; PE=619; 224x224x7 reconstruction matrix; resolution=1x5x1mm; total scan time=18.9min, 4th axial slice analyzed).

3.2.3 Results

The Monte Carlo simulations show that T_1 was unaffected by the pre-pulse length τ_2. However, increasing TR above T_1 did introduce a small (systematic) error in the mean T_1 compared to the true value. With the shortest (scanner-limited) TR of 609ms and T_2=80ms, the mean systematic error (±SD) in T_1 was 0.6%±11% for T_1=1 s (Fig. 3.1a). As a percentage, the SD in T_1 decreased monotonically from 30% to 9% as T_1 increased from 0.3s to 1.5s. With TR=609ms, τ_2=10ms and T_1=1s, the mean error for T_2=45ms is 1%±18% (Fig. 3.1d).

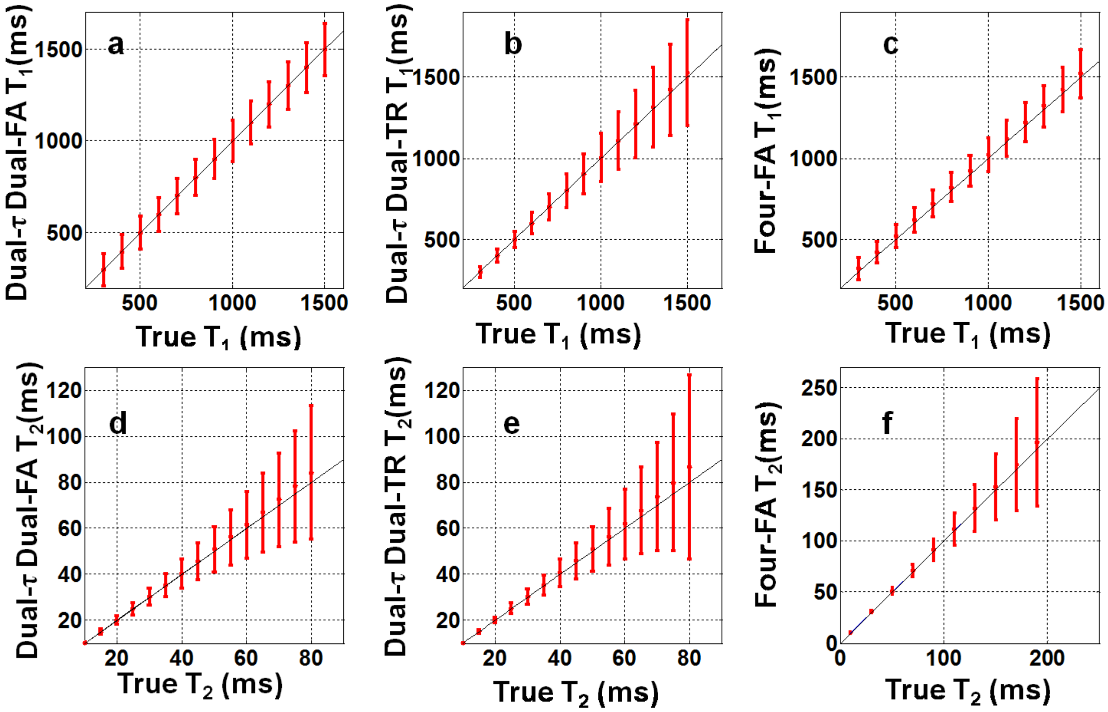

Fig 3.1(a-c) Monte Carlo simulations of the SD in T_1(with T_2=80ms), and (d-f) T_2 (with T_1=1s) with an SNR of 50, and 100 runs. Part (a) and (d) show results for the 'Dual-τ Dual-FA' method with TR=0.609s, $\tau_3=2\tau_2$=20ms, and B_1=13.5uT. Part (b) and (e) show results for the 'Dual-τ Dual-TR' method with $TR_2=2TR_1$=1.06s, $\tau_2=2\tau_1$=20ms, B_1=20uT. Part (c) and (f) are for the 'Four-FA' method with TR=0.6s, TR_4=1.032s, τ=20ms, B_1=20uT over a larger T_2 range.

Experimental 'Dual-τ Dual-FA' T_1, T_2, and PD images of the phantom are shown in Fig. 3.2. The images were segmented into compartments using a region-growth algorithm. Aside from regions with T_2>150ms which are not accurately determined by the 'Dual-τ Dual-FA' method[69], the errors in T_2 were 3.9% ±6.5% vs SE (Fig. 3.2f).

The error in T_1 for the four segmented regions was 11% ±6.5% vs PS (Fig. 3.2e). The PD measured in *pu*[74], has an SD of 9.5% in the phantom (Fig. 3.2a).

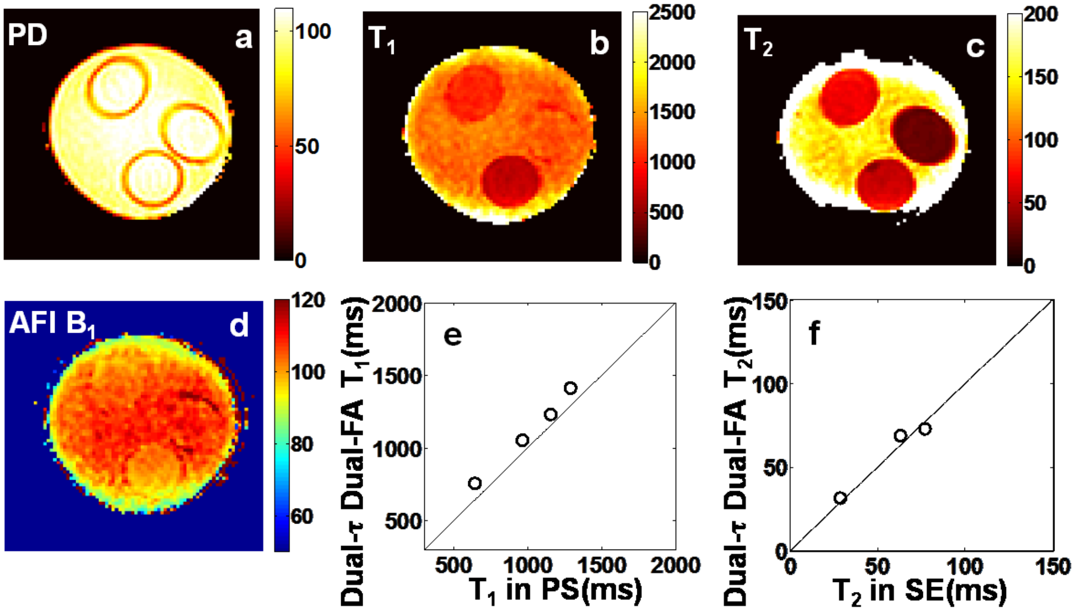

Fig 3.2 Color-coded ‘Dual-τ Dual-FA’ images of (a) PD, (b) T_1, and (c) T_2 in the three-tube bottle gel phantom. Part (d) shows an AFI B_1 map of the phantom. Part (e) plots the ‘Dual-τ Dual-FA’ T_1 vs. the standard PS T_1 for each compartment. Part (f) plots the ‘Dual-τ Dual-FA’ T_2 vs. SE T_2 in the compartments (above 150ms, the ‘Dual-τ Dual-FA’ T_2 is not accurate[69]). The black lines denote identity. The scales of PD is in *pu*, T_1 and T_2 maps are in ms, and the B_1 map is % of the nominal FA.

Fig. 3.3 depicts ‘Dual-τ Dual-FA’ brain MRI results. The ‘Dual-τ Dual-FA’ T_1 values sampled in the annotated regions were 1.65 ±0.12s for grey matter (GM) and 1.06 ±0.08s for white matter (WM). These are consistent with literature values of: 1.33±0.001s[75], 1.47±.05s[76], and 1.82±0.11[77] for GM; and 0.83±0.01s[75], 1.08±0.05s[77], 1.11±0.05s[76], and 1.11s[78] for WM. The ‘Dual-τ Dual-FA’ T_2 values were 68±9ms for GM and 54±5ms for WM, compared to SE results of 73±5ms and 54±5ms, respectively. Published T_2 values for comparison are: 71±10ms[59], 99±7ms[77], and 110±2ms[75] for GM; and 56±4ms[59], 69±3ms[77], 80±0.6ms[75] for WM.

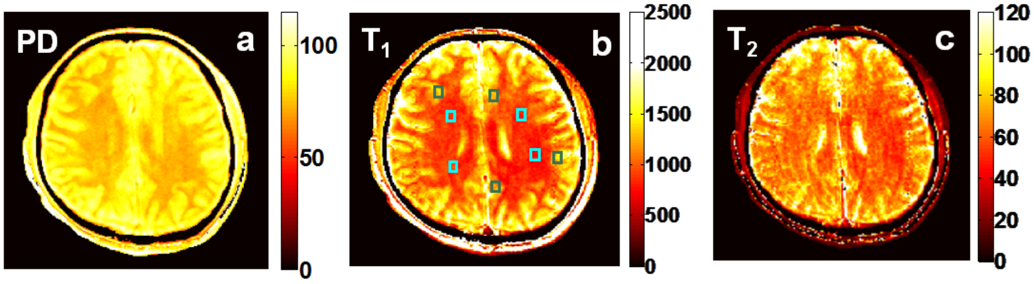

Fig 3.3 Color coded 'Dual-τ Dual-FA' (a) PD, (b) T_1(b) and (c) T_2 images from a healthy human brain. T_1 and T_2 values in the annotated squares in GM (green) and WM (blue) are compared with known values in the text. The scales are in *pu* (PD) and ms (T_1 and T_2).

3.3 Dual-τ Dual-TR Method

3.3.1 Theory

Instead of varying FA to encode T_1 as in the 'Dual-τ Dual-FA' method, the 'Dual-τ Dual-TR' method varies TR along with τ in the following three acquisitions. (B1) A first signal, S_1, is acquired in the steady-state at a short $TR=TR_1$ using a short 0° adiabatic pre-pulse of duration τ_1, followed by a GRE MRI sequence with an FA of φ. (B2) A second signal, S_2, is acquired with a longer $TR_2=2*TR_1$ and the same τ_1 0° adiabatic pre-pulse followed by the φ pulse, GRE sequence. (B3) A third steady-state signal S_3 is acquired also with $TR=TR_2$, but using an adiabatic pre-pulse of duration $\tau_2=2\tau_1$, followed by the same φ pulse, GRE sequence.

The three resulting signals are:

$$S_1 = M_0 \frac{(1-E_1)E_{p1}\sin\phi}{(1-E_1E_{p1}\cos\phi)} \;,\; S_2 = M_0 \frac{(1-E_1{}')E_{p1}\sin\phi}{(1-E_1{}'E_{p1}\cos\phi)} \;,\text{ and }\; S_3 = M_0 \frac{(1-E_1{}')E_{p2}\sin\phi}{(1-E_1{}'E_{p2}\cos\phi)} \;, \tag{3.1}$$

where $E_{p1} = E_p(\tau_1)$ and $E_1' = \exp(-TR_2/T_1)$. Because $\tau_2 = 2\tau_1$, $TR_2 = 2TR_1$, we have $E_{p2} = E_{p1}^2$ and $E_1' = E_1^2$. This equation set can be solved by the numerical iteration of:

$$E_{p1} = \left(\frac{S_3}{S_2}\right)\frac{1-E_1^2E_{p1}^2\cos\phi}{1-E_1^2E_{p1}\cos\phi}\,,\quad E_1 = \left(\frac{S_2}{S_1}\right)\frac{1-E_1^2E_{p1}\cos\phi}{1-E_1E_{p1}\cos\phi} - 1,\ \text{and}\ M_0 = \frac{S_1(1-E_1E_{p1}\cos\phi)}{(1-E_1)E_{p1}\sin\phi}\,, \qquad [3.2]$$

after setting initial values for E_1 and E_{p1}. When $\varphi = 90^\circ$ the solutions are analytic:

$$E_{p1} = S_3/S_2\,,\ E_1 = S_2/S_1 - 1,\ \text{and}\ M_0 = S_1/[(1-E_1)E_{p1}] \qquad [3.3]$$

In all our experiments the FA was set nominally to $\varphi = 90^\circ$. However, the presence of B_1 inhomogeneities generally requires that a FA (or B_1) map must be acquired and the local FAs substituted into the iterative algorithm. Initial values for E_{p1} and E_1 are calculated from Eq. [3.3]. We recorded final values after ten iterations of Eqs. [3.2], but convergence was usually achieved at 4 iterations. T_1 and T_2 values were calculated by substituting E_{p1} for E_{p2} and τ_1 for τ_2, and TR_1 for TR in Eq. [2.7]. The value of TR_1 is selected based on Monte Carlo error analysis of the Bloch equation as described below.

3.3.2 Methods

3.3.2.1 Numeric simulations

Monte Carlo simulations of the 'Dual-τ Dual-TR' method used the same noise, T_1 and T_2 ranges as in Sec. 3.2, but with FA=90° for all three GRE acquisitions. Because validation experiments for this method used the Philips system's birdcage transmit/receive head-coil with a higher B_1, we set $B_1 = 20\mu T$, $f_{max} = 15kHz$, and $\tau_2 = 2\tau_1 = 20ms$ for the BIR-4 pulse. To determine a suitable TR_1, the error in T_1 was calculated from simulations performed with $T_1 = 1s$ and $T_2 = 80ms$ for $0.3 \le TR_1 \le 1.8s$.

3.3.2.2 MRI validations on phantoms

Experiments were performed with the Philips' head-coil and BIR-4 pulse parameters as simulated (Sec. 3.3.2.1). The same 4-compartment phantom used in 'Dual-τ Dual-FA' experiments (Sec. 3.2.2.2) was imaged. S_1 and S_2 were acquired with a τ_1=10ms 0° BIR-4 pre-pulse followed by a nominal-90° slab-selective excitation with TR=530ms and 1060ms, respectively (FOV=70x130x130 mm; resolution=5x2x2mm; BW=117kHz; elliptically sampled k-space, PE=388; 80 x80x7 reconstruction matrix; total scan time=17.1min, central 4th coronal slice analyzed). For step B3, S_3 was acquired with the same nominal-90° selective excitation, but TR was limited to 1060ms by scanner RF power constraints on the τ_2=20ms 0° adiabatic pre-pulse. Measured 'Dual-τ Dual-TR' T_1 and T_2 values were compared to standard SE and PS values acquired with the same experimental parameters used in the 'Dual-τ Dual-FA' experiments. Standard and 'Dual-τ Dual-TR' PD images were computed as in Sec. 3.2.2.2, except that the 'Dual-τ Dual-TR' PD images were corrected using the 'Dual-τ Dual-TR' T_1 and T_2 values.

3.3.3 Results

The Monte Carlo simulations of the 'Dual-τ Dual-TR' method showed that the SD of the estimated T_1 decreased from 27% to 10% as TR_1 increased from 0.3s to 1.2s (Fig. 3.4a), and that the choice of TR_1 had little effect on the T_2 measurement. We chose TR_1=0.53s as a compromise between scan-time, T_1 accuracy, and our scanner's RF power constraints for τ_1=10ms. With these settings, the T_1 error of the 'Dual-τ Dual-TR' experiment varied from 0.6%±11% to 2%±22% for $0.3 \leq T_1 \leq 1.5$s with T_2=80ms. The T_2 error for tissue with (T_1, T_2)=(1s, 45ms) was 1.8±17% (Fig. 3.1b, e).

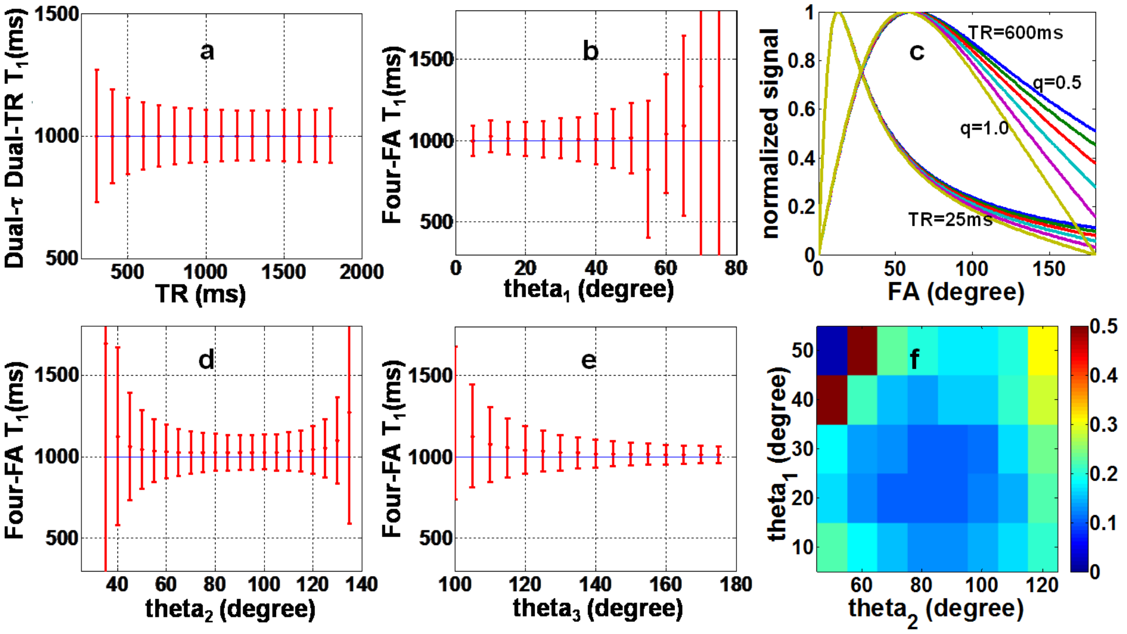

Fig 3.4 Monte Carlo simulations used for selecting TR and FA: (a) the SD in the ‘Dual-τ Dual-TR T_1 experiment as a function of TR; and the SD in the ‘Four-FA’ T_1 experiment as a function of (b) θ_1, (d), θ_2, and (e) θ_3, with each of the other two FAs set to the most favorable values (30°, 80°, 140°, respectively), and SNR=50. The horizontal blue line is the true (input) T_1 value. Part (f) shows the SD in the ‘Four-FA’ T_1 measurement as a function of θ_1 and θ_2, varied independently with a noise level=M_0/100. The scale reflects the SD as a fraction of the true T_1. (c) The normalized steady-state signal as a function of nominal FA for B_1-field variations from 50-100% (*q* =0.5-1.0), TR=25ms and TR=600ms. B_1 field differences can only be differentiated at long TR and high FA.

Experimental ‘Dual-τ Dual-TR’ T_1, T_2 and PD maps of the 4-compartment phantom are depicted in Fig. 3.5, with the relaxation values plotted below. The mean errors are 6.6±11% for T_1 in the range $0.65 \leq T_1 \leq 1.3$s; and 2.7%±5.2% for T_2 in the range 29ms$\leq T_2 \leq$187ms. The SD of the PD signal is 8.8%.

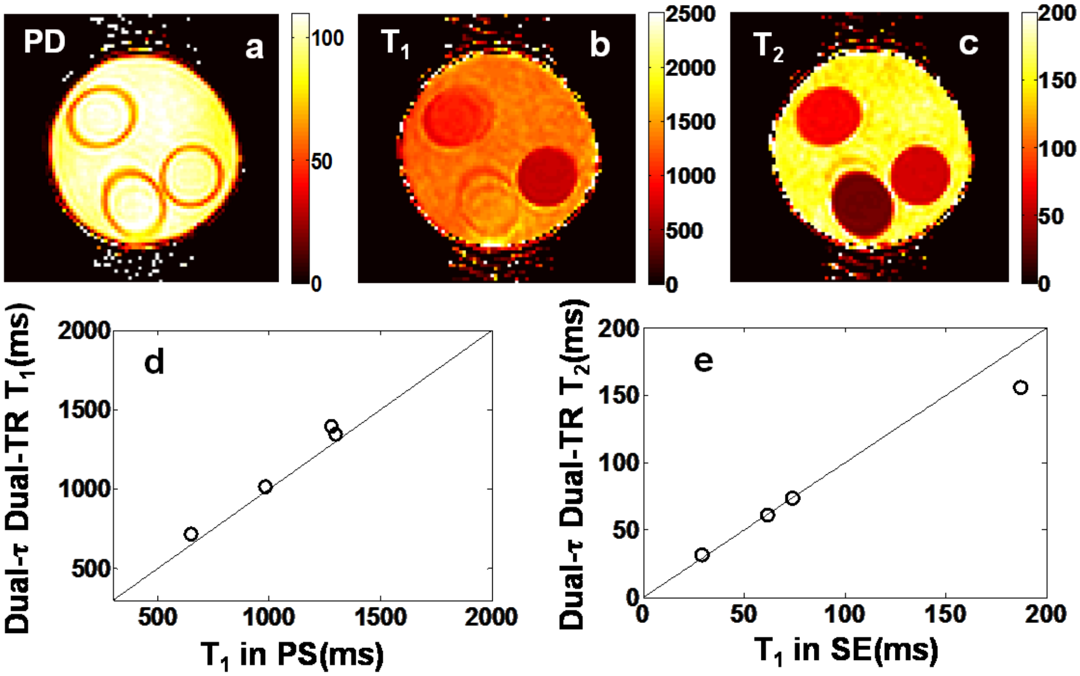

Fig 3.5 In vitro color-coded 'Dual-τ Dual-TR' (a) PD, (b) T_1 and (c) T_2 from the same phantom as Fig.3.2. Parts (d) and (e) plots the mean T_1 and T_2 values for the four compartments compared to measured standard PS and SE values (the black line is the identity line).

3.4 Four-FA Method

3.4.1 Theory

The accuracy of all of the above methods, including the standards, depends on accurate knowledge of the FA. Fast FA mapping techniques such as AFI or as provided by the MRI scanner manufacturer, require at least two acquisitions and are generally limited in accuracy to the central uniform region of selectively excited slices or slabs[79]. Thus, when FAs are uncertain and an FA map is required, even the minimum-acquisition 'Dual-τ Dual-FA' and 'Dual-τ Dual-TR' methods actually require at least five acquisitions to produce accurate T_1, T_2 and PD maps. This is greater than the minimum possible number of acquisitions–four, that could be used to measure the independent parameters T_1, T_2, PD, and FA. The 'Four-FA' method achieves this by incorporating an FA (or B_1) determination in the same protocol.

The 'Four-FA' method acquires three steady-state signals S_1, S_2 and S_3 from spoiled GRE MRI sequences each applied with the same $TR=TR_1$, but different nominal FAs, θ_1, θ_2, and θ_3 in steps C1-C3. A fourth signal, S_4, is acquired in step C4, using a long 0° adiabatic pre-pulse of duration τ_2 followed by a GRE sequence with $FA=\theta_4$, and $TR=TR_2$. In these studies, we set the actual FAs equal to the nominal FAs scaled by a factor q that reflects the effect of a nonuniform B_1-field at each (pixel) location. The four steady-state signals are thus:

$$S_1 = M_0 \frac{(1-E_1)\sin(q\cdot\theta_1)}{1-E_1\cos(q\cdot\theta_1)}\ ,\ S_2 = M_0 \frac{(1-E_1)\sin(q\cdot\theta_2)}{1-E_1\cos(q\cdot\theta_2)}\ ,\ S_3 = M_0 \frac{(1-E_1)\sin(q\cdot\theta_3)}{1-E_1\cos(q\cdot\theta_3)} \text{ and}$$

$$S_4 = M_0 \frac{(1-E_1')\sin(q\cdot\theta_4)E_{p2}}{1-E_1'\cos(q\cdot\theta_4)E_{p2}}\ . \tag{3.4}$$

Here, the B_1 scaling factor, q, proton density M_0, and T_1 attenuation factor E_1 are solved by three-coefficient least-squares fitting of the signal curve with $x=[\theta_1, \theta_2, \theta_3]$, $y=[S_1, S_2, S_3]$, $coeff=[M_0, E_1, q]$, minimizing $\|F(x,coeff)-y\|_2^2$. T_1 is obtained from E_1. Then M_0, q, and E_1' are substituted into the expression for S_4 to obtain E_{p2}, from which T_2 is obtained using Eq. [2.7]. Note that the value of T_2 is determined by S_4, after computing the other parameters from S_1, S_2, or S_3 in Eq. [3.4]. Also, by choosing $\theta_4=\theta_1$, the θ_1 and M_0 terms in S_4 and S_1 cancel in Eq. [3.4], enabling a direct computation of T_2 from the ratio S_4/S_1, once T_1 is known.

As noted earlier, short 0° adiabatic pre-pulses added to the three sequences in steps C1-C3 can control for the effects of the delay following the adiabatic pre-pulse used in step C4. The T_2 attenuation from a 1ms pre-pulse, for example, is negligible (<3% for

T_2>13ms and <0.7% for brain tissue), and does not significantly affect the solution of Eq. (10) as presented. The values of θ_1, θ_2, and θ_3 are chosen as those that minimize T_1 quantification errors based on Monte Carlo simulations of the Bloch equations over an appropriate range of relaxation times. This results in at least one FA>90°.

3.4.2 Slice profile correction

The 'Four-FA' method can correct for an inhomogeneous B_1 field, as long as the slice profiles excited by θ_1, θ_2 and θ_3 have the same shape with magnitudes proportional to $\sin(q.\theta)$. However, this does not hold for FA>90°[80] where signals from the edge of the profile can greatly exceed $\sin(q.\theta)$ at the slice center (Fig. 3.6)[81]. For full or slab-selective 3D MRI[82], the middle slice of an excited slab is typically unperturbed by the slice profile, and yields accurate results even with short, truncated slab-selective excitation pulses. However, for 2D MRI employing a single slice selection with FA>90° pulses, the integrated effect of slice profile imperfections can be substantial. In this case, the T_1 error can be calibrated by a factor generated by Bloch equation simulations and/or determined experimentally, as detailed below.

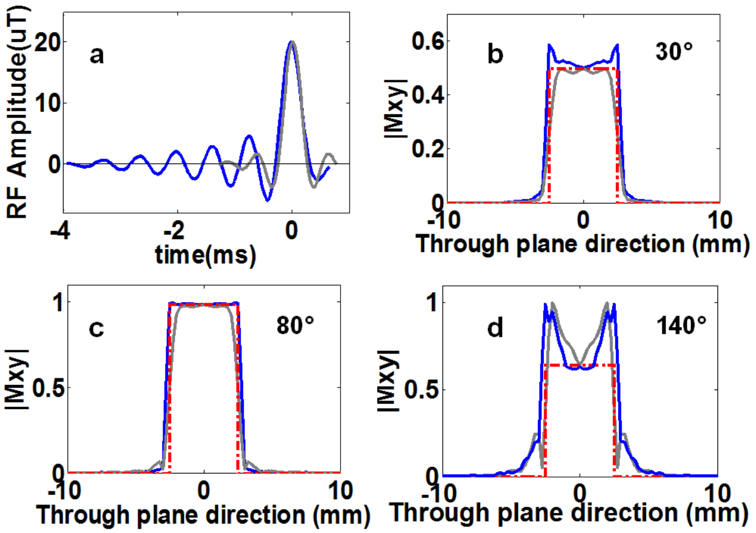

Fig 3.6(a) Waveforms of ‘spredrex’ (blue) and truncated ‘sinc’(grey) FA=80° pulses used in our ‘Four-FA’ MRI sequences. The ‘spredrex’ pulse is more than twice as long as the truncated sinc pulse. Parts (b-d) show the slice profiles for the spredrex and sinc pulses determined from the magnitude of the transverse magnetization for (b) 30°, (c) 80°, and (d) 140° pulses used in the ‘Four-FA’ studies. The dashed red line is an ideal 5mm slice pulse profile.

3.4.3 Numerical simulations

Monte Carlo simulations of the ‘Four-FA’ method used the same T_1 range as the earlier simulations, but a larger T_2 range of $0 \leq T_2 \leq 190$ms, and a noise level of $M_0/100$ or an SNR of 50. The same BIR-4 pulse as the ‘Dual-τ Dual-TR’ was used with $\tau =$ 20ms[69]. FAs were successively incremented by 5° from 5°-180° to determine the values of θ_1, θ_2 and θ_3 that minimized the error in T_1. The rationale for setting the FAs is as follows. Fig. 3.4c shows that in order to differentiate B_1, the signal curves should be sampled at FAs that span the range 0-180°, and that maximum differentiation occurring at the highest FA. If we allow a 25% variation in B_1, the nominal FA cannot be greater than 140° lest the actual FA exceed 180°, which would cause aliasing. This sets the maximum FA for optimally differentiating B_1 inhomogeneity at ~140°. The other two

FAs are basically chosen to minimize the error in T_1, based on the Monte Carlo simulations.

The effect of an imperfect slice profile is to alter the ($q.\theta$) terms in Eq. [3.4] as a function of position across the slice (Fig. 3.6). This is not accounted by the global solution of Eq. [3.4]. In addition to a standard 'sinc' pulse excitation, the Philips' scanner can provide 'spredrex' excitation pulses (Fig.3.6a), which have an improved slice profile at high FA across the center of the slice, as compared to a truncated 'sinc' pulse (Fig.3.6d) [81]. A Bloch equation simulation of the effect of slice profile imperfections on T_1 was performed by digitizing 'spredrex' pulses into 996 rectangular segments, with the pulse length, amplitude, and gradient strength set according to the scanner's pulse viewer tool and T_2=50ms and 100ms. The simulated 'Four-FA' T_1 was compared with the true (input) T_1, and a linear correction curve computed. To account for possible system non-linearity in the scanner's delivery of the RF waveform to the coil, the response assuming a small quadratic term included in the output response, was also computed.

3.4.4 Experimental validation

The 'Four-FA' method was validated with a phantom comprised of 11 isolated gel-filled tubes spanning a broader range of T_1 and T_2 than used for the earlier methods ($186 \leq T_1 \leq 1332$ms, $13.2 \leq T_2 \leq 227$ms), and in IRB-approved studies of the human brain. A 1ms 0° adiabatic pre-pulse was added 9ms prior to slice-selective excitation in steps C1-C3, while step C4 used a 20ms BIR-4 pulse applied with the same pre-pulse delay. In phantom studies, S_1-S_4 were acquired using standard 2D and (slab-selective) 3D GRE MRI (TR_1=600; TR_2=1036ms; TE=1.9-3.0ms. 3D: FOV=25x160x160mm; resolution 5x2x2mm; BW=144kHz; elliptically sampled k-space; PE=353; reconstruction matrix

80x80x5; total scan time=16.7min, 3rd coronal slice analyzed. 2D: FOV=200x5x200mm; resolution=1x5x1mm; BW=180kHz; PE=200; reconstruction matrix 224x224; total scan time=9.6min) with nominal FAs of θ_1=30°, θ_2=80°, θ_3=140°, and θ_4=30°.

Human brain studies utilized the same sequences, except that the 3D array had same-sized sections as 2D (3D FOV=200x 25x200mm; elliptically sampled k-space; PE=550; reconstruction matrix 224x224x5; resolution 1x5x1mm; BW=180kHz; total 3D scan time=26min, 3rd axial slice analyzed).

The *in vitro* 'Four-FA' relaxation measurements were compared to 3D SE T_2 data acquired with 14 echoes (TR/TE=500/15ms), and PS T_1 measurements acquired the same as in Sec. 3.2.2.2. The *in vivo* 'Four-FA' measurements were compared with PS T_1 data acquired using a slab-selective 3D GRE sequence at TR=100, 600, 1200ms and FA=90°; and with standard 32-echo 3D SE T_2 data acquired at TR=725ms. Standard and 'Four-FA' PD images were computed as in Sec. 3.2.2.2, except that the 'Four-FA' PD images were corrected using the 'Four-FA' T_1, T_2 and FA values.

The effect of non-uniform slice profiles on the observed T_1 for the 2D (slice-selective) 'Four-FA' method with the 'spredrex' pulse was measured in the 11-tube phantom, and the results compared to the numerical simulations with and without a small quadratic RF system response. The experimental results relating 2D 'Four-FA' T_1 to 3D PS T_1 were fitted to a linear regression line and used to correct 2D T_1 values for slice profile effects. The T_2 images were then recalculated using the corrected T_1 values on a pixel-by-pixel basis.

3.4.5 Results

3.4.5.1 Numerical simulations

Bloch equation simulations of the ‘Four-FA’ method in Fig. 3.4c show that increasing TR increases the dispersion in steady-state signals elicited by different FAs, and improves the accuracy of T_1 and B_1 measurements. The Monte Carlo simulations show that the error in T_1 decreases monotonically with increasing θ_3 up to 180° (Fig. 3.4e). Setting $\theta_3 = 140°$ to accommodate a ~25% B_1 variation, the error in T_1 increases monotonically with θ_1, and has a minimum for $\theta_2 \sim 80°$. A plot of the SD in T_1 wherein θ_1 and θ_2 are varied independently, confirmed that noise is minimal with a θ_1 of 20°-30° and a θ_2 of 70°-100° (Fig. 3.4f). Accordingly, we chose $\theta_1 = 30°$and $\theta_2 = 80°$.

Monte Carlo simulations performed with $\theta_4 = \theta_1$ (to cancel the θ_1 and M_0 terms in Eq. [3.4] show that the uncertainty or SD in T_2 is <3% for $20° \leq \theta_4 \leq 40°$, and does not vary by more than 2% for choices of TR_2 in the range $0.3 \leq TR_2 \leq 1$s. Therefore, we chose the shortest TR allowed by the scanner for step C4: TR_2 =1.032s. With TR_1=0.6s, and T_2=80ms, the simulations show that the uncertainty in T_1 measured by the ‘Four-FA’ experiment decreases from 4±19% to 1.6±7.5% as T_1 increases from 0.3 to 1.5s (Fig. 3.1c). With T_1=1s, TR_2=1.032s, τ=20ms, the error in T_2 is ≤ 0.4±27%, increasing with T_2 ≤190ms (Fig. 3.1f).

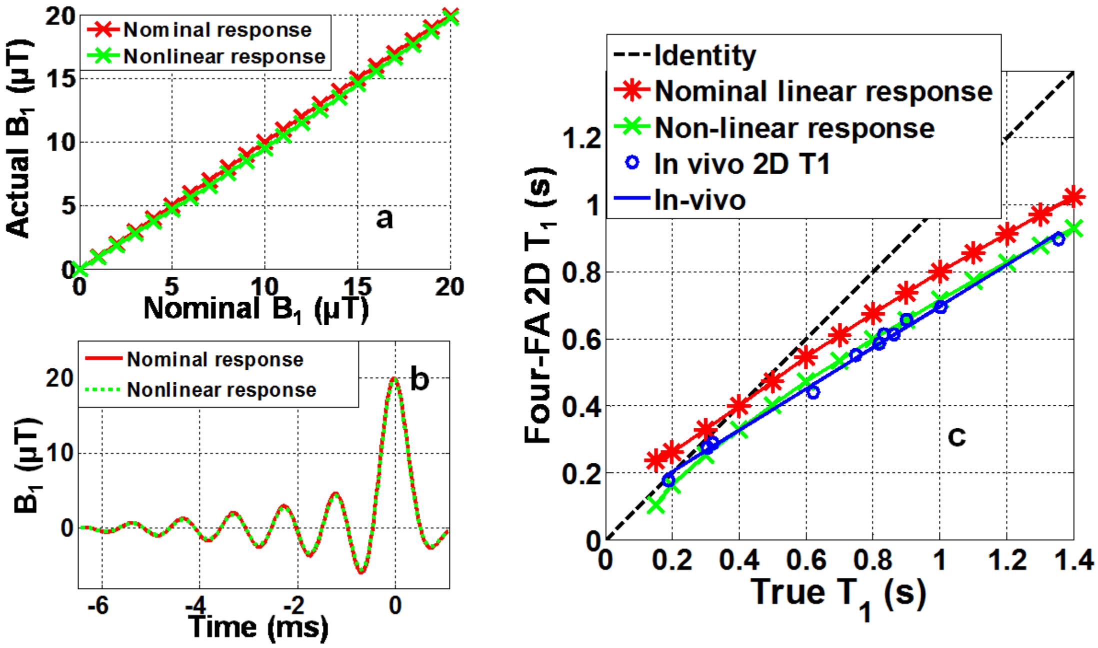

Fig 3.7 Effect of slice profile on T_1. (a) Actual B_1, or B_{1A}, for a linear system response (red stars), and with (green crosses) a small second-order ($B_{1A}=0.004B_{1I}^2+0.91B_{1I}$) RF system response, as a function of input B_1, denoted B_{1I}. (b) Effect of the linear and second-order responses on the 'Spredrex' excitation waveform for a maximum B_1=20μT (FA=140°). (c) Bloch equation simulation of the 'Four-FA' T_1 acquired with the 2D 'Spredrex' excitation pulse from (b), compared to the true T_1 assuming linear (red stars) and non-linear (green crosses) RF system responses. Blue circles show the experimental results from the 11-tube phantom fitted to a straight line (R^2=0.995; T_1^{2D} = $0.62T_1^{3D}$ + 81.3; blue line) that were used for calibration. Here, the 3D PS T_1, denoted T_1^{3D}, measurements are plotted as the 'True T_1'.

Results from the slice profile simulations comparing the apparent T_1 with the true T_1 for the 'spredrex' excitation used in the slice-selective (2D) 'Four-FA' experiment are plotted in Fig. 3.7. The star symbols (red) assume a linear RF field response. The crosses (green) show the effect of assuming a mild quadratic nonlinearity in the delivered RF field (Fig. 3.7a), which barely attenuates the pulses' side-lobes (Fig. 3.7b). The integrated effect of the slice profile excitation was to reduce the observed T_1 compared to the true

T_1: by about 20% and 28% at T_1=1s, for the linear and non-linear profiles, respectively (Fig. 3.7c). These results did not change appreciably with T_2.

3.4.5.2. Experiments

Fig. 3.8 compares 3D slab-selective 'Four-FA' T_1, T_2 and B_1 maps with the standard images acquired from the 11-tube phantom. Mean 'Four-FA' values are plotted against standard values in the first column. Mean differences are all within 5%: the error in T_1 is 2.5%±14% and the error in FA or B_1 is 0.9%±8%. Even though the tube in the bottom left of Fig.3.8c has an anomalously poor B_0 at its rim which compromises the performance of the adiabatic pulse used for the T_2 determination, the error in T_2 is just 3.6%±9%. The SD of the sensitivity- and T_2-corrected PD image of the phantom was ±5.3% (not shown).

Fig. 3.9 shows 3D 'Four-FA' results from two volunteers. T_1 and T_2 values in the blue boxes in the WM region and the green boxes in the GM region are compared with standard T_1 and T_2 values from the same region. The mean ±SD error in T_1 is -4.0±8.5% and -5.5±6.0% for volunteers A and B respectively. The T_2 errors are 0.9±7.4% and 1.2±10.1%, respectively. For WM, the mean relaxation values are (T_1, T_2)=(859, 64.9) for volunteer A, and (865, 64.7) for volunteer B in ms. For GM, (T_1, T_2)=(1387, 75.4) and (1351, 77.0) in ms. These are consistent with prior published values listed in Sec. 3.2.3. On the other hand, contrast between cerebral spinal fluid (CSF) and neural tissue is poor in the standard PS T_1 and SE T_2 maps where the TRs (of 1.2s and 0.6s) are much less than T_1 and T_2 of CSF (in the range of 4/2s)[68]. Indeed, all of the T_1 and T_2 measurements of CSF appear lower than literature values, although the 'Four-FA' images provide much higher contrast between CSF and WM.

A comparison of the 2D slice-selective ‘Four-FA’ T_1 measurements with the standard 3D PS T_1 measurements taken as the ‘True T_1’, is included in Fig. 3.7(c). The empirical data (blue points and line; R^2=0.995) are consistent with the simulation (green) that assumes a small (0.004 B_1^2) quadratic RF response. Fig.3.10 compares 2D ‘Four-FA’ brain T_1 and T_2 maps computed without and with the empirical slice profile correction, with corresponding 3D PS T_1 and 3D SE T_2 results which are not subject to slice profile effects. As expected, the correction primarily affects T_1, reducing the 2D ‘Four-FA’ errors in the boxes that were annotated in Fig. 3.9 from -33±5% to -3.6±6% for T_1, and from -9.7±3.8% to -8.5±3.6% for T_2.

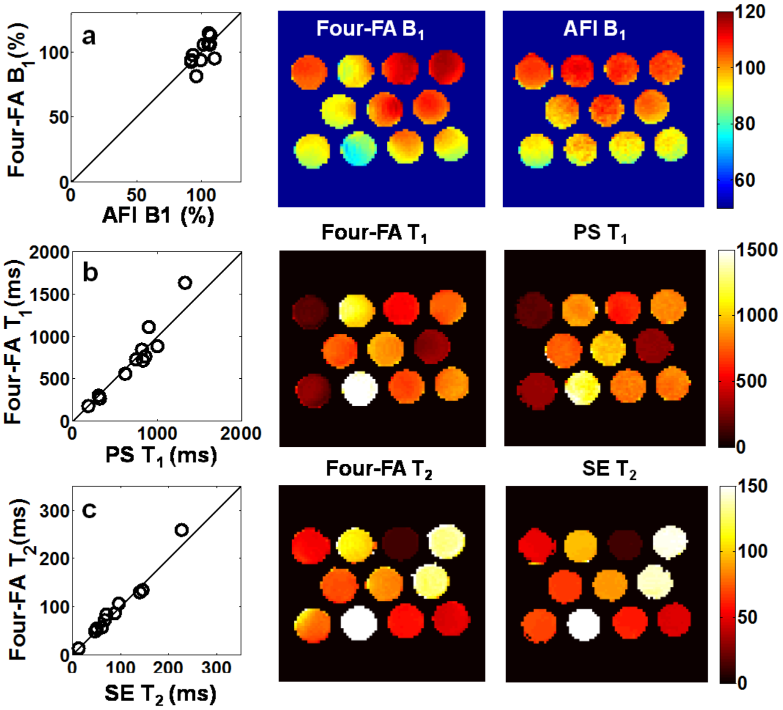

Fig 3.8 ‘Four-FA’ results vs. reference values (column 1), and corresponding ‘Four-FA’ (column 2) and reference images (column 3) from the 11-tube phantom. Color scales are the same for each row (row a, B_1 distribution, % nominal FA; row b, T_1, ms; row c, T_2 in ms).

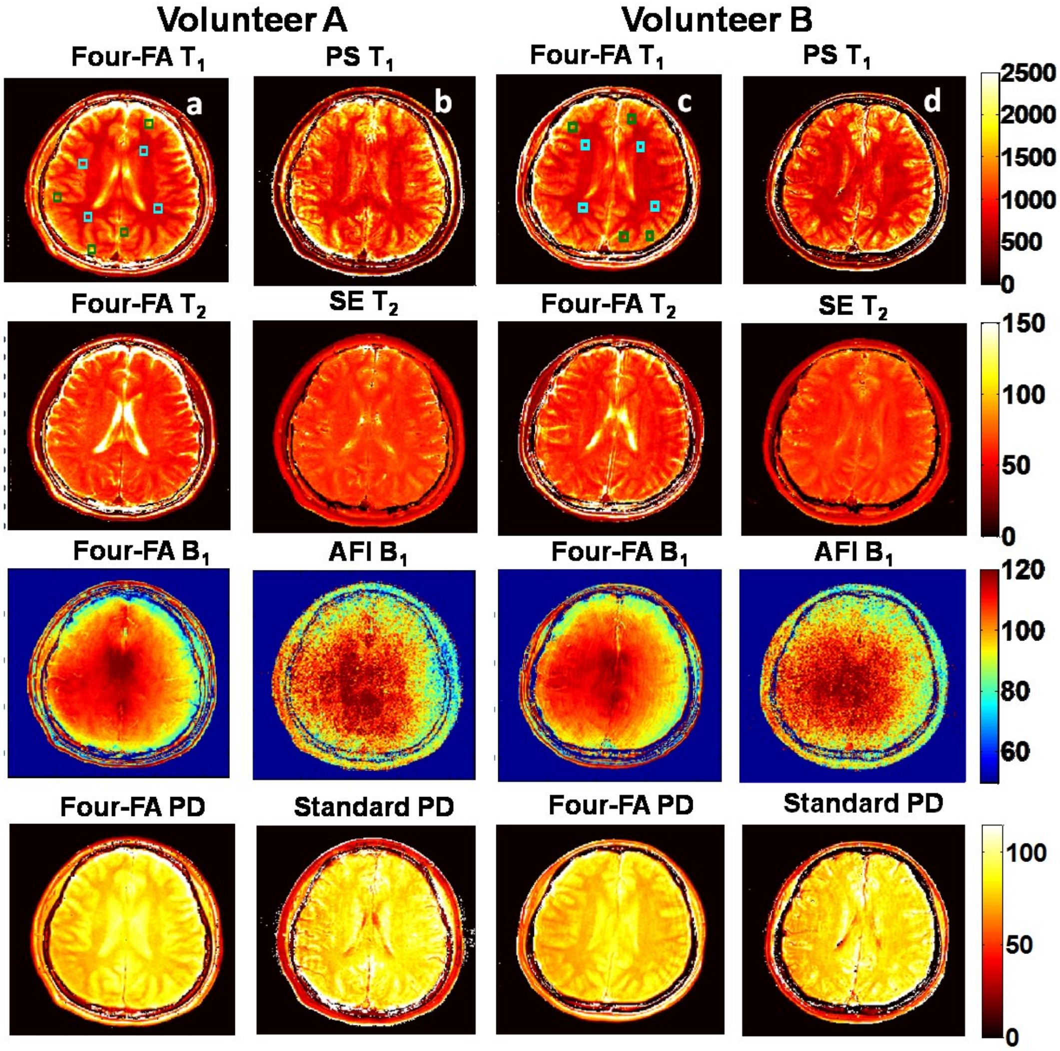

Fig 3.9 In vivo 3D ‘Four-FA’ images for two healthy volunteers (A, column a; B, column c) compared with corresponding standard maps from the same subjects (columns b and d, respectively). The maps are depicted with the same scales at right. The T_1 and T_2 scales are in ms, the B_1 scale is in % and PD is in *pu*. ‘Four-FA’ relaxation values in the annotated boxes are compared with PS T_1 and SE T_2 values in the text. The poorer SNR and CSF contrast in the standard T_1 and T_2 maps is attributable to the TR settings used for these studies.

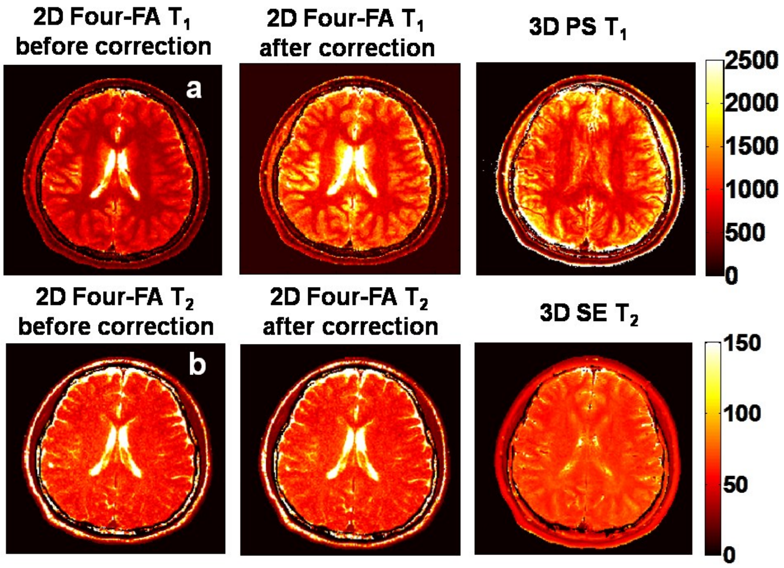

Fig 3.10 Fig. 2D 'Four-FA' T_1 (Row a) and T_2 (Row b) before and after application of slice profile corrections, as compared to standard PS and SE measurements from the central slice of 3D data sets, which do not have the slice profile problem. GM and WM show good agreement with the standards. The data are from Volunteer A in Fig. 3.9, and the scales are in ms.

3.5. Efficiency and accuracy

3.5.1 Theory

The theoretical efficiency of a T_1 method, Γ_{T1}, has been defined as T_1 divided by the SD in T_1, per square-root of the scan time, σ_{T1}, for a unit random noise with SD=σ_0 in the underlying signal[60, 83, 84]. By extension, the efficiencies in determining the mean values of T_1, T_2, B_1 and PD (or M_0) are:

$$\Gamma_{T1} = \frac{T_1}{\sigma_{T1}\sqrt{T_S}}, \Gamma_{T2} = \frac{T_2}{\sigma_{T2}\sqrt{T_S}}, \Gamma_{B1} = \frac{B_1}{\sigma_{B1}\sqrt{T_S}} \text{ and } \Gamma_{M0} = \frac{M_0}{\sigma_{M0}\sqrt{T_S}} \qquad [3.5]$$

where the σ's are SDs in the respective measurements, and T_s is the total scan time for acquiring T_1, T_2, B_1 and M_0 in the combined experiment. Note that while the Γ's reflect the scatter in the measured parameters, they do not show the accuracy of the determinations. We therefore compute the fractional accuracy or systematic error, defined as the difference between the mean determination from the simulations and the 'true' input values, divided by the true value. Because accuracy is arguably as important as efficiency, we divide Γ by the accuracy, Γ/(mean error), to create a figure-of-merit reflecting the efficiency per unit accuracy.

3.5.2 Methods

The efficiency and accuracy of the 'Four-FA' method were determined by Monte Carlo simulations for true values of (T_1, T_2) = (860, 65ms) and (1360, 75ms) to approximate WM and GM relaxation, respectively, as measured in PS, SE and 'Four-FA' experiments. Simulations were also performed with (T_1, T_2) = (1000, 70ms), which falls in the middle of this range. 10^4 runs were performed with four levels of noise (σ_0=M_0/50, M_0/100, M_0/150 and M_0/200) added to the theoretical signal strengths. For comparison, the efficiency and accuracy were also simulated for the following common and efficient T_1, T_2, and PD imaging methods: (i) standard PS (TR=0.1, 0.6, and 1.2s) combined with a multi-SE sequence (TR=0.5s; 14 echoes); (ii) DESPOT1/2[60] (TR=3.4ms, NEX=5; DESPOT1 FA=3°, 12°; DESPOT2 FA=20°, 80°); (iii) and IR TrueFISP[61] (with TR=6.46ms, NEX=5, FA=45°, 5s delay ever 21 PE steps, 38 images acquired). The efficiencies were calculated from Eqs. [3.5] with the duration of a standard AFI sequence (FA=45°, TR1/2=30/130ms) added to all methods lacking a B_1-mapping feature, in order to provide an equivalent comparison to the 'Four-FA' method. Efficiencies were also computed without the AFI sequence for reference. The T_1 and T_2 efficiency of the MRF method without AFI were determined from results presented in Ref. [68] that show it to have ~2.1 and ~1.6 times the T_1 and T_2 efficiencies as DESPOT1 and DEPOT2, respectively, at T_1/T_2 values of 985/67ms. The efficiency of MRF with AFI, assumed a 200x200 AFI image matrix[68].

3.5.3 Results

With $\sigma_0=M_0/100$ and input $(T_1, T_2)=(1000, 70\text{ms})$, the Monte Carlo simulation of the 'Four-FA' method yielded a mean T_1 of 1007±114(SD) ms, that is, a mean error of 7ms or 0.7%. The scan time for one phase-encoded acquisition was $3TR_1+TR_2=0.6\text{x}3+1.036=2.836$ s. Thus, the T_1 efficiency of the Four-FA method was $1000/(114\sqrt{2.836})=5.2$, and its efficiency/error was 5.2/0.7=7.4. The efficiency and mean error for all the methods being compared are listed in Table 3.2. Except for the MRF method for which information is presently incomplete, DESPOT1/2 is the most efficient for T_1 T_2 mapping when no B_1 mapping is included, as was previously reported[60]. However, adding AFI to provide B_1-calibration reduces the T_1 and T_2 efficiency of DESPOT1/2 as compared to 'Four-FA', while DESPOT1/2 was 6-times less accurate. The 'Four-FA' method was at least twice as efficient as AFI in B_1 mapping, and more than 50 times more accurate. The 'Four-FA' method outperformed in efficiency per unit accuracy for jointly measuring T_1, T_2, B_1 (or FA), and PD, with the exception that PD measured with IR True-FISP had zero mean error. The efficiency and mean errors varied with T_1, T_2 and σ_0, and typically improved with decreasing noise, $\sigma_0<M_0/100$. Analysis of the 'Dual-τ Dual-TR' and 'Dual-τ Dual-FA' methods showed they were less efficient than the 'Four-FA' method.

3.6 Discussion

This paper extends the application of the T_2 filtering property of 0° adiabatic pre-pulses to combined T_1, T_2 and PD imaging methods, by introducing three new imaging protocols that employ the minimum number of steady-state acquisitions possible. While

Table 3.2 T_1, T_2, B_1 and M_0 efficiency, mean error (%), and [efficiency/mean error] for 'Four-FA' and relative quantitative mapping methods at T_1=1s, T_2=70ms and noise level =M_0/100. Numbers in the brackets indicates the efficiency without the B_1 mapping sequence (AFI).

	Four FA	Standard with(w/o) AFI	DESPOT1/2 with(w/o) AFI	IR TrueFISP with(w/o) AFI	MRF* with(w/o) AFI
T_1 efficiency	5.2	3.6 (3.7)	4.5 (8.2) [a]	2.0 (2.1)	8.4 (16)
mean error(%)	0.7	2.3	9.3	17	-
efficiency/error	7.4	1.6 (1.6)	0.5 (0.9)	0.1 (0.1)	
T_2 efficiency	4.7	7.2 (7.4)	4.3 (7.9) [a]	2.7 (2.8)	6.3 (12)
mean error(%)	1.4	4.5	9.5 [b]	8.7	-
efficiency/error	3.4	1.6 (1.6)	0.5 (0.8)	0.3 (0.3)	
B_1 efficiency	23	2.8	9	2.8	9.5
mean error(%)	0.06	3.2	3.2	3.2	3.2
efficiency/error	383	0.9	2.8	0.9	3
M_0 efficiency	11.8	8.0 (8.3)	9 (17)	53(55)	-
mean error(%)	0.2	0.2 [c]	3.6	0.03	-
efficiency/error	59	40 (42) [c]	2.5 (4.7)	1800 (1800)	

Notes: The relative standings of the methods vary with T_1 & T_2 as follows. [a]DESPOT1/2 has (<10%) higher efficiency than 'Four-FA' at (T_1, T_2)= (860ms, 65ms). [b]The error in DESPOT1/2<TrueFISP error at (T_1, T_2)=(860ms, 65ms). [c]The error and efficiency/error in the standard method are respectively lower and higher than 'Four-FA' at (T_1, T_2)=(1360ms, 75ms).

*Efficiency was estimated from Fig. 5 of [85] at T_1=985ms and T_2=67ms (% error estimates from the figure, and M_0 efficiency data were unavailable).

the ‘Dual-τ Dual-TR’ and ‘Four-FA’ methods were not previously described, we note that the ‘Dual-τ Dual-FA’ method, was previously introduced as the ‘Tri-τ’ method for T_1 and T_2 measurements, but not for MRI[69] (name corrected to ‘Dual-τ Dual-FA’ in Chapter 2). In fact, inaccuracies in both T_1 and T_2 due to what turned out to be B_0, B_1 and slice profile effects when attempting MRI with the ‘Tri-τ’ method are what inspired the present work.

For a combined T_1 and T_2 MRI experiment, the use of 0° adiabatic pre-pulses have advantages over spin-echoes in avoiding the confounding effects of saturation that arise when the excitation pulses are non-90° or non-uniform[72, 86]. T_2 accuracy is enhanced by including a short 0° adiabatic pre-pulse in at least one sequence, as a control. While SSFP sequences also generate stimulated echoes and provide sensitivity to all three of T_2, T_1 and M_0[87], the peak of the true T_2 echo signal actually falls at the center of the next excitation pulse[88]. Moving the echo to the center of the acquisition window by means of MRI gradients–as is invariably done in MRI–renders the signal prone to the effects of T_2*, motion during the MRI gradients, as well as the usual B_1 inhomogeneity and off-resonance effects.

Indeed, all existing T_1 methods are prone to errors in B_1 when deployed with sequence TRs $\leq T_1$ and large FAs. We chose incoherent steady-state sequences for T_1 encoding, because unlike transient methods (Table 3.1) they are amenable to the repeat acquisitions required for spatial encoding, which can allow greater versatility in adjusting the number of averages or spatial encoding steps than approaches that sample the transient recovery of the magnetization. The primary determinant of accuracy was B_1 inhomogeneity which is intrinsically worse at 3T compared to lower fields, owing to RF penetration effects. When incorporated into 3D or slab-selective sequences with FA corrections provided by our scanner's B_1 mapping sequence, all of the new methods agreed experimentally with the standard 3D SE and PS methods within 11%. However, in 2D slice-selective sequences, even though the 'Four-FA' method yielded results comparable to standard 2D slice-selective SE and PS measurements, the T_1 measurements–including those acquired with standard 2D PS–all differed significantly from the 3D measures. This is attributable to the inadequacy of the scanner's AFI method for addressing slice profile effects[79]. Even so, adding a 2D AFI correction to the 2D measurements did not fully correct for the T_1 differences between any of the 2D images and the 3D PS results acquired for reference. This means that the FA measured by the scanner's standard AFI protocol was insufficient to permit accurate correction of T_1 measured by 2D MRI.

Since FA is so critical to accuracy, and B_1-inhomogeneity is more problematic at ≥3T fields, it makes most sense to formally integrate the FA or B_1 correction, into the whole T_1, T_2 and PD imaging method, as exemplified by the 'Four-FA' method. This also ensures that the correct FA information specific to the actual T_1 or T_2 sequence(s) is acquired, which is typically not the case when standard AFI sequences are run. Combining the FA meaurement with the addition of only one acquisition via the 'Four-FA' method, improves the overall efficiency as compared to adding the at-least-two acquisitions required for AFI, to an existing method.

In fact, when B_1 corrections derived from the scanner's AFI protocol were used, both *in vivo* and *in vitro* studies yielded 'Dual-τ Dual-FA' T_1 maps that were systematically slightly higher than the PS T_1 maps (Fig. 3.5). Because results from a conventional (non-MRI) 'Dual-τ Dual-FA' T_1 NMR experiment previously demonstrated essential agreement with standard methods [69], we attributed the difference to the inadequacy of the scanner's AFI B_1 mapping protocol in replicating the FA distribution that was in effect during the 'Dual-τ Dual-FA' experiment. This was confirmed by phantom 2D 'Four-FA' validation experiments which revealed AFI B_1 values that were ~12% lower than the 'Four-FA' B_1, and by numerical simulations of the effects of such B_1 errors on T_1. Indeed, when the effective B_1 was measured using fully-relaxed experiments in which the FA was varied and the NMR signal fit to a sine curve, the 'Four-FA' B_1 was observed to agree with the measured B_1 to within 0.4%. Clearly, greater accuracy in B_1 mapping would at least improve the accuracy of 'Dual-τ Dual-FA' measurements, and likely T_1 measured by other methods as well. In this regard, note that the SNR of 'Four-FA' B_1 is more than twice that of the scanner's AFI B_1 map (Fig. 3.9).

Because the 'Dual-τ Dual-TR' method uses the same FA ~90°, it is relatively insensitive to B_1 mapping errors. The *in vitro* validation indicated accurate T_1 and T_2 mapping over a wide range of T_1 and T_2. However the scanner's built-in RF power constraints limited the shortest TR to $\geq$530ms for the Philips transmit/receive head coil, whereupon doubling the TR in steps B2 and B3 resulted in a total acquisition time that was comparable to a conventional T_1 measurement. Consequently, we did not validate the 'Dual-τ Dual-TR' method *in vivo*. The RF power associated with long adiabatic pulses is a significant limitation on long-τ acquisitions due to regulatory compliance[50]. It does not help that scanner power limits can over-state the deposited power by 2.2-fold or so[89].

The ‘Four-FA’ method self-corrects for FA inhomogeneity. While it has been suggested that varying FA to estimate B_1, M_0 and T_1 is an ill-posed problem[90], we have demonstrated that the three parameters can be fairly accurately estimated from a least possible number of acquisitions (Fig. 3.4c). Generally, TR should be chosen generally in a range ~$T_1/2$, but the simulations and experiments show that a fixed TR of 600ms yields accurate results for $TR/3 \leq T_1 \leq 2.5TR$ (Fig. 3.1c, Fig. 3.8b). With $\theta_3 > 90°$, the slice profile of the S_3 acquisition of the ‘Four-FA’ method develops serious horns (Fig. 3.6d) which requires an additional correction for 2D MRI applications (Fig. 3.7c). A similar correction for FLASH T_1 imaging was previously reported[91], and other slice-selective T_1 imaging methods are likely to require FA- and/or TR-dependent slice-profile corrections beyond those provided by conventional B_1 or AFI mapping to achieve accurate results. The need for such correction would be signified by the presence of differences between T_1s measured in 2D and 3D images of the same subject or phantom. This, along with the fact that the image resolution along the slice selection direction usually can’t match that achievable with 3D MRI, however, may be considered minor disadvantages of 2D T_1 MRI compared to the speed-up realized by reducing the number of phase encodes vs. 3D.

Despite having the minimum theoretical number of steady-state acquisitions possible, the ‘Four-FA’ method nevertheless exhibited only average efficiency as defined by the conventional ‘Γ’ metrics, in Monte Carlo simulations (Table 3.2). Its efficiency was poorer than both multi-SE (with 14 echoes) and MRF. However, the overall accuracy of the ‘Four-FA’ method was much better than SSFP based measurements and SE, which is not accounted for in the Γ metrics. The efficiency per unit accuracy, Γ/(mean error), of the ‘Four-FA’ method was generally many times higher than the other methods, with the caveat that we presently do not know whether the newest MRF approach[68] accommodates T_2*, B_1 and slice profile effects in its library of solutions.

The primary reason for the longer acquisition times for all of the new methods proposed here, and for the ‘Four-FA’ method’s lower Γs compared to SSFP-based measurements (DESPOT1/2, IR TrueFISP, MRF), is their longer TRs. Here at 3T, the TRs were limited by RF power constraints on the long adiabatic pulses. A simple fix to this problem could be switching to a lower field. At 1.5T, for example, the SAR would be reduced to 25% or more, depending on how the scanner treats the regulatory limits on peak power. In this case, the TR in ‘Dual-τ Dual-FA’ and ‘Dual-TR Dual-FA’ could be reduced four-fold, reducing the total scan time to less than 5 mins for 7 slices in Figs 3.2, 3.3, 3.5, for example. For the ‘Four-FA’ method, SAR only affects the final acquisition with the long BIR-4 pulse, which again would be reduced four-fold at 1.5T. The ‘Four-FA’ method is in addition affected by the need for a long TR to ensure accurate B_1 measurements. As discussed, accurate knowledge of B_1 is critical to the credibility of all T_1 methods (PS, IR, DESPOT1, IR-TrueFISP). If B_1 is known, reducing TR from 600ms down to ~10ms for the ‘Four-FA’ method for example, not only reduces the scan time, but also results in a 11−22% higher T_1 efficiency (without the last acquisition) than DESPOT1 without AFI, while still maintaining its advantage of a much smaller mean error of <2%. Indeed, the much higher accuracy seen with the ‘Four-FA’ method (Table 3.2) is in good part due to the longer TR required for a much more accurate B_1 determination.

Implicit in the development of any minimum-acquisition T_1 and T_2 MRI protocols is the assumption that the number of relaxation components is limited. Here we have assumed that both are mono-exponential. Indeed, single-valued T_1s and T_2s are commonly reported for human studies, and often represent the only data available from MRI studies at a given B_0. This is not to say that multiple components do not exist. Also, multi-component relaxation may not be distinguishable from mono-component relaxation combined with tissue heterogeneity, for example, due to mixtures of GM, WM and CSF present in brain pixels. However, in our PS and SE experiments acquired at multiple time points during relaxation, we found no evidence of multi-exponential decays that could not as easily be characterized by a single exponential. Moreover, the 'Four-FA' method measures T_1 and T_2 intrinsically differently from the PS and SE methods–and at different time scales. If T_1 or T_2 relaxation were multi-component, agreement would have been be problematic.

In conclusion, the validation studies show results consistent with mapping using standard methods, and with prior published relaxation values for brain WM and GM tissue at 3T. The three methods described offer a minimum-acquisition option for imaging single-component T_1, T_2, and PD, potentially offering considerably higher efficiency per unit accuracy in the context of existing approaches, when B_1-inhomogeneity and slice profile affects are appropriately addressed.

Chapter 4. Automatic Vessel Disease Classification Using Multi-parametric IVMRI

4.1 Introduction

Lipid-bearing intravascular atherosclerotic plaques have a high risk of rupture which can clog arteries and cause stroke or myocardial infarction. Such events are responsible for 25% of all mortality worldwide [92, 93]. The plaques evolve from early-stage lesions, and their progression to those vulnerable to rupture may take decades. Differentiation of the lesions' stage is crucial to determine its progression and response to interventions. The American Heart Association (AHA) has classified atherosclerotic lesions into Types I-VI, according to their histological composition and structure[94]. Type IV – VI lesions are considered to be advanced and have a significant risk of developing complications.

There has been much research into the assessment of vessel wall characteristics using MRI, with the goal of detecting and classifying atherosclerotic lesions. Angiography visualizes the lumens of blood vessels, but the impact on vessel wall imaging has been limited. Recent studies show that the vessel wall and the presence of atherosclerosis are identifiable on T_1- and T_2-weighted black blood MRI (BBMRI) in the middle cerebral and intracranial arteries in the brains, with a resolution of ≥ 0.375 mm [95-97], but with suboptimal SNR. Ye *et al.* developed a 3D variable FA turbo SE (TSE) sequence, namely, "VISTA", with an isotropic resolution of 0.5 mm, that improved SNR by 58% compared to BBMRI with the identical voxel volume [98]. Because the average common carotid artery wall thickness is ≤ 0.75 mm[99], the vessel wall occupies only one pixel at this resolution. This leads to inaccurate quantification due to extensive partial volume effects (PVE).

On the other hand, T_1, T_2 and PD are known to reflect the intrinsic characteristics of biological tissues and are responsible for the contrast in T_1- and T_2-weighted MRIs. The absolute values of T_1, T_2 and PD, as opposed to the image intensities in weighted images, are interpretable and provide quantitative measures that could potentially be used for diagnosis, with negligible influence from instrumental factors associated with different scanners [100]. Several studies have reported the relaxation times from atherosclerotic tissues [85, 101-105]. However, currently, all MRI approaches to diagnose vessel disease relies upon weighted images [106, 107]. This is because: (i) the standard multi-parametric mapping sequences require long scan times; (ii) the limited SNR and resolution introduce quantification errors in small vessel walls; and (iii) no feasible MRI multi-parametric criteria for vessel disease classification have yet been developed.

SNR can be dramatically improved with the use of an intravascular (IV) coil [108, 109]. Recently, our group developed biocompatible IV coils [110, 111] that produce superior local SNR and ≤ 80 μm resolution at 3T. The IV coils receive signal within a radius of < 20mm. Thus, the scan time can be greatly reduced by encoding a much smaller FOV compared to receiving with conventional external coils. The IV coils can be placed at close proximity to the vessel wall, yielding a high local SNR that is sufficient for high-resolution, fast, quantitative vessel wall mapping.

We posit that the measurement of all three T_1, T_2, and PD parameters, in conjunction with high resolution fast IV MRI, can be used for comprehensive 3D classification of atherosclerotic disease. The hope is that this would provide quantitative criteria for disease characterization. Machine-learning [112] techniques have been developed and widely applied in high-dimensional classification. Supervised learning classifiers study training datasets and produce a function that can best categorize the data with minimum errors. The support vector machine (SVM) [113, 114] is a robust supervised learning algorithm that classifies the data using optimum decision boundaries in the high-dimensional feature space.

In this chapter, high-resolution, IV MRI multi-parametric mapping is reported for the first time. The parametric maps of autopsied specimens were acquired using two fast mapping methods: 1) the "Four-FA" method, with minimum theoretical steady-state acquisitions and the highest accuracy [115]; and 2) the "MIX-TSE" method that yields maps for T_1 and T_2, which span almost the full biologic range with just a single scan [116, 117]. An SVM classifier was then trained using the multi-parametric maps to automatically differentiate the vessel disease stage. The results produced by the SVM classifier were compared to histology as the standard.

4.2 Methods

Human iliac or coronary artery segments that were harvested from decedents were acquired from the Pathology Department of the Johns Hopkins Hospital and from the NICHD Brain and Tissue Bank for Developmental Disorders (Baltimore, MD). This study was approved by the Johns Hopkins IRB. Ten vessel specimens were obtained from eight patients, five of which had diagnostic information available (Table 4.1). Although all patients were diagnosed with cardiovascular disease, atherosclerotic lesions were observed at gross examination in five specimens. Specimens measured approximately 2-5 cm long, with a diameter of 0.5-2.2 cm.

Table 4.1 Patient information

Age	Sex	Race	Cause of Death
64	male	Caucasian	Pulmonary hemorrhage
61	female	-	CVD
45	male	Caucasian	ASCVD
58	male	Caucasian	ASCVD
73	male	Caucasian	MI

(CVD: cardiovascular disease, ASCVD: atherosclerotic cardiovascular disease, MI: myocardial infarction)

MRI

IVMRI was performed on a Philips 3T Achieva clinical MRI scanner (Philips Healthcare, Cleveland OH) using an in-house-built loopless IV coil. The coil consists a 2.2mm outer diameter, 400mm-long semi-rigid copper coaxial cable antenna (UT-85-C, Micro-coax Inc., Pottstown PA), and a 39mm distal whip. The IV antenna was inserted into the lumen of the vessel segment, with the specimen centered at the cable-whip junction, where the sensitivity is the highest. The specimen and the antenna were positioned at the center of a phantom filled with 3.5g L^{-1} saline to mimic the body's RF electrical properties at the MRI frequency (128 Hz).

The IV antenna was used to receive RF signals after the body coil excitation. The Four-FA method acquired $S_{1\text{-}4}$ (as in Section 3.4) with a TR=636 or 651ms; FA $\theta_{1\text{-}4}$=30°, 80°, 140°, 30°; 3D voxel size $=0.2\text{x}0.2\text{x}1.6\text{mm}^3$ or $0.27\text{x}0.27\text{x}5\text{mm}^3$; and 0° BIR4 prepulse length τ=10ms in S_4. 2D MIX-TSE was acquired with TR_{SE}=1000, TR_{IR}=1760, $TE_{1/2}$=28.6ms/100ms, TI=0.5s, and 3D voxel size = $0.2\text{x}0.2\text{x}2\text{mm}^3$. The Dixon method [118] was used to image separate water and fat components (TR=0.2s; TE=4.6, 5.8, 6.9ms; FA=55°; $0.27\text{x}0.27\text{x}3\text{mm}^3$ voxels).

Image analysis

The IVMRI intensity was corrected by a 1/r inverse scaling map, with r being the distance from the center of the antenna; or by a 2D interpolated map of the signal from saline. The Four-FA multi-parametric maps were computed using $S_{1\text{-}4}$ according to the formula in Section 3.4.1 [119]. The scanner's built-in function was used to produce the MIX-TSE multi-parametric maps.

Histology staining

Transverse sections of the specimens were stained using hematoxylin and eosin (H&E, highlights calcification, lipid core and intraplaque hemorrhage) [120], Von Kossa (highlights mineralization), Verhoeff-Van Gieson (VVG, highlights elastic fibers) or Movat (highlights various constituents of cardiovascular tissue) methods to visualize the tissue structures.

SVM classification

The training and validation of the SVM classifier were performed using an object oriented scripting language Python (version 2.7.6, Spyder 2.2.5 IDE). The tissue components of the specimens were categorized into three classes according to histology: smooth muscle cells (SMC), early disease and advanced disease. 202 data points were randomly sampled on the vessel walls in the regions with sufficient SNR and no shield current artifacts. The histology was determined using the methods as follows: early-stage lesions were stained green/blue on Movat, brown in Von Kossa and purple in VVG; advanced lesions were identified as black on Movat and VVG; SMC were stained light pink on H&E. The samples were labeled with the histology readings and the T_1, T_2, and PD values on the multi-parametric maps. The SVM was trained using the samples and tested using the "leave-one-out" [121] cross-validation method.

The three-class SVM classifier generated probabilities for each sample belonging to each class. The class exhibiting the highest probability was determined to be the output class. In addition, a receiver operating characteristic (ROC) [122] analysis was performed to depict the sensitivity and specificity. For this, the samples were regrouped into disease and healthy tissue classes and used to train a two-class SVM classifier. Adjusting the discrimination threshold from 0-1 on the output disease probability generated the ROC curve.

To compare with classification based on a single contrast, the three-class and two-class SVMs were re-trained and re-tested using only T_1, T_2 or PD as the sample feature.

4.4 Results

An example of IV MRI on one specimen with 200 μm resolution is shown in Fig 4.1a. The vessel wall structure including the plaque is clearly seen. In the Dixon lipid-only image, fat is identifiable as the hyperintense signal in the periphery of the vessel wall (Fig 4.1b). Movat and Van Kossa staining confirmed the presence of early-stage thickened fibrosis tissue (Fig 4.1c). The Four-FA T_1, T_2, and PD maps with the same resolution show adequate SNR within R<10mm (Fig 4.1d-f). The T_1 and T_2 of saline are beyond the validation range of Four-FA (see Section 3.4.5); thus, saline is masked out in the multi-parametric maps for clarity.

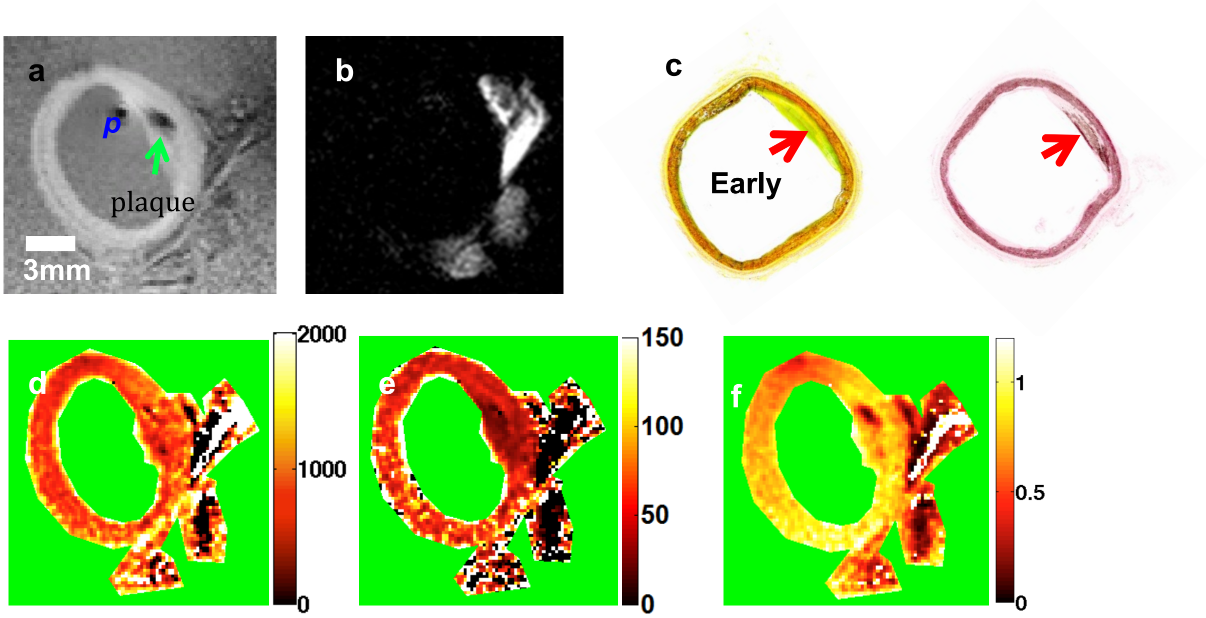

Fig 4.1 a) GRE IV vessel wall image; b) Dixon lipid image; c) Movat and Van Kossa histology results of the vessel section; d-e) color-coded Four-FA quantitative parameter maps: d) T_1 (ms), e) T_2 (ms), f) PD(pu, percent units relative to water).

The measured T_1, T_2, and PD values of the randomly sampled points were color-labeled according to their tissue classes and plotted in 3D space, with each axis representing one parameter (Fig 4.2). The T_1, T_2, and PD values of the three classes are summarized in Table 4.2. They are consistent with the published values measured at 3T: 54±13ms[85], 76±9ms[104], 69.1±6.6ms[105], and 39±5ms[103] for normal vessel wall T_2; 685.9±166ms[105] and 844±96ms[103] for normal vessel wall T_1; and 37±5ms[85], 54±3ms[104] for lipid-rich advanced lesion T_2.

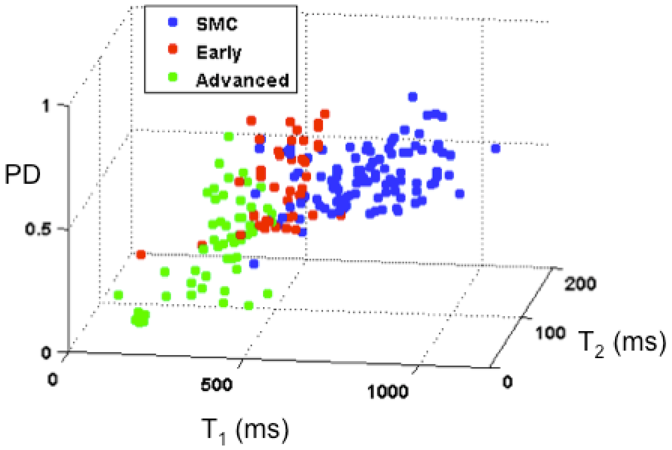

Fig 4.2 3D plot of T_1, T_2, and PD values of sampled points from three tissue classes: SMC(blue); early disease (red); and advanced disease (green).

Table 4.2. T_1, T_2, and PD measurements of autopsied human aorta

	Smooth muscle	Early disease	Advanced disease
T_1 (ms)	792±145	558±111	390±100
T_2 (ms)	62±23	44±16	34±16
PD (ms)	0.63±0.11	0.62±0.15	0.38±0.17

The “leave-one-out” cross-validation results of the three-class SVM are summarized in Table 4.3, showing that the three-class SVM correctly classified 89-93% of SMC and advanced lesions. Test results exemplifying automatic tissue classification in a vessel are shown on a T_1-weighted MRI in Fig. 4.3a. Compared to the VVG-stained histological results (Fig 4.3b), the classifier correctly detected the location of the advanced lesion in this case. The two-class SVM yielded the ROC curve (Fig 4.4), with the area under curve (AUC) =0.97.

Table 3"Leave-one-out" cross-validation results of automatic lesion stage SVM classifier compared to true histology class.

	SMC	Early	Advanced
Histology classification	105	43	54
Correctly classified	93	25	50
Misclassified	12	18	4

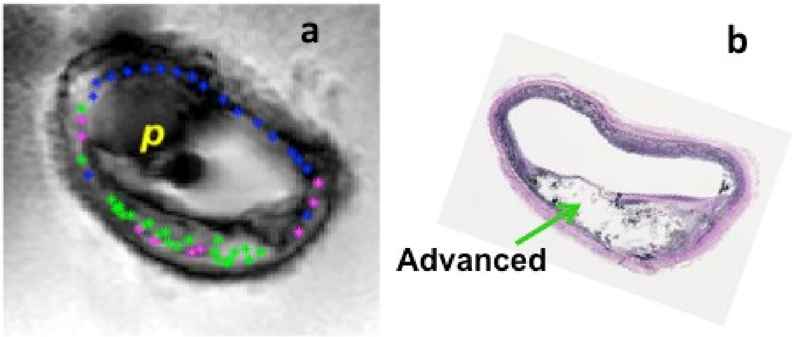

Fig 4.3 a) Color-coded classified sample points overlaid on MRI, with the same color codes as in Fig 4.2. b) Corresponding histological results. The calcium was partially lost during staining.

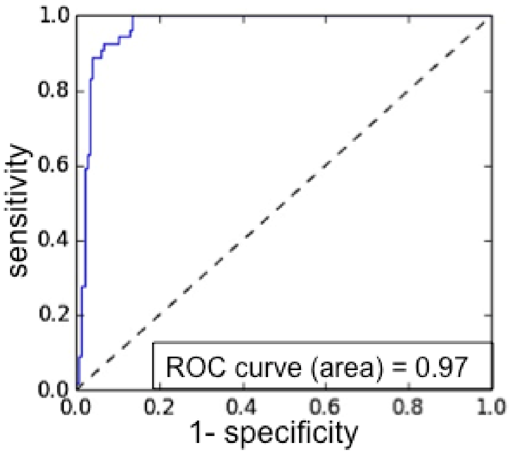

Fig 4.4 The ROC curve of the classifier to distinguish diseased and healthy tissue.

The lesion-stage classification accuracies based on one or all of the parameters are compared in Table 4.4. For the single parameter classifiers, PD outperforms the other two parameters in detecting SMC; T_1 has a higher accuracy in detecting early-stage and advanced disease. Indeed in the present study, T_1 yields the highest sensitivity and specificity in differentiating diseased from healthy tissue. However, combining all three parameters generates the highest overall accuracy.

Table 4.4 Automatic lesion stage classification accuracy based on single or multiple parameters

Parameter	**SMC(%)**	**Early(%)**	**Advanced (%)**
All-three	89	58	93
T_1	86	40	93
T_2	90	0	48
PD	98	0	48

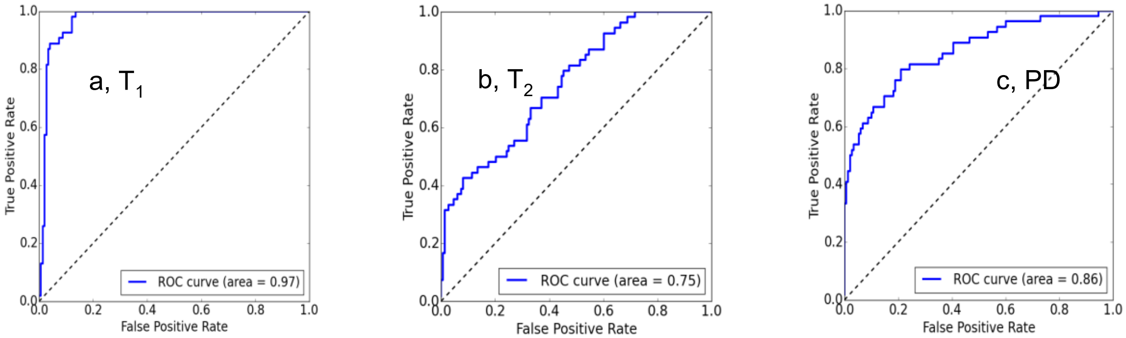

Fig 4.5 The ROC curves of the classifier based on only a) T_1, b) T_2, or c) PD.

4.5 Discussion

In this work, we demonstrated that high-resolution vessel wall T_1, T_2, PD, and lipid imaging is achievable using IV detector at 3T. The multi-parametric mapping allows absolute comparisons that do not depend on timing and instrumental factors that affect T_1- and T_2-weighted images. This potentially offers a more rigorous and reproducible basis for quantifying and discriminating vessel disease. We labeled the vessel wall T_1, T_2, and PD values with the histology-based findings and used them to train a machine-learning SVM classifier to differentiate atherosclerotic lesion stage using the MRI parameters. The automatic classifier demonstrated a three-class differential accuracy of approximately 90%, with an AUC of 0.97 in ROC analysis for disease detection.

Few studies have been published reporting vessel wall multi-parametric mapping with clinical scanners at 3T. Most vessel wall-mapping studies, regardless of the field strength, were focused on T_2 mapping[85, 104] because T_2 is believed to be a better disease indicator [104, 123]. However, in the present study, we showed that T_1 and PD also provide substantial contrast between lesions of different stages. The T_1 difference in vessel wall components was also illustrated in a study by Dalager-Pedersen *et al.* [124] at

9.4 T, which is the only report we could find that reports both T_1 and T_2 values for atherosclerotic tissue components confirmed by histology. The measured T_1 and T_2 values in the present study lie in the range of previously published values [85, 102-105], although the published values generally show poor agreement with each other.

As indicated in Table 4.2, no single contrast alone can be used to distinguish all three classes, although one or two classes are separable in one of these single parameter maps. Consequently, using all three contrasts allows more accurate classification in the 3D feature space (Fig 4.2). The three-class SVM classifier is robust to varying environmental conditions. For instance, SVM is able to produce the correct tissue class in refrigerated or formalin-fixed specimens with reduced T_1 and T_2 (results not shown). Sun *et al.*[125] performed plaque characterization with a fuzzy C-means-based classifier using only T_2; thus, the classifier may produce error results when T_2 is not measured under normal tissue conditions. Moreover, SVM partitions the 3D space with decision planes such that the normal vectors to the planes correspond to the direction in which the data points from the adjacent two classes are maximally separated. That is, the weighted images corresponding to the normal direction of the decision plane should provide the maximum contrast to distinguish the two adjacent classes.

A previous study at clinical field strength 1.5T reported that the AHA classes are differentiable using qualitative criteria based on the appearance of atherosclerotic plaques on T_1-, T_2-, PD-weighted and time-of-flight MRI with an overall accuracy of 80.2% [106]. Our studies indicate that T_1, T_2, and PD contain sufficient information to discriminate the atherosclerotic lesion stage. The SVM classifier based on the three contrasts should more precisely enable identification of atherosclerotic components and

AHA class, rather than merely provide a rough estimation of disease stage. Unfortunately, fresh human vessel specimens exhibiting various atherosclerotic components are difficult to obtain, and in the present study, the limited training data constrained our classifier to $\leq$ 3 classes.

The 3T endoscopic IV antenna has been shown to successfully perform real-time high-resolution imaging *in vivo* on clinical scanners[126]. MR endoscopy has advantages compared to other imaging modalities such as ultrasound and optical coherence tomography (OCT), in its ability to generate versatile multi-parameter contrast. With the imaging methods and classification algorithms described herein, endoscopic MRI opens the potential for real-time high-resolution detection of cardiovascular disease.

Chapter 5. Quantitative Stem Cell Tracking using Multinuclear MRI and CT

5.1 Introduction

Peripheral artery disease (PAD), caused by atherosclerotic plaque in vessels outside the heart, affects approximately eight million Americans and 12-14% of the population worldwide with a significant reduction in quality of life [127]. Up to a third of PAD patients are no longer candidates for conventional treatments, e.g., surgical or endovascular revascularization, primarily due to the excessive surgical risk or an unfavorable vascular environment [128]. To address this, a novel stem cell (SC) therapy has been demonstrated to be effective in improving vascularization and reducing pain at rest [129, 130] apparently due to paracrine mechanisms rather than direct differentiation into new blood vessels [131, 132]. However, current cell therapy suffers from low cell survival and a lack of means to monitor cell engraftment.

Cellular therapy using microencapsulated bone-marrow-derived mesenchymal stem cells (MSCs) could provide a novel means to improve vascularization in PAD patients, and enable cell tracking by adding imaging contrast agent to the microcapsules [129]. Using a rabbit PAD model, this laboratory previously demonstrated ~65% of improvement in hind limb perfusion after 14 days of the administration of X-ray-visible microencapsulated MSCs as compared to empty capsules [132]. Recently, our group has developed a PFOB-containing microcapsule, XMRCap, that not only provides an immune isolation for stem cells, but also enables noninvasive cell tracking *in vivo* with ^{19}F MRI, ultrasound (US) and X-ray [133, 134].

Noninvasive cell tracking using clinical imaging systems (e.g., MRI, CT, PET, US, etc.) is important as it enables targeted imaging of cells non-invasively, nondestructively, and repetitively *in vivo* [135, 136]. Among those, MRI, being a high resolution imaging modality that provides versatile soft tissue contrast without ionizing radiation, is particularly suitable for tracking stem cell engraftment and assessing the treatment efficacy [137]. SPIO-based MRI cell-tracking techniques, which induce strong local field distortion, have been widely adopted for their high sensitivity [4, 138]. However, the artifacts created by SPIO-labeled cells can distort the underlying anatomical MRI. Alternatively, ^{19}F is particularly suitable as a tracer for MR tracking because it doesn't alter the underlying anatomical image. While endogenous ^{19}F concentrations are negligible in the body, ^{19}F MRI could be advantageous for fluorinated cell tracking by generating positive signals with comparable imaging sensitivity to ^{1}H MRI [5, 6]. Moreover, the ^{19}F MR signal intensity is directly proportional to the number of ^{19}F atoms, offering the potential of ^{19}F concentration quantification.

Quantifying the administered microcapsules containing therapeutic cells would not only provide a measure of cell fate, but could also be useful for determining whether re-intervention or repeat treatment is necessary. However, efforts to perform such studies have thus far proved elusive. In order to quantify XMRCaps and test whether they can monitor cell fate, the following properties would be desirable: 1) that XMRCaps provide sufficient SNR and CNR in both CT and MR images; 2) that PFOB in the XMRCaps is stable and provides constant signal over the studies; and 3) that XMRCaps protect and constrain the cells for the duration of serial imaging. In this study, we have performed volume and concentration quantification of XMRCaps containing either xenogeneic (Xeno-) or allogeneic (Allo-) MSCs, in serially non-invasive tracking using flat-panel, high resolution C-arm CT and ^{19}F MRI, both *in vitro* and *in vivo* in rabbits, by comparing the signals to concentration references. To address the XMRCaps property of immune-rejection prevention, the variations in XMRCaps volume and concentration *in vivo* over time were studied and statistically compared between Xeno- and Allo-XMRCaps.

5.2 Materials and Methods

5.2.1 Phantom preparation

Empty XMRCaps with a diameter of 300±16 μm were produced using a modified alginate-poly-L-lysine microencapsulation process containing 12% PFOB, as described previously[133, 139]. Eight 0.5 ml microcentrifuge tubes were filled with empty XMRCaps at various concentrations: Tubes 1 to 5 were packed with maximum 0.5 ml XMRCaps, while Tubes 6-8 contained 0.25 ml XMRCaps well mixed with 0.25 ml 5% agarose gel (Sigma Chemical, St. Louis, MO, USA). To avoid the MRI susceptibility artifacts at the edge of the tubes, the tubes were immersed in containers filled with gelatin or agarose gel.

Four reference markers (M1-M4) made with maximally packed empty XMRCaps containing either 6%, 12% or 20% PFOB served as concentration standards to measure XMRCaps concentrations and correct for receiver coil sensitivity. M1 is a 0.5ml microcentrifuge tube, M2-M4 are the square tubes with a dimension of 1.2 x1.2 x3 cm^3. In addition, four surface markers were taped to each phased-array of the receiver coil to assist with the visualization of the coil location in ^{19}F MRI studies.

5.2.2 In vivo delivery of XMRCaps

All animal procedures were approved by the Johns Hopkins Institutional Animal Care and Use Committee. Microencapsulation of male rabbit MSCs (AlloSCs) or human MSCs (XenoSCs) was performed using the same method as empty XMRCaps but with the incorporation of MSCs at density of 6.0 $x10^6$ cells/ml. Female New Zealand White rabbits (n=10, weight 5-8kg) were sedated with ketamine (40 mg/kg) and acepromazine (1 mg/kg) intramuscularly, induced with propofol and intubated. General anesthesia was maintained with 1.5-2% isoflurane mixed with oxygen. Hind limb ischemia was induced in 5 of the 10 rabbits using a minimally invasive endovascular technique in the left superficial femoral artery (SFA) as previously described [140, 141]. 24 hours after SFA occlusion, PAD rabbits (n=5) received 6 intramuscular injections (~0.5ml /injection) of AlloSC XMRCaps into the ischemic left thigh. The normal rabbits (n=5) received 6 injections of XenoSC XMRCaps in the left thigh. The rabbits were positioned on a plastic V-board to ensure minimum movements between the imaging modalities. M1-M4 were attached to the animals (n=9) prior to imaging as shown in Fig. 5.1. The animals were imaged using the same protocols at day one, day eight and day fifteen after XMRCaps administration.

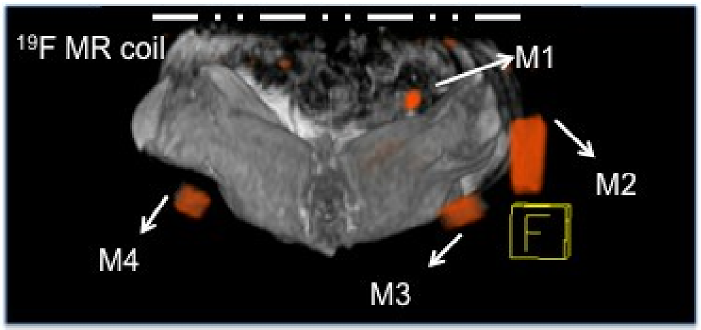

Fig 5.1 ^{19}F MRI (red) of markers (M1-M4) fused with axial maximum intensity projection (MIP) of ^{1}H MRI to indicate the location of the markers to the rabbit. (M1: 6% PFOB XMRCaps filled in a 0.5 ml tube; M2: 12% PFOB XMRCaps in a 4.3ml tube; M3, M4: 20% PFOB XMRCaps in 4.3ml tubes). The coil (dash) was placed on top of the rabbit oriented in the coronal plane.

5.2.3 C-arm CT imaging protocol

Phantom C-arm CT images were acquired on a flat-panel X-ray fluoroscopic system (Siemens Axiom Artis dFA, 20 second DynaCT preset, 240° scan angle; 0.5° increment; 0.36 μGy dose per pulse; and 48 cm FOV). Secondary reconstructions were performed using the vendor's software to yield a 0.39 mm^3 isotropic voxel size. *In vivo* C-arm CT images were acquired on the same system using the 8s body dynamic subtraction angiogram (DSA) preset and reconstructed at 0.46 mm^3 isotropic voxel size.

5.2.4 MR imaging protocol

MRI was performed on a 3.0 T MR system (Siemens Tim Trio). Phantom ^1H and ^{19}F MRI were acquired in the coronal plane. ^1H MRI was acquired with the system's body matrix coil using a GRE sequence for geometry reference (15 ms TR, 3.7 ms TE, 118 x 252 x 108mm^3 FOV; 0.49 x 0.49 x 1.5mm^3 voxel size; 20° FA; and 320 Hz/pixel receiver bandwidth). ^{19}F MR signals were acquired with a custom flexible coil consisting of a single-loop transmit coil and four phased array receivers. A B_0 field shim on the region of interest (ROI) was performed before imaging. ^{19}F MRI was performed with a 3D True fast imaging with steady state precession (TrueFISP) sequence (4.1ms TR, 2.0ms TE, 32 signal averages, 289 x 208 x 88mm^3 FOV, 1.5 x 1.5 x 2mm^3 voxel size and 1002 Hz/pixel receiver bandwidth).

In vivo MRI was performed using imaging parameters identical to those in the phantom studies with FOV adjusted to the animal size. The ^{19}F coil was positioned in the coronal plane at a fixed distance from the V-board to minimize depth variations in longitudinal quantification due to coil positioning. To test the repeatability of ^{19}F MRI, XenoSC Rabbit1 was imaged and then re-imaged on the same day with the ^{19}F coil repositioned between acquisitions.

5.2.5 Image segmentation and quantification

For visualization, the phantom and *in vivo* ^{1}H and ^{19}F MRI were registered and fused using the Siemens LEONARDO Syngo product workstation, and plotted in the same orientation for comparison.

Image segmentation and quantification were performed in Matlab (2013a, Mathworks, Natick, MA). Otsu segmentation [142] was performed in 3D ROIs to segment XMRCaps volumes in phantom CT, phantom ^{19}F MR and *in vivo* ^{19}F MR images. The *in vivo* CT images were thresholded with the lower bound of $\mu_{st} + 6\sigma_{st}$ (μ_{st}: soft tissue intensity mean, σ_{st}: soft tissue intensity standard deviation), and the upper bound of $\mu_{XMR}+6\sigma_{XMR}$ (μ_{XMR}: XMRCaps intensity mean, σ_{XMR}: XMRCaps intensity standard deviation). Volumes from CT were used as the standard.

^{19}F image intensities or CT Hounsfield units (HU) were converted to PFOB concentrations for quantification. Phantom CT HU numbers were normalized to the highest mean HU number of the phantom tubes, which was assumed to consist of pure XMRCaps containing 12% PFOB. The *in vivo* CT was calibrated by extrapolating from the HU numbers of the markers that consist of 12% and 20% PFOB XMRCaps. The ^{19}F MR image intensities were corrected by the reference ^{19}F coil's sensitivity profile. The field profile function was created using the intensities of the markers located at different depth obtained from three studies. The intensities were fitted to an exponential decay as a function of depth, using minimum least-square fitting. The function was scaled for each individual study to compensate for variations in the receiver gain.

5.2.6 Histological analysis

After humane euthanasia at the final imaging session, the hind limb tissue containing XMRCaps was harvested for histological analysis. H&E staining was performed to evaluate the microcapsule integrity. Human cell viability was determined by an anti-human nuclear antigen (HuNa) staining.

5.2.7 Statistical analysis

The alternations in XMRCaps volumes and concentrations in AlloSC and XenoSC rabbits were reported as percentage mean ± SD. To interpret these variations, two-way analysis of variance (ANOVA) with repeated measures was performed over time after delivery and cell type (R, version 3.1.1, Vienna, Austria). A probability of $p<0.05$ was considered statistically significant.

5.3 Results

The ^{19}F MRI intensities in M1-M3 were plotted as a function of the distance from the coil, *r*, after normalized to their ^{19}F concentration (Fig.5.2). The field profile function fit to the exponential decay was:

$$y=2663.[\exp(-0.03r)-0.072],\ R^2=0.86. \qquad \text{……[5.1]}$$

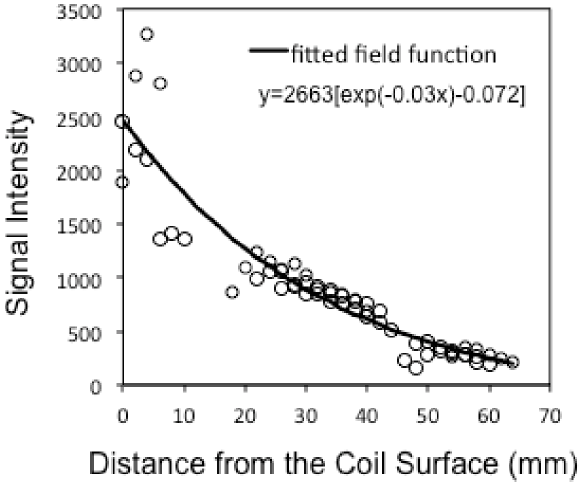

Fig 5.2 Mean signal intensities of M1-M3 in each slice vs. distance from the coil after normalization to its known concentration. Data points are fitted to the exponential function for receiver B_1 field correction.

Both CT and MRI phantom images provided a clear contrast between agarose and XMRCaps (Fig. 5.3A-B). The microcentrifuge tubes in the MRI and CT images were morphologically highly correlated. The tube volumes and the PFOB concentrations quantified from MRI and CT were highly consistent (Fig.5.3 C-D), with a relative volume deviation of 0.3±12%, and a relative concentration deviation of 3.4±13%. Tubes 3 and 6, placed at 5.8 and 6.6 cm from the coil, were excluded in Fig.5.3C-D, due to the low ^{19}F MRI SNR in those tubes.

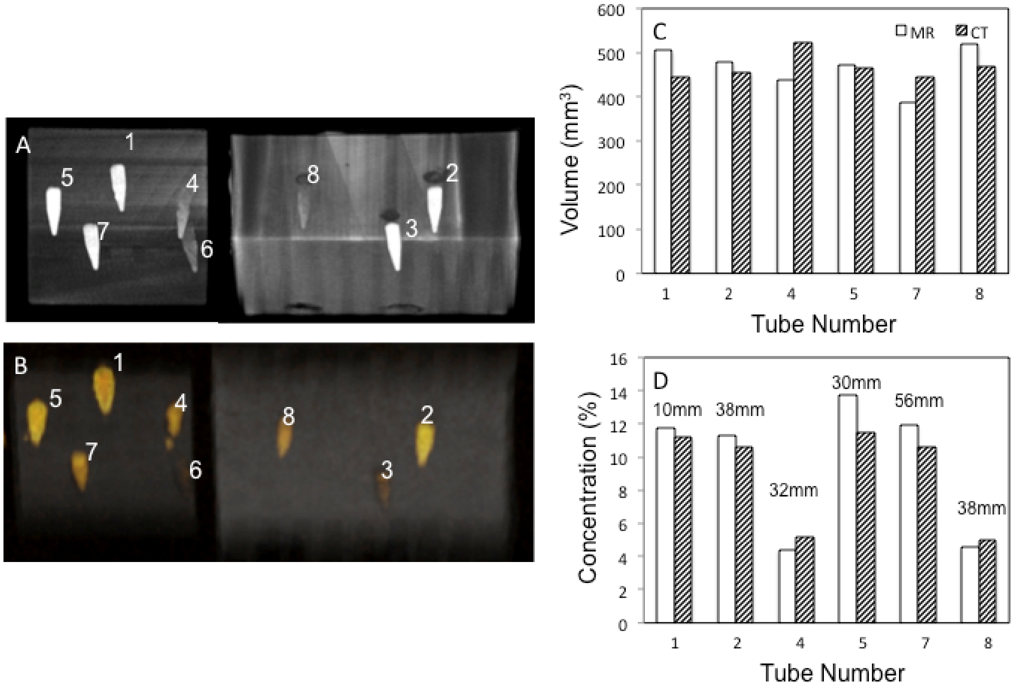

Fig 5.3 CT and MRI studies of the phantom consisting 8 tubes of fully (Tubes 1,2,3,5,7) or half (Tubes 4,6,8) concentrated XMRCaps. (A) A gray scale DynaCT image and (B) a gray scale ^{1}H MRI fused with a hot scale ^{19}F MRI of the phantom with tube number labeled. The quantification results from^{19}F MRI and CT images of tube volumes (C) and PFOB concentration (D), with the distance from the ^{19}F coil noted in (D). Tubes 3 and 6 were excluded due to low ^{19}F MRI SNR at large depth.

The injection sites in *in vivo* CT images showed high concordance to those of the MR image in all longitudinal studies (Fig.5.4). SNR of CT images was about 1.5 times of

^{19}F MRI. Because the AlloSC rabbits CT images were difficult to analyze due to the contamination of blooming artifact caused by the platinum coil, the available *in vivo* CT volumes were measured from 11 studies of 5 XenoSC rabbits. The volume and concentration quantification of *in vivo* CT and MRI in XenoSC rabbits showed good agreement. Compared to CT results, the volume and concentration deviations of ^{19}F MRI results were -9.2±12% and 8.7±15% respectively (Fig.5.5).

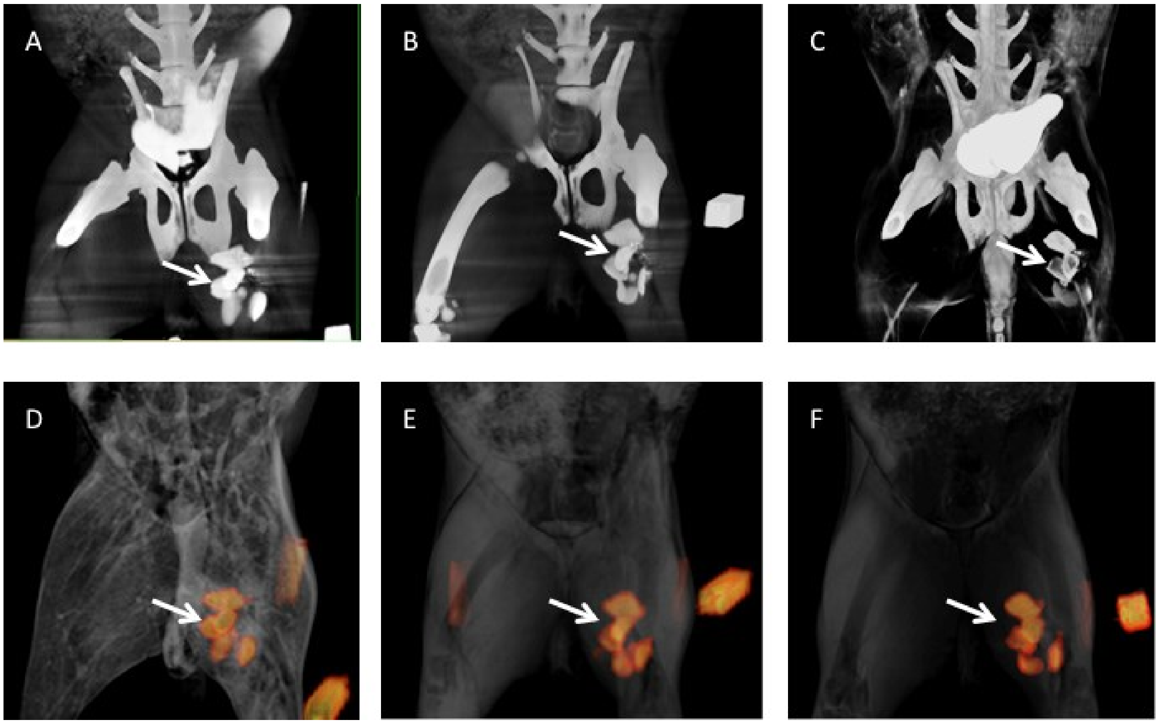

Fig 5.4 Representative CT (A-C) and fused MRI (D-F; ^{19}F:orange, ^{1}H:gray) images of an Allo-rabbit showing the injections of XMRCaps (arrow) at day 1(A,D), day 8 (B,E), and day 15 (C, F). The platinum coils in the CT images and M1, M3, and M4 in the MRI are cropped to facilitate visualization.

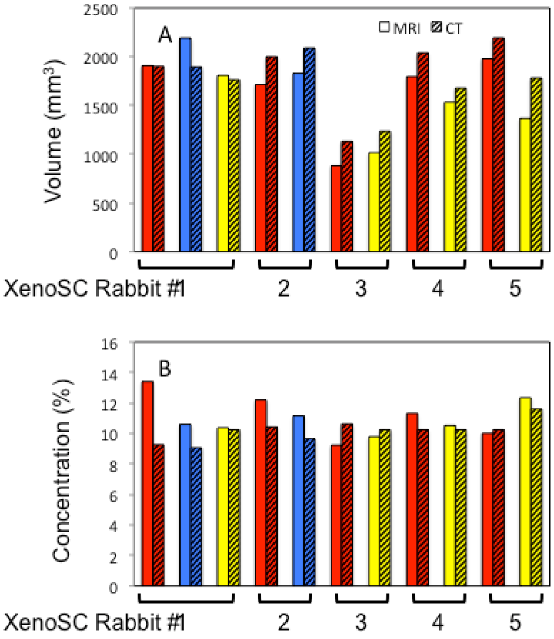

Fig 5.5 *In vivo* XMRCaps (A) volume and (B) concentration quantifications from MRI and CT images in XenoSC rabbit studies. Rabbit numbers are noted on the x-axis. Color codes time after delivery (Red-day 1, blue-day 8, and yellow-day 15)

The segmented volumes (Fig.5.6A) and intensities (Fig.5.6B) of the markers and injections from the repeated ^{19}F MRI studies are plotted vs. depth, *r*. The difference between two studies in the segmented volumes was <1.8±7.4%, and the difference in the signal intensities was <1.9±6.9%.

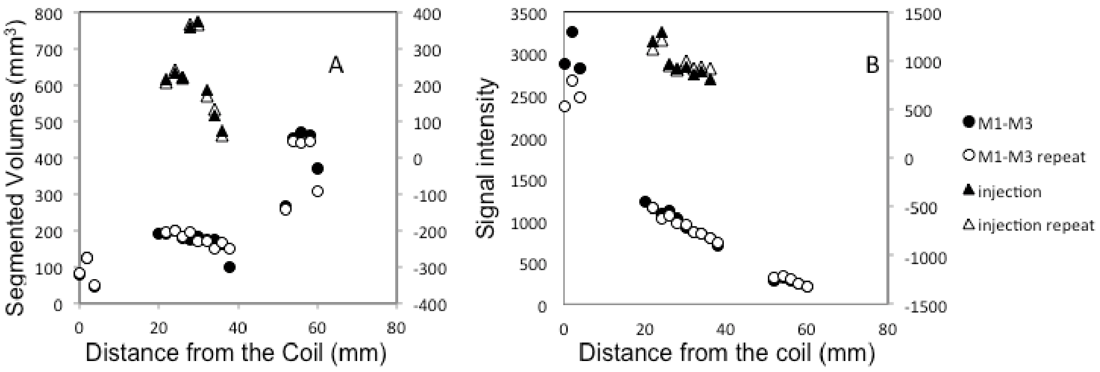

Fig 5.6 The reproducibility of quantitative ^{19}F MRI in a XenoSC Rabbit, showing the segmented volumes (A) and the volume signal intensity (B) in each slice vs. distance from the coil. The results of the markers in the first (dot) and the second (circle) studies refer to the left axis, while the results of the injection sites in the first (triangles) and the second (solid triangles) studies refer to the right axis.

Quantified volumes and concentrations of *in vivo* ^{19}F MRI for 5 AlloSC rabbits (Fig.5.7, solid lines) and 5 XenoSC rabbits (Fig. 5.7, dashed lines) at days 1, 8 and 15 were used for statistical analysis. For XMRCaps volumes, an average weekly decrease in AlloSC rabbits was 5±12.5% compared with 4.1%±17.4% in XenoSC rabbits. Because AlloSC Rabbit 2 missed the second ^{19}F MRI study, only volumes and concentrations at days 1, 8, 15 of AlloSC (n=4) and XenoSC (n=5) rabbits were included in the ANOVA test. ANOVA testing indicated no significant difference from cell types on volumes (p=0.7). For all rabbits, no significant volume variation from day 1 to day 8 was observed (p=0.8), while a significant decrease of 12±10% was evident from day 8 to day 15 (p=0.03). For concentrations, the average weekly decrease in AlloSC rabbits was 1.2%±18%, which was not significant compared to 0±12% in XenoSC rabbits (p=0.41). No significant variations were noted in all rabbits over time after delivery during week 1 (p=0.55) or week 2 (p=0.67).

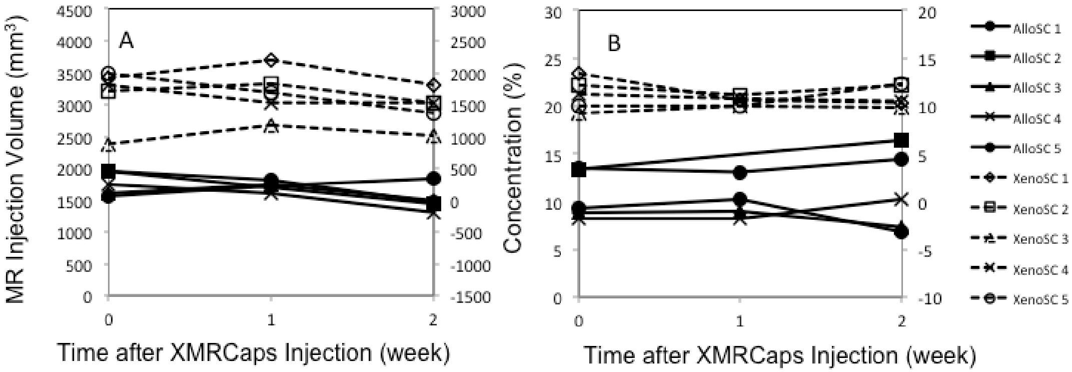

Fig 5.7 The XMRCaps injection volume (A) and concentration (B) from five AlloSC rabbits (solid lines, refer to the left axis) and five XenoSC rabbits (dashed lines, refer to the right axis) at day 1, day 8 and day 15 after delivery.

HuNa staining revealed high cell viability two weeks after administration (Fig.5.8A). H&E staining demonstrated XMRCaps remained intact (Fig.5.8B), which was consistent with CT and MR images.

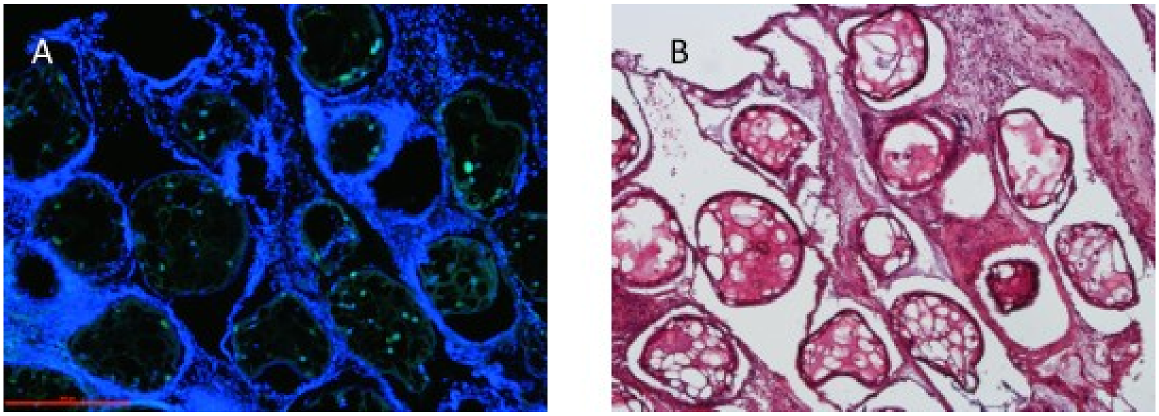

Fig 5.8 (A) Representative image of HuNa staining of the tissue from XenoSC rabbit shows the presence of live Xeno MSCs within XMRCaps 2 weeks after injection (green: live cells; blue: DAPI stained nuclei). (B) H&E of the adjacent slice shows the capsules remain intact.

2.4 Discussion

In the present study, we used quantitative CT and MRI to track stem cells serially in rabbit models. Quantification of the number of the stem cells was achieved by quantifying the PFOB signal from XMRCaps. Both CT and MRI were used to assess XMRCaps volume and concentration *in vitro* and *in vivo*. MRI was advantageous here, not only for its non-ionizing radiation, but also for its simplicity and repeatability in segmenting the ^{19}F hotspots from the background. The *in vivo* CT image segmentation was much more difficult due to the presence of the surrounding tissue, the metal artifacts from the platinum coils, or the bright vessel overlapping in the DSA images and so on.

The quantification of cells is based on the assumptions that the contrast agent remains inside the XMRCaps and that the cells are well preserved for the whole study period. In this study, we demonstrated no significant change in the PFOB signal of the XMRCaps (<5%) over two weeks *in vivo*, compared to over half of the ^{19}F signal loss 7 days after direct cell labeling using CF_3 [143]. In addition, PFOB is not only biocompatible as an FDA-approved blood substitute, but is also a synthetic oxygen carrier which sustains the cell viability. The high cell survival in the XMRCaps two weeks post-delivery may be attributed in part to the presence of PFOB. This agrees with prior studies wherein PFOB encapsulation increased cell transplantation success rates compared to alginate-only encapsulation [144]. Moreover, the T_1 value of the PFOB may be potentially used to evaluate the efficacy of new vessel development, due to the correlation between the T_1 of perfluorocarbons with the local oxygen concentration [145].

Impregnating ^{19}F into XMRCaps greatly improves the imaging sensitivity in MRI. The number of fluorine atoms in one voxel was in the order of 10^{19}, ten times more than that from direct cell labeling with ^{19}F [5, 146]. Thus the SNR is ten times higher.

However, the SNR produced by XMRCaps in ^{19}F MRI is still very low, such that 32 averages are required in ^{19}F MRI. This limits the choice to only SSFP type sequences, which provide maximum SNR per unit time. SSFP permits us to detect as low as 10caps/voxel [147], but has the well-known disadvantage of being the susceptible to B_0 field inhomogeneity, which causes banding artifacts. To minimize these effects, a local B_0 field shim was performed before imaging. The banding that sometimes still appeared in the high volume markers (M2 in particular) were excluded when computing concentrations. Moreover, the PFOB spectrum contains three fluorine peaks, which may cause chemical shift artifacts [148]. With the PFOB spectral range being more than 20 ppm wide [149], MRI was performed by centering the frequency on the peak that contained the most signal. Despite the fact that the signal from the other two peaks was insufficient to be visually observed in the images, we minimized the measurement error by acquiring ^{19}F MRI with a large bandwidth (1002Hz/pixel), such that the induced chemical shift differences between the furthest peaks would not exceed three pixels.

The CT and MR images were segmented using Otsu's method (^{19}F MRI and phantom CT) or hard thresholding (*in vivo* CT). Otsu's method[142] automatically thresholds the image into two classes with a minimum within-class variance, and no input parameters are needed. It is preferable here for its adaptiveness to the imaging gain variations and its high repeatability, except for *in vivo* CT images, which consist more than two tissue classes. For the segmentation of *in vivo* CT images, the HU number of XMRCaps (~400) can be distinguished from that of soft tissue (~0) and bone (varies from 700 to 3000) [150], thus thresholding with an upper and a lower bound was suitable. All of the segmentation algorithms are automatic with a roughly defined-ROI, which were found to be 100% reproducible.

The CT image has a voxel size that is more than 45 times smaller than that of the ^{19}F MR images, and no spatial field variations, thus the CT volumes were served as the standard. The segmented MRI volumes were consistent with CT volumes (on average <1% error in phantoms). However, the larger voxel size in MR reduces the accuracy of volume measurements due to PVE. The Otsu method was able to minimize this error by separating two classes based on the histogram distribution rather than merely the intensity values. Thus, the partially filled voxels are assigned to foreground or background with an optimized probability. In contrast, the hard thresholding with $\mu+6\sigma$ was not suitable for the low-resolution ^{19}F MRI segmentation, as it mostly assigned the partially-filled voxels to the foreground.

^{19}F MRI signal is proportional to the ^{19}F spin density, thus it is directly proportional to the PFOB concentration. The acquired ^{19}F signal follows the detector coil's field profile function [5.1]. An increase of the depth from 1cm to 5.8cm, for example, causes an 80% signal loss, resulting in the exclusion of Tube 3 and Tube 6 in phantom MRI analysis. This would potentially limit the effective imaging depth of the coil to < 6cm. A volume ^{19}F coil is anticipated to generate a more homogenous field. The HU number in CT was demonstrated to be roughly linear with the physical density in certain tissues [151]. Although the quantification of PFOB concentration in CT was based on this assumption of linearity, the markers were used to calibrate out any non-linearity or offsets. However, the underlying mechanism of CT imaging contrast is not directly related to molecule density, thus even though the measured concentrations were consistent, MRI, rather than CT, should be treated as the standard PFOB concentration measurement.

The MRI serial tracking shows a slight decrease in the XMRCaps volumes (<5%) and concentration (<2%) with a high reproducibility *in vivo*. The lost volume is most likely due to the settlement of the loose XMRCaps injections and insufficient SNR. The concentration and volume oscillations over time reflect the measurement error. Previous published studies indicate that large voxels in MRI cause up to 20% errors [152, 153]. Imaging with smaller voxels will reduce this error, but also result in longer scan time for the same SNR.

The success in *in vivo* XMRCaps tracking using both CT and ^{19}MRI leads to a prospective therapeutic regime for PAD. XMRCaps delivery can be monitored in real-time using CT with high-resolution. Metallic needles, which are compatible with CT, generate high contrast against soft tissue, ensuring the precision delivery to the target location. PFOB greatly improves the visibility of XMRCaps under CT for monitoring the injection dose. Then ^{19}F MRI can be performed for follow-up cell tracking, which eliminates the patients' exposure to ionizing radiation. In addition, with ^{1}H MR angiography sequences, it is possible to monitor the SC engraftment and the treatment efficacy using a single imaging modality.

In conclusion, CT and ^{19}F MRI of the XMRCaps provides a novel means to track SCs in a non-invasive fashion. Segmentation and calibration algorithms were developed for accurate quantification and successfully validated in both volume and concentration measurements. The results of serial ^{19}F MRI tracking of the XMRCaps and the histological staining proved that XMRCaps prevent immunorejection. The combination of the two modalities offers great potential for quantitative monitoring of therapeutic cell delivery and tracking engraftment in PAD therapy. Future work is needed to eliminate MRI artifacts resulted from chemical shift and field inhomogeneities.

Chapter 6. Conclusion and Future Works

6.1 Conclusion

MRI produces soft tissue contrast superior to that of any other imaging modality, and is thus ideally suited to detecting soft tissue pathology. Quantification of the factors that characterize contrast, enables absolute comparisons between images from different studies, potentially providing a quantitative standard for disease diagnosis and a means of monitoring response to therapy. In this dissertation, we developed several quantitative parameter-mapping methods, and explored the potential of quantitative MRI for classifying vessel disease and for tracking the delivery of cell therapy.

First, the Dual-τ T_2 mapping method was introduced, which utilizes the fact that the spins undergo T_2 decay during long adiabatic pulses. This method yields high accuracy in tissues with short T_2s, such as muscle, cartilage and white matter. The Dual-τ method is relatively immune to B_0 and B_1 inhomogeneity, due to their use of adiabatic pulses. It was shown that T_2 contrast can be introduced to MRI by adding a 0° FA adiabatic pre-pulse to an imaging sequence. The method was validated both in phantoms and *in vivo* in humans, and produced accurate T_2 values compared to gold standard SE T_2 measurements. This work was published in *Journal of Magnetic Resonance* [69] and a patent application was filed on it in 2012[154].

The Dual-τ method was further explored and extended for the simultaneous mapping of all the standard MRI contrast parameters – T_1, T_2, and PD. Three new methods with a minimum number of acquisitions were developed therefrom. In particular, the Four-FA method provides T_1, T_2, and PD maps that incorporate a B_1 field inhomogeneity self-correction with only four acquisitions. Compared to existing mapping methods, such as DESPOT1/2 or IR TrueFISP, the Four-FA method performed best overall in terms of accuracy, while exhibiting high efficiency per unit accuracy. These methods were validated in phantoms and *in vivo* in the human brain, and also published in the *Journal of Magnetic Resonance*, in 2014 [115].

After the development of novel mapping methods, the value of multi-parametric mapping for characterizing vessel disease was explored. We first demonstrated that high-resolution vessel wall T_1, T_2, PD, and fat imaging are achievable using an IV detector at 3T. Then, a machine-learning-based classifier was trained using the vessel wall T_1, T_2, and PD values, which were labeled with the pathology results to differentiate atherosclerotic lesion stages. The automatic classifier demonstrated a three-class differential accuracy of approximately 90%, with an AUC of 0.97 in the ROC analysis for disease detection. This work was presented at *International Society of Magnetic Resonance in Medicine* conferences in 2014 and 2015.

Finally, direct quantification of the image intensities was used to measure the delivery and fate of an encapsulated cell therapy. We performed quantitative serial stem cell-tracking in rabbit models using CT and ^{19}F MR images. Segmentation and calibration algorithms were developed for accurate quantification. Both CT and MRI were able to non-invasively assess XMRCaps volume and concentration *in vitro* and *in vivo*. The constant signal level during the serial ^{19}F MRI tracking of the XMRCaps and the cell integrity two weeks after administration proved that the XMRCaps preparation could successfully avoid immunorejection. This work was presented at the *World Molecular Imaging Conference* in 2012, and the *International Society of Magnetic*

Resonance in Medicine and *Society for Cardiovascular Magnetic Resonance* conferences in 2013.

6.2 Future works

T_1, T_2, and PD are the intrinsic factors that affect MRI contrast. However, long acquisition times are potentially limiting for clinical T_1, T_2, and PD mapping, and increase the likelihood of motion artifacts. Recently, *spectroscopy with linear algebraic modeling* (SLAM) was developed for MRS and CEST to reduce scan times up to 120-fold by delivering compartment-averaged spectroscopy signals that were reconstructed from a small subset of those *k*-space acquisitions with the highest SNR[155, 156]. Currently, we are testing the feasibility of combining SLAM with MRI to yield compartment-averaged T_1, T_2 and PD measures. In the initial attempt, the SLAM measurements were validated with a standard "MIX" sequence [157] in human vessel specimens with IV MRI and are compared with those from the conventional full *k*-space FT reconstruction acquired at 3T.

A segmented FOV from a diseased vessel (myelodysplastic syndrome) is exemplified in Fig.6.1 (fat=F; lesion=L; vessel fluid contents=W1; smooth vessel-wall muscle=SM; surrounding tissue=W2). SLAM results for the vessel wall are plotted against acceleration factor, *R* in Fig. 6.2, with error-bands indicating compartment mean ± SD measured in the FT-MIX maps. For $R \leq 10$, SLAM T_1, T_2, and PD measurements in all compartments fall within the mean ± SD of the FT results. In both lesion compartments (L1, L2) and F, and with R=10, errors in the three parameters are $\leq$

0.5%(±4%) compared to the FT mean. Even in W1 and W2, where the SD of T_1 and PD are ≥30% in the FT maps, SLAM T_1 and PD agree with the FT means within ≤6%±6%.

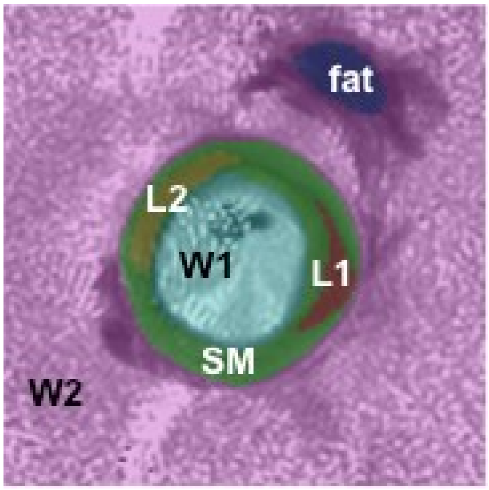

Fig 6.1 Anatomical compartment masks of a diseased vessel overlaid on vessel IV MRI.

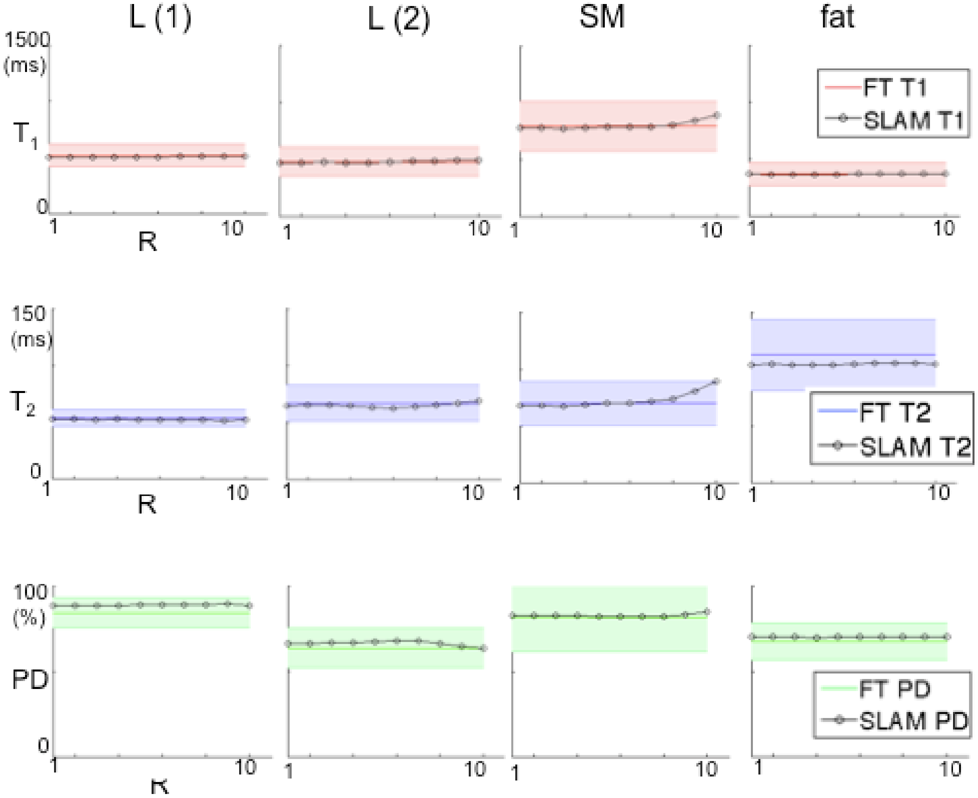

Fig 6.2 SLAM T_1, T_2, and PD values vs. *R*. The error bands denote compartment mean±SD derived from the FT maps. SLAM and FT measures of T_1, T_2, and PD agree.

The initial results show that acceleration methods enable fast and accurate multi-parametric mapping, which could satisfy the time limitations in routine clinical MRI and provide quantitative measures of quantitative value. Considering this, the value of the multi-parametric maps should be further explored, including the creation of quantitative criteria for tissue component discrimination, as well as the generation of the optimum contrast images using the maps.

REFERENCE

1. Lauterbur PC: **Image formation by induced local interactions: examples employing nuclear magnetic resonance.** *Nature* 1973, **242:**190-191.
2. Edeistein WA, Bottomley PA: **Magnetic resonance without nuclei?** *Radiology* 1984, **152:**237-237.
3. Ahrens ET, Bulte JWM: **Tracking immune cells in vivo using magnetic resonance imaging.** *Nat Rev Immunol* 2013, **13:**755-763.
4. Kraitchman DL, Gilson WD, Lorenz CH: **Stem cell therapy: MRI guidance and monitoring.** *Journal of Magnetic Resonance Imaging* 2008, **27:**299-310.
5. Boehm-Sturm P, Mengler L, Wecker S, Hoehn M, Kallur T: **<italic>In Vivo</italic> Tracking of Human Neural Stem Cells with ¹⁹F Magnetic Resonance Imaging.** *PLoS ONE* 2011, **6:**e29040.
6. Srinivas M, Heerschap A, Ahrens ET, Figdor CG, Vries IJM: **< sup> 19</sup> F MRI for quantitative< i> in vivo</i> cell tracking.** *Trends in biotechnology* 2010, **28:**363-370.
7. Rabi II: **Space Quantization in a Gyrating Magnetic Field.** *Physical Review* 1937, **51:**652-654.
8. Rabi II: **On the Process of Space Quantization.** *Physical Review* 1936, **49:**324-328.
9. **Isidor Isaac Rabi** [http://www.britannica.com/biography/Isidor-Isaac-Rabi]
10. Purcell EM: **Spontaneous emission probabilities at radio frequencies.** In.; 1946: 681.
11. Bloch F: **Nuclear induction.** *Physical review* 1946, **70:**460.
12. Bloembergen N, Purcell EM, Pound RV: **Relaxation effects in nuclear magnetic resonance absorption.** *Physical Review* 1948, **73:**679.
13. Hahn EL: **Spin echoes.** *Physical review* 1950, **80:**580.
14. Ernst RR: **Nuclear Magnetic Resonance Fourier Transform Spectroscopy (Nobel Lecture).** *Angewandte Chemie International Edition in English* 1992, **31:**805-823.
15. Mansfield P: **Multi-planar image formation using NMR spin echoes.** *Journal of Physics C: Solid State Physics* 1977, **10:**L55.
16. Wuthrich K: *NMR of proteins and nucleic acids.* Wiley; 1986.
17. Koradi R, Billeter M, Wüthrich K: **MOLMOL: A program for display and analysis of macromolecular structures.** *Journal of Molecular Graphics* 1996, **14:**51-55.
18. Mallard J, Hutchison J, Edelstein W, Ling C, Foster M, Johnson G, Cox S, Lauterbur P, Mansfield P, Wilkie D: **In vivo nmr Imaging in Medicine: The Aberdeen Approach, both Physical and Biological [and Discussion].** *Philosophical Transactions of the Royal Society of London Series B, Biological Sciences* 1980**:**519-530.
19. Edelstein WA, Hutchison JM, Johnson G, Redpath T: **Spin warp NMR imaging and applications to human whole-body imaging.** *Physics in medicine and biology* 1980, **25:**751-756.

20. Yuri L, Ernst Wolfgang S, Tao Z: **Novel technologies and configurations of superconducting magnets for MRI.** *Superconductor Science and Technology* 2013, **26:**093001.
21. Vaughan T, DelaBarre L, Snyder C, Tian J, Akgun C, Shrivastava D, Liu W, Olson C, Adriany G, Strupp J, et al: **9.4T human MRI: Preliminary results.** *Magnetic Resonance in Medicine* 2006, **56:**1274-1282.
22. Schepkin VD, Brey WW, Gor'kov PL, Grant SC: **Initial in vivo rodent sodium and proton MR imaging at 21.1 T.** *Magnetic resonance imaging* 2010, **28:**400-407.
23. Haacke EM, Brown RW, Thompson MR, Venkatesan R: *Magnetic Resonance Imaging: Physical Principles and Sequence Design.* St. Louis: Mosby; 1999.
24. Nishimura DG: *Principles of magnetic resonance imaging.* Stanford University; 1996.
25. Mansfield P: *Nmr imaging in biomedicine: Supplement 2 advances in magnetic resonance.* Elsevier; 1982.
26. Erdman WA: **Biomedical Magnetic Resonance Imaging: Principles, Methodology, and Applications.** *Radiology* 1990, **174:**462-462.
27. Bottomley PA, Hardy CJ, Argersinger RE, Allen-Moore G: **A review of 1H nuclear magnetic resonance relaxation in pathology: are T1 and T2 diagnostic?** *Medical physics* 1987, **14:**1-37.
28. Bottomley PA, Foster TH, Argersinger RE, Pfeifer LM: **A review of normal tissue hydrogen NMR relaxation times and relaxation mechanisms from 1–100 MHz: Dependence on tissue type, NMR frequency, temperature, species, excision, and age.** *Medical physics* 1984, **11:**425-448.
29. Stanisz GJ, Odrobina EE, Pun J, Escaravage M, Graham SJ, Bronskill MJ, Henkelman RM: **T1, T2 relaxation and magnetization transfer in tissue at 3T.** *Magnetic resonance in medicine : official journal of the Society of Magnetic Resonance in Medicine / Society of Magnetic Resonance in Medicine* 2005, **54:**507-512.
30. Gold GE, Han E, Stainsby J, Wright G, Brittain J, Beaulieu C: **Musculoskeletal MRI at 3.0 T: Relaxation Times and Image Contrast.** *Am J Roentgenol* 2004, **183:**343-351.
31. Kleine LJ, Mulkern RV, Guttmann CR, Colucci VM, Jolesz FA: **In vivo characterization of cytotoxic intracellular edema by multicomponent analysis of transverse magnetization decay curves.** *Academic radiology* 1995, **2:**365-372.
32. Does MD, Snyder RE: **Multiexponential T2 relaxation in degenerating peripheral nerve.** *Magnetic Resonance in Medicine* 1996, **35:**207-213.
33. Frey HE, Knispel RR, Kruuv J, Sharp AR, Thompson RT, Pintar MM: **Proton Spin-Lattice Relaxation Studies of Nonmalignant Tissues of Tumorous Mice.** *Journal of the National Cancer Institute* 1972, **49:**903-906.
34. Rogers WJ, Prichard JW, Hu YL, Olson PR, Benckart DH, Kramer CM, Vido DA, Reichek N: **Characterization of signal properties in atherosclerotic plaque components by intravascular MRI.** *Arteriosclerosis, thrombosis, and vascular biology* 2000, **20:**1824-1830.

35. Meiboom S, Gill D: **Modified Spin-Echo Method for Measuring Nuclear Relaxation Times.** *Review of Scientific Instruments* 1958, **29:**688-691.
36. Rose A: *Vision: human and electronic.* Springer Science & Business Media; 2013.
37. Feinstein A: *The clinical neuropsychiatry of multiple sclerosis.* Cambridge University Press; 2007.
38. Erbay SH, Brewer E, French R, Midle JB, Zou KH, Lee GM, Erbay KD, Bhadelia RA: **T2 hyperintensity of medial lemniscus is an indicator of small-vessel disease.** *AJR American journal of roentgenology* 2012, **199:**163-168.
39. Chowdhury R, Wilson I, Rofe C: *Radiology at a Glance.* John Wiley & Sons; 2010.
40. Geraldes CF, Laurent S: **Classification and basic properties of contrast agents for magnetic resonance imaging.** *Contrast media & molecular imaging* 2009, **4:**1-23.
41. Gilad AA, Walczak P, McMahon MT, Na HB, Lee JH, An K, Hyeon T, van Zijl PCM, Bulte JWM: **MR tracking of transplanted cells with "positive contrast" using manganese oxide nanoparticles.** *Magnetic Resonance in Medicine* 2008, **60:**1-7.
42. Abragam A: **The Principles of Nuclear Magnetism.** *Oxford, Clarendon Press* 1961**:**599.
43. Norris DG: **Adiabatic radiofrequency pulse forms in biomedical nuclear magnetic resonance.** *Concepts in Magnetic Resonance* 2002, **14:**89-101.
44. De Graaf RA, Nicolay K: **Adiabatic rf pulses: Applications to in vivo NMR.** *Concepts in Magnetic Resonance* 1997, **9:**247-268.
45. Silver MS, Joseph RI, Hoult DI: **Highly selective [pi]/2 and [pi] pulse generation.** *Journal of Magnetic Resonance (1969)* 1984, **59:**347-351.
46. Hardy CJ, Edelstein WA, Vatis D: **Efficient adiabatic fast passage for NMR population inversion in the presence of radiofrequency field inhomogeneity and frequency offsets.** *J Magn Reson* 1986, **66:**470-482.
47. Garwood M, Ke Y: **Symmetric pulses to induce arbitrary flip angles with compensation for rf inhomogeneity and resonance offsets.** *Journal of Magnetic Resonance (1969)* 1991, **94:**511-525.
48. Bottomley PA, Ouwerkerk R: **BIRP: an improved implementation of low-angle adiabatic (BIR-4) excitation pulses.** *J Magn Reson Ser A* 1993, **103:**242-244.
49. Robin Bendall M, Garwood M, Uğurbil K, Pegg DT: **Adiabatic refocusing pulse which compensates for variable of power and off-resonance effects.** *Magnetic Resonance in Medicine* 1987, **4:**493-499.
50. El-Sharkawy A-M, Schar M, Ouwerkerk R, Weiss RG, Bottomley PA: **Quantitative Cardiac ^{31}P Spectroscopy at 3 Tesla Using Adiabatic Paulses.** *Magnetic Resonance in Medicine* 2009, **61**.
51. Bottomley PA, Edelstein WA: **NMR imaging of the transverse relaxation time using multiple spin echo sequences.** In *Book NMR imaging of the transverse relaxation time using multiple spin echo sequences* (Editor ed.^eds.). City: General Electric Company (Schenectady, NY); 1985.

52. Bottomley PA, Ouwerkerk R: **The Dual-Angle Method for Fast, Sensitive T1 Measurement in Vivo with Low-Angle Adiabatic Pulses.** *Journal of Magnetic Resonance, Series B* 1994, **104:**159-167.
53. Nezafat R, Ouwerkerk R, Derbyshire AJ, Stuber M, McVeigh ER: **Spectrally selective B1-insensitive T2 magnetization preparation sequence.** *Magnetic Resonance in Medicine* 2009, **61:**1326-1335.
54. Bottomley PA, Edelstein WA: **Method of eliminating effects of spurious free induction decay NMR signal caused by imperfect 180 degrees pulses.** In *Book Method of eliminating effects of spurious free induction decay NMR signal caused by imperfect 180 degrees pulses* (Editor ed.^eds.). City: General Electric Company (Schenectady, NY); 1984.
55. Bittoun J, Taquin J, Sauzade M: **A computer algorithm for the simulation of any Nuclear Magnetic Resonance (NMR) imaging method.** *Magnetic Resonance Imaging* 1984, **2:**113-120.
56. Yoshimura K, Kato H, Kuroda M, Yoshida A, Hanamoto K, Tanaka A, Tsunoda M, Kanazawa S, Shibuya K, Kawasaki S, Hiraki Y: **Development of a tissue-equivalent MRI phantom using carrageenan gel.** *Magnetic Resonance in Medicine* 2003, **50:**1011-1017.
57. Naressi A, Couturier C, Devos JM, Janssen M, Mangeat C, Beer Rd, Graveron-Demilly D: **Java-based Graphical User Interface for the MRUI Quantitation Package.** *MAGMA* 2001, **12:**141-152.
58. Moran PR, Hamilton CA: **Near-resonance spin-lock contrast.** *Magnetic Resonance Imaging* 1995, **13:**837-846.
59. Gelman N, Gorell JM, Barker PB, Savage RM, Spickler EM, Windham JP, Knight RA: **MR Imaging of Human Brain at 3.0 T: Preliminary Report on Transverse Relaxation Rates and Relation to Estimated Iron Content.** *Radiology* 1999, **210:**759-767.
60. Deoni SCL, Rutt BK, Peters TM: **Rapid combined T1 and T2 mapping using gradient recalled acquisition in the steady state.** *Magnetic Resonance in Medicine* 2003, **49:**515-526.
61. Schmitt P, Griswold MA, Jakob PM, Kotas M, Gulani V, Flentje M, Haase A: **Inversion recovery TrueFISP: Quantification of T1, T2, and spin density.** *Magnetic Resonance in Medicine* 2004, **51:**661-667.
62. Heule R, Ganter C, Bieri O: **Triple echo steady-state (TESS) relaxometry.** *Magnetic Resonance in Medicine* 2013**:**n/a-n/a.
63. Bieri O, Scheffler K: **On the origin of apparent low tissue signals in balanced SSFP.** *Magnetic Resonance in Medicine* 2006, **56:**1067-1074.
64. Tong CY, Prato FS: **A novel fast T1-mapping method.** *Journal of Magnetic Resonance Imaging* 1994, **4:**701-708.
65. Look DC, Locker DR: **Time Saving in Measurement of NMR and EPR Relaxation Times.** *Review of Scientific Instruments* 1970, **41:**250-251.
66. Haase A, Matthaei D, Bartkowski R, Dühmke E, Leibfritz D: **Inversion recovery snapshot FLASH MR imaging.** *Journal of computer assisted tomography* 1989, **13:**1036.

67. Ehses P, Seiberlich N, Ma D, Breuer FA, Jakob PM, Griswold MA, Gulani V: **IR TrueFISP with a golden-ratio-based radial readout: Fast quantification of T1, T2, and proton density.** *Magnetic Resonance in Medicine* 2013, **69:**71-81.
68. Ma D, Gulani V, Seiberlich N, Liu K, Sunshine JL, Duerk JL, Griswold MA: **Magnetic resonance fingerprinting.** *Nature* 2013, **495:**187-192.
69. Wang G, El-Sharkawy AM, Edelstein WA, Schär M, Bottomley PA: **Measuring T2 and T1, and imaging T2 without spin echoes.** *J Magn Reson* 2012, **214:**273-280.
70. Fram EK, Herfkens RJ, Johnson GA, Glover GH, Karis JP, Shimakawa A, Perkins TG, Pelc NJ: **Rapid calculation of T1 using variable flip angle gradient refocused imaging.** *Magnetic Resonance Imaging* 1987, **5:**201-208.
71. Freeman R, Hill H: **Fourier transform study of NMR spin–lattice relaxation by "Progressive Saturation".** *The Journal of Chemical Physics* 1971, **54:**3367.
72. Edelstein WA, Bottomley PA, Hart HR, Smith LS: **Signal, noise, and contrast in nuclear magnetic resonance (NMR) imaging.** *J Comput Assist Tomogr* 1983, **7:**391-401.
73. Bottomley PA, Ouwerkerk R: **BIRP, an improved implementation of low-angle adiabatic (BIR-4) excitation pulses.** *J Magn Reson Ser A* 1993, **103:**242-244.
74. Volz S, Nöth U, Deichmann R: **Correction of systematic errors in quantitative proton density mapping.** *Magnetic Resonance in Medicine* 2012, **68:**74-85.
75. Wansapura JP, Holland SK, Dunn RS, Ball WS: **NMR relaxation times in the human brain at 3.0 tesla.** *Journal of Magnetic Resonance Imaging* 1999, **9:**531-538.
76. Ethofer T, Mader I, Seeger U, Helms G, Erb M, Grodd W, Ludolph A, Klose U: **Comparison of longitudinal metabolite relaxation times in different regions of the human brain at 1.5 and 3 Tesla.** *Magnetic Resonance in Medicine* 2003, **50:**1296-1301.
77. Stanisz GJ, Odrobina EE, Pun J, Escaravage M, Graham SJ, Bronskill MJ, Henkelman RM: **T1, T2 relaxation and magnetization transfer in tissue at 3T.** *Magnetic Resonance in Medicine* 2005, **54:**507-512.
78. Deoni SCL: **High-resolution T1 mapping of the brain at 3T with driven equilibrium single pulse observation of T1 with high-speed incorporation of RF field inhomogeneities (DESPOT1-HIFI).** *Journal of Magnetic Resonance Imaging* 2007, **26:**1106-1111.
79. Yarnykh VL: **Actual flip-angle imaging in the pulsed steady state: A method for rapid three-dimensional mapping of the transmitted radiofrequency field.** *Magnetic Resonance in Medicine* 2007, **57:**192-200.
80. Joseph PM, Axel L, O'Donnell M: **Potential problems with selective pulses in NMR imaging systems.** *Medical physics* 1984, **11:**772.
81. Schär M, Vonken E-J, Stuber M: **Simultaneous B0- and B1+-Map acquisition for fast localized shim, frequency, and RF power determination in the heart at 3 T.** *Magnetic Resonance in Medicine* 2010, **63:**419-426.
82. Edelstein WA, Bottomley PA: **Method of three-dimensional NMR imaging using selective excitation.** In *Book Method of three-dimensional NMR imaging using selective excitation* (Editor ed.^eds.). City: Google Patents; 1984.

83. Crawley AP, Henkelman RM: **A comparison of one-shot and recovery methods in T1 imaging.** *Magnetic Resonance in Medicine* 1988, **7:**23-34.
84. Cheng HLM, Wright GA: **Rapid high-resolution T1 mapping by variable flip angles: Accurate and precise measurements in the presence of radiofrequency field inhomogeneity.** *Magnetic Resonance in Medicine* 2006, **55:**566-574.
85. Biasiolli L, Lindsay A, Chai J, Choudhury R, Robson M: **In-vivo quantitative T2 mapping of carotid arteries in atherosclerotic patients: segmentation and T2 measurement of plaque components.** *Journal of Cardiovascular Magnetic Resonance* 2013, **15:**69.
86. Hurley SA, Yarnykh VL, Johnson KM, Field AS, Alexander AL, Samsonov AA: **Simultaneous variable flip angle–actual flip angle imaging method for improved accuracy and precision of three-dimensional T1 and B1 measurements.** *Magnetic Resonance in Medicine* 2012, **68:**54-64.
87. Hinshaw WS: **Image formation by nuclear magnetic resonance: The sensitive‐point method.** *Journal of Applied Physics* 1976, **47:**3709-3721.
88. Carr HY: **Steady-State Free Precession in Nuclear Magnetic Resonance.** *Physical Review* 1958, **112:**1693-1701.
89. El-Sharkawy A-MM, Qian D, Bottomley PA, Edelstein WA: **A multichannel, real-time MRI RF power monitor for independent SAR determination.** *Medical physics* 2012, **39:**2334.
90. Venkatesan R, Lin W, Haacke EM: **Accurate determination of spin-density and T1 in the presence of RF-field inhomogeneities and flip-angle miscalibration.** *Magnetic Resonance in Medicine* 1998, **40:**592-602.
91. Gras V, Abbas Z, Shah NJ: **Spoiled FLASH MRI with slice selective excitation: Signal equation with a correction term.** *Concepts in Magnetic Resonance Part A* 2013, **42:**89-100.
92. Mathers C, Fat DM, Boerma J: *The global burden of disease: 2004 update.* World Health Organization; 2008.
93. Organization WH: *World health statistics 2014.* World Health Organization; 2014.
94. Stary HC, Chandler AB, Dinsmore RE, Fuster V, Glagov S, Insull W, Rosenfeld ME, Schwartz CJ, Wagner WD, Wissler RW: **A definition of advanced types of atherosclerotic lesions and a histological classification of atherosclerosis A report from the Committee on Vascular Lesions of the Council on Arteriosclerosis, American Heart Association.** *Circulation* 1995, **92:**1355-1374.
95. Xu W-H, Li M-L, Gao S, Ni J, Zhou L-X, Yao M, Peng B, Feng F, Jin Z-Y, Cui L-Y: **In vivo high-resolution MR imaging of symptomatic and asymptomatic middle cerebral artery atherosclerotic stenosis.** *Atherosclerosis* 2010, **212:**507-511.
96. Ryu CW, Jahng GH, Kim EJ, Choi WS, Yang DM: **High resolution wall and lumen MRI of the middle cerebral arteries at 3 tesla.** *Cerebrovascular diseases (Basel, Switzerland)* 2009, **27:**433-442.

97. Swartz R, Bhuta S, Farb R, Agid R, Willinsky R, Butany J, Wasserman B, Johnstone D, Silver F, Mikulis D: **Intracranial arterial wall imaging using high-resolution 3-tesla contrast-enhanced MRI.** *Neurology* 2009, **72:**627-634.
98. Qiao Y, Steinman DA, Qin Q, Etesami M, Schär M, Astor BC, Wasserman BA: **Intracranial arterial wall imaging using three-dimensional high isotropic resolution black blood MRI at 3.0 Tesla.** *Journal of Magnetic Resonance Imaging* 2011, **34:**22-30.
99. Touboul P-J, Elbaz A, Koller C, Lucas C, Adraï V, Chédru F, Amarenco P, Investigators G: **Common Carotid Artery Intima-Media Thickness and Brain Infarction The Étude du Profil Génétique de l'Infarctus Cérébral (GÉNIC) Case-Control Study.** *Circulation* 2000, **102:**313-318.
100. Bottomley P, Hardy C, Argersinger R, Allen-Moore G: **A review of 1H nuclear magnetic resonance relaxation in pathology: are T1 and T2 diagnostic?** *Medical physics* 1987, **14:**1-37.
101. Rogers WJ, Prichard JW, Hu Y-L, Olson PR, Benckart DH, Kramer CM, Vido DA, Reichek N: **Characterization of Signal Properties in Atherosclerotic Plaque Components by Intravascular MRI.** *Arteriosclerosis, Thrombosis, and Vascular Biology* 2000, **20:**1824-1830.
102. Dalager-Pedersen S, Falk E, Ringgaard S, Kristensen IB, Pedersen EM: **Effects of temperature and histopathologic preparation on the size and morphology of atherosclerotic carotid arteries as imaged by MRI.** *Journal of Magnetic Resonance Imaging* 1999, **10:**876-885.
103. Coolen BF, Poot DH, Liem MI, Smits LP, Gao S, Kotek G, Klein S, Nederveen AJ: **Three-dimensional quantitative T1 and T2 mapping of the carotid artery: Sequence design and in vivo feasibility.** *Magnetic Resonance in Medicine* 2015.
104. Raynaud J-S, Bridal SL, Toussaint J-F, Fornès P, Lebon V, Berger G, Leroy-Willig A: **Characterization of atherosclerotic plaque components by high resolution quantitative MR and US imaging.** *Journal of Magnetic Resonance Imaging* 1998, **8:**622-629.
105. Mihai G, Giri S, Sharkey-Toppen TP, Raman SV, Rajagopalan S, Simonetti PP: **Quantitative T1, T2 and T2* Mapping of Carotid Artery Normal Wall and Atherosclerotic Plaque.** *International Society of Magnetic Resonance in Medicine* 2011.
106. Cai J-M, Hatsukami TS, Ferguson MS, Small R, Polissar NL, Yuan C: **Classification of human carotid atherosclerotic lesions with in vivo multicontrast magnetic resonance imaging.** *Circulation* 2002, **106:**1368-1373.
107. Saam T, Ferguson MS, Yarnykh VL, Takaya N, Xu D, Polissar NL, Hatsukami TS, Yuan C: **Quantitative Evaluation of Carotid Plaque Composition by In Vivo MRI.** *Arteriosclerosis, Thrombosis, and Vascular Biology* 2005, **25:**234-239.
108. Martin AJ, Plewes DB, Henkelman RM: **MR imaging of blood vessels with an intravascular coil.** *Journal of Magnetic Resonance Imaging* 1992, **2:**421-429.
109. Ocali O, Atalar E: **Intravascular magnetic resonance imaging using a loopless catheter antenna.** *Magnetic resonance in medicine* 1997, **37:**112-118.

110. Sathyanarayana S, Bottomley PA: **MRI endoscopy using intrinsically localized probes.** *Medical Physics* 2009, **36:**908-919.

111. El-Sharkawy AM, Qian D, Bottomley PA: **The performance of interventional loopless MRI antennae at higher magnetic field strengths.** *Med Phys* 2008, **35:**1995-2006.

112. Hastie T, Tibshirani R, Friedman J, Hastie T, Friedman J, Tibshirani R: *The elements of statistical learning.* Springer; 2009.

113. Cortes C, Vapnik V: **Support-vector networks.** *Machine learning* 1995, **20:**273-297.

114. Suykens JAK, Vandewalle J: **Least Squares Support Vector Machine Classifiers.** *Neural Processing Letters* 1999, **9:**293-300.

115. Wang G, El-Sharkawy A-MM, Bottomley PA: **Minimum acquisition methods for simultaneously imaging T1, T2, and proton density with B1 correction and no spin-echoes.** *Journal of Magnetic Resonance* 2014, **242:**243-255.

116. Jara H, Fleming K, Sakai O: **PD, T1, and T2 quantitative MRI spectroscopy of the orbit: An application of the Mix-TSE pulse sequence.** In *12th Scientific Meeting and Exhibition of the International Society for Magnetic Resonance in Medicine, Kyoto, Japan.* 2004

117. Jensen M, Caruthers S, Jara H: **Quantitative magnetic resonance imaging with the mixed turbo spin-echo pulse sequence: A validation study.** *Internet Journal of Radiology* 2001, **2**.

118. Glover GH, Schneider E: **Three-point dixon technique for true water/fat decomposition with B0 inhomogeneity correction.** *Magnetic Resonance in Medicine* 1991, **18:**371-383.

119. Wang G, El-Sharkawy A-MM, Bottomley PA: **Minimum Acquisition Methods for Simultaneously Imaging T1, T2, and Proton Density with B1 Correction and No Spin-echoes.** *J Magn Reson*.

120. Hellings WE, Moll FL, de Kleijn DPV, Pasterkamp G: **10-years experience with the Athero-Express study.** *Cardiovascular Diagnosis and Therapy* 2012, **2:**63-73.

121. Li K-C: **Asymptotic Optimality for Cp, CL, Cross-Validation and Generalized Cross-Validation: Discrete Index Set.** *The Annals of Statistics* 1987, **15:**958-975.

122. Hanley JA, McNeil BJ: **The meaning and use of the area under a receiver operating characteristic (ROC) curve.** *Radiology* 1982, **143:**29-36.

123. Martin AJ, Gotlieb AI, Henkelman RM: **High-resolution MR imaging of human arteries.** *Journal of Magnetic Resonance Imaging* 1995, **5:**93-100.

124. Morrisett J, Vick W, Sharma R, Lawrie G, Reardon M, Ezell E, Schwartz J, Hunter G, Gorenstein D: **Discrimination of components in atherosclerotic plaques from human carotid endarterectomy specimens by magnetic resonance imaging ex vivo.** *Magn Reson Imaging* 2003, **21:**465-474.

125. Sun B, Giddens DP, Long R, Taylor WR, Weiss D, Joseph G, Vega D, Oshinski JN: **Automatic plaque characterization employing quantitative and multicontrast MRI.** *Magnetic Resonance in Medicine* 2008, **59:**174-180.

126. Sathyanarayana S, Schär M, Kraitchman DL, Bottomley PA: **Towards Real-Time Intravascular Endoscopic Magnetic Resonance Imaging.** *JACC: Cardiovascular Imaging* 2010, **3:**1158-1165.
127. Shammas NW: **Epidemiology, classification, and modifiable risk factors of peripheral arterial disease.** *Vascular Health and Risk Management* 2007, **3:**229.
128. Fadini GP, Agostini C, Avogaro A: **Autologous stem cell therapy for peripheral arterial disease: Meta-analysis and systematic review of the literature.** *Atherosclerosis* 2010, **209:**10-17.
129. Tateishi-Yuyama E, Matsubara H, Murohara T, Ikeda U, Shintani S, Masaki H, Amano K, Kishimoto Y, Yoshimoto K, Akashi H, et al: **Therapeutic angiogenesis for patients with limb ischaemia by autologous transplantation of bone-marrow cells: a pilot study and a randomised controlled trial.** *The lancet* 2002, **360:**427-435.
130. Ransohoff JD, Wu JC: **Imaging stem cell therapy for the treatment of peripheral arterial disease.** *Current vascular pharmacology* 2012, **10:**361.
131. Kinnaird T, Stabile E, Burnett M, Shou M, Lee C, Barr S, Fuchs S, Epstein S: **Local delivery of marrow-derived stromal cells augments collateral perfusion through paracrine mechanisms.** *Circulation* 2004, **109:**1543-1549.
132. Kedziorek DA, Hofmann LV, Fu Y, Gilson WD, Cosby KM, Kohl B, Barnett BP, Simons BW, Walczak P, Bulte JW: **X-Ray-Visible Microcapsules Containing Mesenchymal Stem Cells Improve Hind Limb Perfusion in a Rabbit Model of Peripheral Arterial Disease.** *Stem Cells* 2012, **30:**1286-1296.
133. Kedziorek DA, Solaiyappan M, Walczak P, Ehtiati T, Fu Y, Bulte JW, Shea SM, Brost A, Wacker FK, Kraitchman DL: **Using C-Arm X-Ray Imaging to Guide Local Reporter Probe Delivery for Tracking Stem Cell Engraftment.** *Theranostics* 2013, **3:**916.
134. Arifin DR, Kedziorek DA, Fu Y, Chan KW, McMahon MT, Weiss CR, Kraitchman DL, Bulte JW: **Microencapsulated cell tracking.** *NMR in Biomedicine* 2013, **26:**850-859.
135. Bulte JW, Kraitchman DL: **Iron oxide MR contrast agents for molecular and cellular imaging.** *NMR Biomed* 2004, **17:**484-499.
136. Nahrendorf M, Sosnovik DE, French BA, Swirski FK, Bengel F, Sadeghi MM, Lindner JR, Wu JC, Kraitchman DL, Fayad ZA: **Multimodality cardiovascular molecular imaging, Part II.** *Circulation: Cardiovascular Imaging* 2009, **2:**56-70.
137. Fu Y, Azene N, Xu Y, Kraitchman DL: **Tracking stem cells for cardiovascular applications in vivo: focus on imaging techniques.** *Imaging in medicine* 2011, **3:**473-486.
138. Ahrens ET, Bulte JW: **Tracking immune cells in vivo using magnetic resonance imaging.** *Nature Reviews Immunology* 2013, **13:**755-763.
139. Barnett BP, Arepally A, Stuber M, Arifin DR, Kraitchman DL, Bulte JWM: **Synthesis of magnetic resonance-, X-ray- and ultrasound-visible alginate microcapsules for immunoisolation and noninvasive imaging of cellular therapeutics.** *Nat Protocols* 2011, **6:**1142-1151.
140. Liddell RP, Patel TH, Weiss CR, Lee DS, Matsuhashi T, Brown P, Gabrielson KL, Rodriguez ER, Eng J, Kimura H: **Endovascular model of rabbit hindlimb**

ischemia: a platform to evaluate therapeutic angiogenesis. *Journal of vascular and interventional radiology* 2005, **16:**991-998.

141. Patel TH, Kimura H, Weiss CR, Semenza GL, Hofmann LV: **Constitutively active HIF-1α improves perfusion and arterial remodeling in an endovascular model of limb ischemia.** *Cardiovascular research* 2005, **68:**144-154.
142. Otsu N: **A threshold selection method from gray-level histograms.** *Automatica* 1975, **11:**23-27.
143. Maki J, Masuda C, Morikawa S, Morita M, Inubushi T, Matsusue Y, Taguchi H, Tooyama I: **The MR tracking of transplanted ATDC5 cells using fluorinated poly-L-lysine-CF3.** *Biomaterials* 2007, **28:**434-440.
144. Khattak SF, Chin KS, Bhatia SR, Roberts SC: **Enhancing oxygen tension and cellular function in alginate cell encapsulation devices through the use of perfluorocarbons.** *Biotechnology and bioengineering* 2007, **96:**156-166.
145. McGovern KA, Schoeniger JS, Wehrle JP, Ng CE, Glickson JD: **Gel-entrapment of perfluorocarbons: A fluorine-19 NMR spectroscopic method for monitoring oxygen concentration in cell perfusion systems.** *Magnetic Resonance in Medicine* 1993, **29:**196-204.
146. Srinivas M, Morel PA, Ernst LA, Laidlaw DH, Ahrens ET: **Fluorine-19 MRI for visualization and quantification of cell migration in a diabetes model.** *Magnetic resonance in medicine* 2007, **58:**725-734.
147. Fu Y, Kedziorek D, Shea S, Ouwerkerk R, Huang G, Ehtiati T, Krieg R, Bulte JWM, Kraitchman DL: **Novel 19F MRI and CT Trackable Microencapsulated Mesenchymal stem cells for treating peripheral arterial disease** *Journal of the American College of Cardiology* 2010, **55:**A216.E2049-A2216.E2049.
148. Lee H, Nalcioglu O, Buxton R: **Correction for chemical-shift artifacts in 19F imaging of PFOB: Simultaneous multislice imaging.** *Magnetic resonance in medicine* 1991, **21:**21-29.
149. Yildirim M, Keupp J, Nicolay K, Lamerichs R: **Chemical shift independent imaging of 19F contrast agents using ultrafast MRSI (F-uTSI).**
150. Hounsfield GN: **Computed medical imaging.** *Medical Physics* 1980, **7:**283-290.
151. Ciarelli MJ, Goldstein SA, Kuhn JL, Cody DD, Brown MB: **Evaluation of orthogonal mechanical properties and density of human trabecular bone from the major metaphyseal regions with materials testing and computed tomography.** *Journal of orthopaedic research : official publication of the Orthopaedic Research Society* 1991, **9:**674-682.
152. González Ballester MÁ, Zisserman AP, Brady M: **Estimation of the partial volume effect in MRI.** *Medical Image Analysis* 2002, **6:**389-405.
153. González Ballester MÁ, Zisserman A, Brady M: **Segmentation and measurement of brain structures in MRI including confidence bounds.** *Medical Image Analysis* 2000, **4:**189-200.
154. Bottomley PA, Wang G, Abdel-monem M: **Systems and methods for measuring nuclear magnetic resonance spin-lattice relaxation time t1 and spin-spin relaxation time t2.** In *Book Systems and methods for measuring nuclear*

magnetic resonance spin-lattice relaxation time t1 and spin-spin relaxation time t2 (Editor ed.^eds.). City: Google Patents; 2012.

155. Zhang Y, Gabr RE, Schär M, Weiss RG, Bottomley PA: **Magnetic resonance Spectroscopy with Linear Algebraic Modeling (SLAM) for higher speed and sensitivity.** *Journal of Magnetic Resonance* 2012, **218:**66-76.

156. Zhang Y, Gabr RE, Zhou J, Weiss RG, Bottomley PA: **Highly-accelerated quantitative 2D and 3D localized spectroscopy with linear algebraic modeling (SLAM) and sensitivity encoding.** *Journal of Magnetic Resonance* 2013, **237:**125-138.

157. Cuppen J: **RLSQ: T1, T2, and ρ calculations, combining ratios and least squares.** *Magnetic resonance in medicine* 1987, **5:**513-524.

Curriculum Vita

Guan Wang

Personal Information

- Date of Birth: June-02-1987; Xi'an, China
- Email: wangg62@gmail.com

Education

- PhD: Johns Hopkins University Baltimore, MD 2009-2015
  Electrical and Computer Engineering
  Advisor: Paul A. Bottomley
- M.Sc.: Johns Hopkins University Baltimore, MD 2009-2012
  Electrical and Computer Engineering
- B.Sc.: Xi'an Jiaotong University Xi'an, China 2005-2009

  Biomedical Engineering

Teaching

- Class assistant: Johns Hopkins University Baltimore, MD Sep-Dec 2013

  Basics of Wave & Quantum Mechanics

Publications

Patent

1. P.A. Bottomley, G. Wang, A.M. EI-Sharkawy. Systems and methods for measuring nuclear magnetic resonance spin-lattice relaxation time t1 and spin-spin relaxation time t2, *US 20130141096 A1*

Peer-reviewed Journal Articles

1. **G. Wang**, A.M. El-Sharkawy, P.A. Bottomley. Minimum acquisition methods for simultaneously imaging T_1, T_2, and proton density with B_1 *correction and no spin-echoes. Journal of Magnetic Resonance 242 (2014) 243–255.*
2. **G. Wang,** A.M. El-Sharkawy, W.A. Edelstein, M. Schär, P.A. Bottomley. Measuring T_2 and T_1, and imaging T_2 without spin echoes. *Journal of Magnetic Resonance 214 (2012) 273-280.*
3. **G. Wang**, X. Wu, S. Wang, X. Guo. Comparison of DNA sequences in gene regulation regions according to the existence of transcription factor binding sites. *Beijing Biomedical Engineering, 2009, 28(002): 170-174.*
4. L.C. Rose, D.K. Kadayakkara, **G. Wang**, A. Bar-shir, B.M. Helfer, C.F. O'Hanlon, D.L. Kraitchman, R.L. Rodriguez, J.W.M Bulte. Fluorine-19 Labeling

of Stromal Vascular Fraction Cells for Clinical Imaging Applications. *Stem Cells Translational Medicine(2015):sctm.2015-0113.*

Conference Abstracts

1. **G. Wang**, M.A. Erturk, S.S. Hegde, P.A. Bottomley. Automated classification of vessel disease based on high-resolution intravascular multi-parametric mapping MRI. *International Society for Magnetic Resonance in Medicine Annual Meeting 2015.*
2. **G. Wang,** A.M. El-Sharkawy, P.A. Bottomley. Imaging T_1, T_2 and proton density with minimum possible acquisitions. *International Society for Magnetic Resonance in Medicine Annual Meeting 2014.*
3. **G. Wang**, M.A. Erturk, S.S. Hegde, P.A. Bottomley. High-resolution multi-parametric characterization of atherosclerotic lesions with 3T intravascular MRI. *International Society for Magnetic Resonance in Medicine Annual Meeting 2014.*
4. **G. Wang**, Y. Fu, S. Shea, J. Cook, D. Kraitchman. Quantitative 19F MRI and CT tracking of the microencapsulated stem cells in a rabbit peripheral arterial disease model. Journal of Cardiovascular Magnetic Resonance, 16(Suppl 1, 2014): P61.
5. **G. Wang**, Y. Fu, S.M. Shea, D.L. Kraitchman. Quantitative ^{19}F MRI and CT tracking of the microencapsulated stem cells in peripheral arterial disease model. *International Society for Magnetic Resonance in Medicine Annual Meeting 2013, Salt Lake City, Utah.*
6. **G. Wang**, Y. Fu, S.M. Shea, J.A. Cook, D.L. Kraitchman. CT and ^{19}F MR imaging for quantitative tracking of encapsulated mesenchymal stem cells in a peripheral arterial disease model. *World Molecular Imaging Congress 2012, Dublin, Ireland.*
7. **G. Wang**, A.M. El-Sharkawy, W.A. Edelstein, M. Schär, and P.A. Bottomley. Measuring T_1 and T_2 and proton density in 3 acquisitions: the Tri-τ method. *International Society for Magnetic Resonance in Medicine Annual Meeting 2012, Melbourne, Australia.*
8. **G. Wang**, A.M. El-Sharkawy, W.A. Edelstein, M. Schar, and P.A. Bottomley. Measuring T2 and T2-imaging without echoes? *International Society for Magnetic Resonance in Medicine Annual Meeting 2011, Montreal, Canada.*